Development of Nanostructured Metal Oxide-Carbon Composites for Rechargeable Li-Ion Battery

Thesis Submitted to the AcSIR for the Award of The Degree of

DOCTOR OF PHILOSOPHY
In
CHEMICAL SCIENCES

By

Pravin Kumari Dwivedi

Registration Number: 10CC14J26008

Under the guidance of

Dr. Manjusha V. Shelke
(Research Guide)

And

Dr. G V N Rathna
(Research Co-guide)

CSIR-NATIONAL CHEMICAL LABORATORY
PUNE – 411008, INDIA

2019


Dedicated to Ma & Papa

सीएसआईआर - राष्ट्रीय रासायनिक प्रयोगशाला
(वैज्ञानिक तथा औद्योगिक अनुसंधान परिषद)
डॉ. होमी भाभा मार्ग, पुणे - 411 008, भारत
CSIR - NATIONAL CHEMICAL LABORATORY
(Council of Scientific & Industrial Research)
Dr. Homi Bhabha Road, Pune - 411 008, India

Certificate

This is to certify that the work incorporated in Ph.D. thesis entitled **"Development of Nanostructured Metal Oxide-Carbon Composites for Rechargeable Li-Ion Battery"** submitted by **Ms. Pravin Kumari Dwivedi** to the Academy of Scientific & Innovative Research (AcSIR), in fulfilment of the requirement for the award of the Degree of **Doctor of Philosophy** embodies original research work under my guidance. We further certify that that this work has not been submitted to any other University or Institution in part or full for the award of any degree or diploma. Research material obtained from other sources has been duly acknowledged in the thesis. Any text, illustration, table etc., used in the thesis from other sources have been duly cited and acknowledged.

It is also certified that this work done by the student under my supervision, is plagiarism free.

Pravin Kumari Dwivedi	**Dr. Manjusha V. Shelke**	**Dr. G V N Rathna**
Student	**(Research Guide)**	**(Research Co-guide)**

Date- 31st July, 2019

Place- Pune

Communication Channels
NCL Level DID : 2590
NCL Board No. : +91-20-25902000
EPABX : +91-20-25893300
: +91-20-25893400
FAX
Director's Office : +91-20-25902601
COA's Office : +91-20-25902660
SPO's Office : +91-20-25902664
WEBSITE
www.ncl-india.org

Declaration

I hereby declare that the thesis entitled **"Development of Nanostructured Metal Oxide-Carbon Composites for Rechargeable Li-Ion Battery"** submitted for the degree of **Doctor of Philosophy** in **Chemical Sciences** to the Academy of Scientific & Innovative Research (AcSIR), has been carried out by me at the Physical and Materials Chemistry Division of CSIR-National Chemical Laboratory, Pune, India, under the guidance of **Dr. Manjusha V Shelke** and co-guidance of **Dr. G V N Rathna**. Such material which has been obtained by other sources has been duly acknowledged in this thesis. The work is original and has not been submitted in part or full by me for any other degree or diploma to other University.

Pravin Kumari Dwivedi
(Research Student)

Date: 26 July, 2019
Physical & Materials Chemistry Division
CSIR-National Chemical Laboratory,
Pune - 411008, India

Acknowledgements

In the journey of my ultimate step of studentship, many people with or without knowing, have contributed significantly to help me reach this level through their constant support and encouragement. Thus, without acknowledging their effort, this thesis may not be complete.

First and foremost, I would like to express my deep and earnest gratitude to my research supervisor ***Dr. (Mrs.) Manjusha V. Shelke****. A mere word of sincere appreciation is insufficient to express my gratitude to her. I am really grateful to her for her guidance, fruitful discussions, valuable advice, constant support and encouragement throughout the course of this work. She generously offered me with freedom in pursuit of various research interests and abundant research resources and collaboration opportunities, which plays a key role in the learning and progress in my career as a research student. Her enthusiasm for research has invigorated me to investigate and complete lots of interesting topics.*

I would also like to thank to my research co-supervisor Dr. G V N Rathna for her supportive nature regarding work and documentation. I also thank her for many fruitful discussions we had. I am also grateful to her to use some of the important instruments in her lab.

I would like to convey my sincere thanks to the DAC members Dr. Mahesh S. Dharne, Dr. J. Nithyanandhan and Dr. Asha S. K. for all their help, support and suggestions during the PhD coursework evaluations and presentations. I would also like to express my gratitude to Prof. Ashwini Kumar Nangia, Director of CSIR-NCL, Dr. Sourav Pal & Dr. K Vijamohanan (former Directors, CSIR-NCL), Dr. Anil Kumar (former Head of the Physical & Materials chemistry Division), Dr. P. A Joy (Head of the Physical & Materials chemistry Division) for providing the infrastructure and advanced facilities for research and giving me an opportunity to work at CSIR-NCL. Also, I would like to thank Dr. Mahesh Kulkarni, Dr. B L V Prasad, Dr. C.G. Suresh, Dr. Chetan Gadgil, Dr. M. S. Shashidhar, Mr. Naveen Pavithran, Mr. P V Iyer, Mrs. Kolhe, Ms. Komal, Ms. Vaishali and SAO staff throughout the journey. I am also grateful to CMC division for providing excellent instrumental facilities and especially Mr. Gholap, Ketan, Harsha, Sheetal, Pooja, Venkatesh, Pankaj, Harshad, Shiv Prakash, Shravya, Sahithi, Tushar, Chetan, Medha, Vijeyta (For SEM and TEM), Dr. C.S. Gopinath, Mr. Deo (For XPS) for their help and support.

I am also thankful to Dr. Satishchandra Ogale, Dr. K Krishnamurthy, Dr.Kadhiravan Shanmuganathan, Dr. P A Joy to allow me to use the instrumental facility in their lab. I would like to thank the staffs from Glass Blowing, Engineering Section, DIRC, Stores and Purchase for providing excellent facility. The entire library staffs for providing excellent facilities are gratefully acknowledged.

I can never forget the help, love and constant encouragement from my lab seniors, Dr. Joy, Dr. Rami, Dr. Sandeep, Dr. Chaitanya, Prof. Indrapal, Dr. Ashvini, Dr. Rupali, Dr. Wahid, Dr. Yogesh and Dr. Satish at crucial junctures. An individual thanks to all my labmates Vedi, Thripuranthaka, Golu, Vikash, Apurva, Poonam, Ojas, Govind, Dr.Swati, Dr. Bhaskar, Dr. Pushpendra, Sravan, Kundan, Thanuja, Sandra saji, Andreas Z B, Dr. Mukta, Astha, Sanket, Mayank, Maitreyee, Aman, Mona, Ankur, Rishi, Poonam, Vandana, Parikshith, Anshuman, Shubham, Pooja, Neha, Amrutha, Amrutha, Nishant and Jeena for creating the wonderful and friendly atmosphere for research in the lab during my stay. A heartfelt thanks to my dearest friends Apurva, Golu and Thripuranthka for being helpful and caring, without your help it was impossible to complete my thesis.

I would like to acknowledge to my beloved friends, Vineeta, Yachita, Ruchi, Bhawana, Sharabjot, Yogita, Garima, Ragini, Monika, Monika, Subhra, Nalinee, Rajan, Roby, Arun, Rahul, Virat, Bhanu, Pratiksh, Amarnath, Rashid, Abhishek, Yashpal, Sandeep, Manoj, Sharad, Rohit, Kailash, Preeti, Tanaya, Munmun, Jhumur for their priceless love, sharing, admirable support and encouragement in happy as well as unhappy situations. I would like to give special thanks to Dr. Devesh, and Dr. Sudheer for their support and motivation in research and personal life to push me and motivate me.

I would also like to express my sincere thanks to all my institute colleagues and friends Pandiraj, Dr. Umesh, Dr. Anil, Dr .Dhanya, Dr. Santhosh, Dr. Aniruddha, Dr. Abhik, Dr. Mukta, Dr. Pradeep, Sheetal, Swati, Ishita, Srashti, Narugopal, Siddhu, Rajith, Aayesha, Vidyanand, Meena, Sachin, Dr. Divya, Dr. Harshita, Kumar, Sudhakar, Gunvant, Geetanjali, Anup, Bharath, Veer, Praveen, Prashant and Ram for their help and support during the course of Ph.D.

Finally, I would like to thank my family for being immensely supportive, loving and caring. I would like to pay my ultimate thanks to my father and mother for building me to what I am. It was because of their encouragement and motivation that I could think of pursuing higher education. I would like to thank my brothers (Nitin, Vipin, Krishnakant and Shrikant,)

and my sister Jyoti for being a strong support. I would never be able to pay back the love and affection showered upon me by my parents and family. I would like to give my deepest gratitude to my brother late Mr. Jitendra Dwivedi (Sonu Bhaiya) for his valuable support and care.

Finally thanks to the almighty for giving me the strength and patience to work through all these years.

Pravin Kumari Dwivedi

List of Abbreviations

Abbreviations	Expansions
1D	One-dimensional
2D	Two-dimensional
3D	Three-dimensional
AC	Activated Carbon
BET	Brunauer-Emmett-Teller
CCD	Charge coupled device
CCO 1:1	f-CNH-Co_3O_4 1:1
CCO 1:2	f-CNH-Co_3O_4 1:2
CCO 2:1	f-CNH-Co_3O_4 2:1
CE	Coulombic efficiency
CMC	carboxymethyl cellulose
CNF	Carbon nano fibre
CNH	Carbon nanohorn
CNO	Carbon nanoonions
CNT	Carbon nanotube
CV	Cyclic voltammetry
CVD	Chemical vapor deposition
DEC	Diethylene carbonate
DMC	Dimethyl carbonate
DSC	Differential Scanning Calorimetry
DEC	Dimethylene carbonate
EC	Ethylene carbonate
EDLC	Electrical double layer capacitor
EDS	Energy-dispersive X-ray spectroscopy
EDX	Energy dispersive X-ray
EIS	Electrochemical impedance spectroscopy
ESR	Equivalent series resistance
FCC	Face centered cubic
F-CNH	Functionalized carbon nanohorn
FEC	Fluoroethylene carbonate

FESEM	Field emission scanning electron microscopy
GCD	Galvanostatic charge-discharge
HCl	Hydrochloric acid
HEVs	Hybrid electric vehicles
HF	Hydrofluoric acid
HOMO	Highest occupied molecular orbital
IRL	Irreversible capacity loss
KOH	Potassium hydroxide
LCO	$LiCoO_2$
LFP	$LiFePO_4$
LIBs	Li-ion batteries
LiTFSI	(Li-bistrifluoromethane sulfonamide)
LMA	$LiMnO_2$
LNCA	$LiNi_{0.8}Co_{0.15}Al_{0.05}O_2$
LNO	$LiNiO_2$
LTO	$Li_4Ti_5O_{12}$
LUMO	lowest unoccupied molecular orbital
LVP	$Li_3V_2(PO_4)_3$
MCMB	MesoCarbon MicroBeads
MWCNT	Multi walled carbon nanotube
NDC	Nitrogen doped carbon
NFO	$Ni(OH)_2/Fe_2O_4$
NFOC	$Ni(OH)_2/Fe_2O_3$/CNO
NFOC-10	$Ni(OH)_2/Fe_2O_3$/CNO-10
NFOC-20	$Ni(OH)_2/Fe_2O_3$/CNO-20
NFOC-30	$Ni(OH)_2/Fe_2O_3$/CNO-30
NLDFT	Nonlocal density functional theory
NMP	N-methyl pyrrolidinone
NPs	Nanoparticles
PAMAC	Poly (acrylamide-*co*-diallyldimethylammonium chloride)
PC	Porous carbon
PC	Propylene carbonate

PEO	Polyethylene oxide
PSD	Pore size distribution
PTPAn	Polytriphenylamine
PVDF	Polyvinylidene fluoride
RGO	Reduced graphene oxide
SAED	Selected area diffraction pattern
SBR	styrene-butadiene rubber
SEI	Solid electrolyte interface
SEM	Scanning electron microscopy
SSA	Specific surface area
SWCNT	Single walled carbon nanotube
TEM	Transmission electron microscopy
TGA	Thermogravimetric analysis
VC	vinylene carbonate
XPS	X-ray photoelectron spectroscopy
XRD	X-ray diffraction

Table of Content

Abstract

3d transition metal oxides have been considered as a promising anode materials for rechargeable lithium-ion batteries (LIBs) as it possess high theoretical capacity, low toxicity, and cost effectiveness. Nanostructure engineering provides an opportunity to play with different morphology and structures of nanomaterials which helps to enhance the electrochemical performance of electrode materials. Carbon plays an effective role in hybrid nanomaterials electrode for LIB, as it improves the electrochemical performance by enhancing the conductivity, buffering the volume expansion and contraction of the electrode material during continuous charge discharge process. Doping of heteroatoms such as Nitrogen, Boron, Sulphur etc. on the surface of carbon matrix can improve electrochemical performance with enhanced lithiation capacity. Lone pair electrons of N and S atoms contribute to extension of the conjugated electron clouds of carbon matrix resulting in increased conductivity which enhances the rate capacity and cycle life of the electrode material.

The main objective of the research is to develop metal oxide and carbon based anode materials for LIBs with high specific capacity, excellent rate performance and long cycle life. In case of transition metal oxide and carbon nanocomposite, carbon matrix act as barrier to inhibit agglomeration of metal oxide nanoparticles, stabilize the solid electrolyte interphase (SEI) film, and restrain the volume change of metal oxide during cycling process along with improved electronic conductivity of the composite. Finally, nanocomposite of transition metal oxide and carbon provides high specific capacity with long cycle life which serves as an excellent anode material for LIB.

Chapter 1: This chapter highlights the importance of energy storage devices and LIBs. This chapter also encompasses of working principle and different components of LIBs. It also includes the several challenges of LIBs in practical applications.

Chapter 2: This chapter includes the synthesis techniques of different nanocomposites of metal oxides and carbon materials. Then it describes the different instrumental techniques for material characterisation like powder X-ray diffraction, scanning electron microscope, transmission electron microscopy, X-ray photoelectron spectroscopy, thermal gravimetric analysis, and electrochemical characterisation of material with cyclic voltammetry, galvanostatic charge-discharge and impedance measurement.

Chapter 3: This chapter demonstrates the synthesis of ternary hybrid composite of $Ni(OH)_2$-Fe_2O_3/Carbon Nano Onions (NFOC) by using two-step solution phase method which delivers a high reversible discharge capacity of 928 $mAhg^{-1}$ at 50 mAg^{-1} and 673 $mAhg^{-1}$ at a higher

current density of 1000 mAg^{-1} with excellent rate performance. Additionally, it shows stable cycle life up to 1000 cycles with 96% capacity retention and more than 99% of coulombic efficiency. The reversible reaction of Fe_2O_3 and $Ni(OH)_2$ with Li, maintains its long cycle life with higher reversible discharge capacity and CNOs improve the efficient electronic transfer, accommodate substantial volume expansion and maintain the structural integrity of the material during lithiation-delithiation process.

Chapter 4: This chapter involves the synthesis of nanocomposite of polydopamine (PDA) derived N doped carbon with Nickel ferrite / Nickel Oxide as an electrode material via solvothermal reaction followed by annealing at 550^0C. Here, PDA, being a nitrogen-rich biomimetic polymer, has been used to synthesize N doped carbon which can buffer the volume expansion of high-capacity lithium-storage materials and improve the conductivity of electrode material during continuous lithiation delithiation. NDC/$NiFe_2O_4$/NiO shows high specific capacity of 786 $mAhg^{-1}$ at 0.1 Ag^{-1} of current density. At 2 Ag^{-1} of current density it exhibits 463 $mAhg^{-1}$ of Specific capacity. Additionally, it shows very stable cyclic performance up to 1000 cycle at 1 Ag^{-1} of current density and deliver specific capacity of 510 $mAhg^{-1}$.

Chapter 5: This chapter describes the synthesis of nanocomposite of Co_3O_4 nanoparticles with 3D network of CNH foam via freeze drying process. The composite were formed by decorating Co_3O_4 NPs on to CNH foam with high surface area. These interconnected network helps in good conductivity of Li-ions and electrons during charge-discharge and provide stability. CCO 1:1 shows high reversible capacity of 797 $mAhg^{-1}$ at 0.1 Ag^{-1} of current density and at very high current density of 5 Ag^{-1} it exhibit 702 $mAhg^{-1}$ of specific capacity. Also, it gives stable performance over 500 cycles with 78% capacity retention as well as >99 % coulombic efficiency.

Chapter 6: N and S co-doped carbon spheres with Co_3O_4 nanocomposite (NSCS-Co_3O_4) is developed in this work via solvothermal reaction of saccharose with L-cysteine. Hetero atoms doping in carbon matrix alter the electronic properties, which increase the reactivity of carbon surface and become effective for anchoring metal oxide nanoparticles. N and S doped carbon spheres provide efficient electron/ion transfer channels, hinder the agglomeration of Co_3O_4 nanoparticles and serve as a buffer to sustain volume expansion during charge-discharge and enhance the electrochemical performance of electrodes. Stable cycling behaviour is observed at 1 Ag^{-1} with 1285 $mAhg^{-1}$ of specific capacity retained after 350 cycles along with more than 99% of coulombic efficiency.

Chapter 7: This chapter highlights the overall conclusion of above chapters. Future prospects include the use of above prepared electrode material as an anode for Na-ion battery.

Chapter 1

Introduction

This chapter includes an introduction to energy storage devices and Li ion battery. A brief discussion about the importance of the Li ion battery with improvement over the other secondary batteries like lead acid, Ni-Cd, and Ni-MH battery is given. The basic information of different cell components like anode, cathode, separator and electrolyte is depicted. It includes different types of materials used as an anode and cathode. The battery terminologies like power density, C-rate, etc. with the aging and internal resistance of battery responsible for battery degradation are described. Last section of the chapter describes the challenges for Li ion battery in practical applications.

1.1 Energy resources

Energy resources available in the world are classified mainly into two categories: Renewable and Non-Renewable Energy sources. Non-renewable as the name suggests are those energy resources which are in limited quantity and are not replenished. Fossils Fuels, coal, petroleum and natural gases are some examples of non-renewable resources which are viable to be extinct. [1, 2] Renewable energy resources unlike non-renewable resources are abundant in nature and are naturally available. Some of the examples of renewable energy are solar energy, tidal energy, wind energy, geothermal energy, etc. [3, 4]

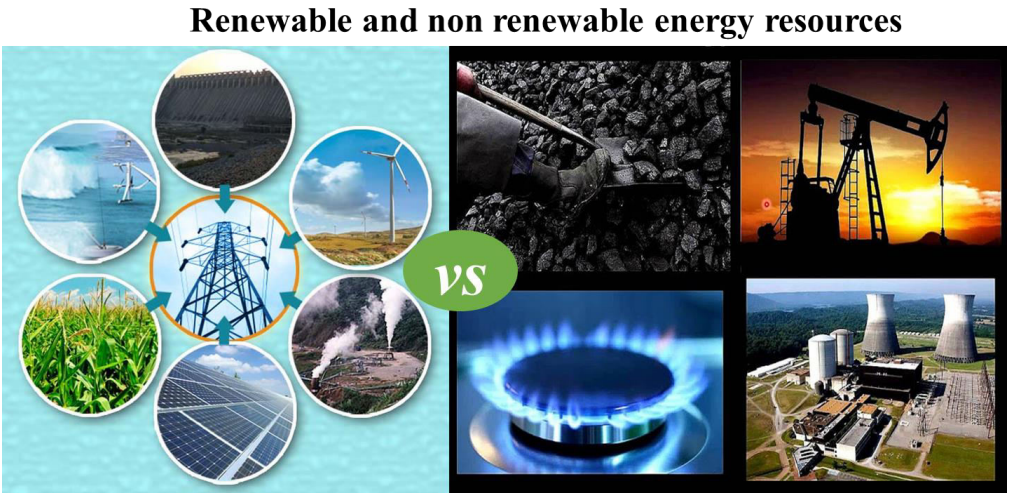

Figure 1.1: Types of energy resources. *(https://byjus.com/physics/renewable-energy/ and https://benz.lastri.co/what-makes-a-non-renewable-energy-resource/)*

1.2 Need for energy storage

Population explosion and rapid industrialisation in the previous century has affected the balance and harmony between nature and mankind severely. Mankind has been dependent on non-renewable resources for its energy requirement in the modern world to an extent of their endangered depletion, which affects sustainability. [5] This led to the way of sustainable development in which energy requirements are fulfilled without harming ecosystem and using only natural resources. Implementing sustainable development faces some hindrances like the uneven distribution of renewable resources across the world. For instance, solar energy in some areas is too extreme while in others it is limited or with low insolation and thus it cannot be used in this region. Similarly other renewable energy resources like wind energy, tidal energy and geothermal energy show characteristic fluctuations and hence their utilisation faces some hurdles. Thus the current situation demands for conservation of energy and its storage and a lot of attention is being given in this field as the fossil fuels are depleting at an alarming rate. This led to the idea of clean and green energy which remains environment friendly and do not cause any pollution for energy conversion and storage.

1.3 Energy storage systems

The energy storage devices provide us the ease of usage of energy at anytime and anywhere. These devices are used for storing and supply of energy in a desired form at the time of requirement. There are generally mechanical storage systems, chemical storage systems and electrical storage systems. Mechanical storage systems can be classified into Hydroelectricity, Pumped storage, Flywheel energy storage and Gravitational potential energy. The thermal energy storage systems are based on temperature difference and basically capture heat and cold substances. Physical characteristics of the materials such as latent heat define the basis of working of thermal energy storage systems and thus it includes the phase change materials and the thermo-chemical energy storage in its class. In chemical storage systems, working is much like a fuel cell where hydrogen is stored. In electrical energy storage systems there are two categories. In the first one capacitors are used to store energy electrostatically and in the other one superconducting magnets are used in which a direct flow of current induces magnetic field in a superconducting coil. [6] In the electrochemical energy storage systems energy is stored in the form of chemical energy. The above mentioned energy storage technologies have been analysed over the time and it was found that in energy usage sectors, electrochemical and chemical energy storage have great significance. Most of the energy is used in residential purposes as well as transportation. For this a convenient, portable and easy handling energy storage system provides much utility. In this regard electrical and electrochemical energy storage systems become utterly important to be flourished.

1.4 Electrochemical energy storage devices

The electrochemical energy storage devices have primary components as follows:

Cathode: Reduction takes place during discharge reaction (Positive Electrode)

Anode: Oxidation takes place during charge reaction (Negative Electrode)

Separator: Thin film material used to avoid direct contact between cathode and anode to prevent short circuiting of cells and allows ions to flow through it.

Electrolyte: An aqueous, alkaline or organic medium which facilitates ion flow from one direction to another.

Capacitors, supercapacitors, batteries and fuel cells are primarily used as major electrochemical energy storage and conversion devices.

1.4.1 Comparison of different devices

From application point of view Supercapacitors are used for applications requiring large amount of energy in a short interval as they have high power density. [7] Similarly

Batteries and Fuel cells are used in applications demanding continuous supply of electrical energy as they have high energy density. [8, 9] To deliver power and energy simultaneously, these devices could be used in combinations. Performance of these devices is mainly analysed and evaluated in terms of energy density and power density. This can be analysed from the Ragone plot as it shows power vs. energy densities of various clean energy storage devices as shown in figure 1.2. [10] Ragone plot shows that capacitors possess very high power density but low energy density and fuel cells have high energy density but low power density. Unlike these, supercapacitors and batteries are moderate in their performance. Supercapacitors have high power density but lower energy density as compared to batteries. Batteries have high energy density which gives reasonably good cycle life and this has developed interest among the researchers. This makes batteries to be used in mobile applications, various gadgets to grid storage. The development of battery is being done from a long time undergoing changes in their chemistry, design and materials.

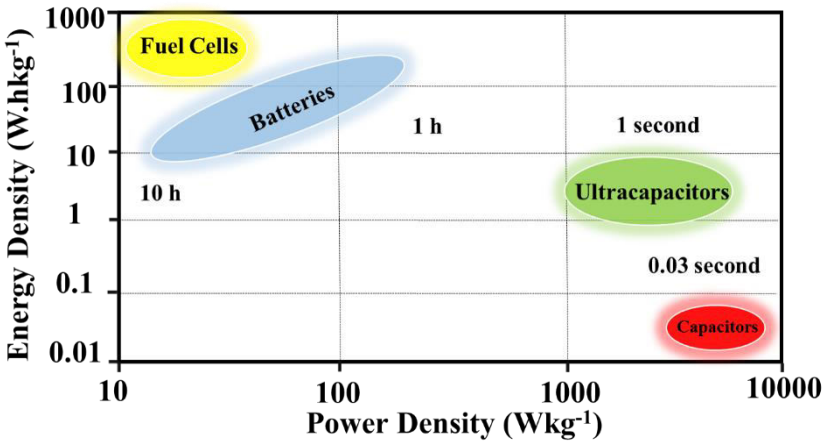

Figure 1.2: Ragone plot for various energy storage and conversion devices.

1.5 Li-ion battery

An electrochemical cell is made up of two electrochemically active positive and negative electrodes (anodes and cathodes) in an electrolyte solution. Both the electrodes are separated by separator which is ionically conducting and electronically insulating. Stack of this type of electrochemical cells forms a Battery. During charging and discharging, electrons are transferred from one electrode to another electrode via outer circuit whereas internally ions get transferred through the electrolyte to complete the flow of current with the help of redox reaction. Once redox reaction gets completed flow of current is restricted and battery stops working. Such batteries are termed as primary batteries. [11] Whereas rechargeable batteries allow recharging by application of current where electrons flow in opposite direction. [12] These are termed as secondary batteries. The electrode capability for any battery

is determined by various factors such as electrochemical capacity, energy density, power density which depends on the number of electrons exchanged during the redox reaction, formula weight and battery voltage which is determined by the difference between the involved redox couples' potential. Lead acid, Ni-Cd, Ni-MH batteries are the type of secondary batteries. Lead acid battery is the oldest rechargeable battery which is economically priced, but it has a low specific energy and limited cycle life. [13, 14] Also toxic nature of lead hinders its practical application. Ni-Cd battery shows high discharge rate, ultrafast charging capacity and sustainability up to -20°C temperature. But high self-discharge and more cost prevents its practical application. Ni-MH is the replacement of Ni-Cd battery, which is having high energy density, low self-discharge rate, low internal resistance and less toxic compare to Ni-Cd battery.[15] Among all these batteries, Li ion battery shows high energy density, no memory effect, relatively low self-discharge rate (less than half of Ni-Cd and NiMH), and low Maintenance compare to other secondary battery. [16] Figure 1.3 shows a Ragone plot of various secondary battery technologies in terms of volumetric and gravimetric energy density which highlights that Lithium ion battery has excellent volume energy density as well as specific energy density. [12] This is the reason that portable electronic devices and electric vehicles have used rechargeable LIBs extensively to fulfil their power requirement.

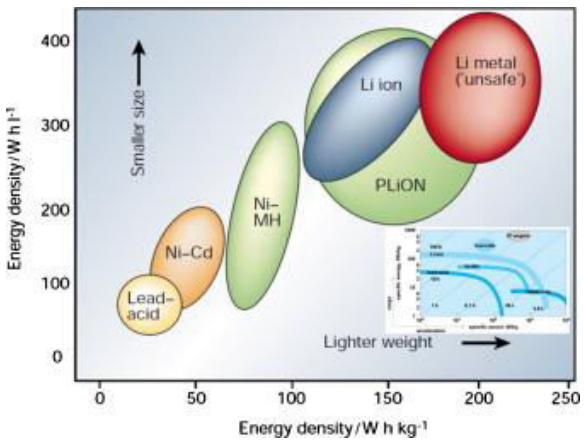

Figure 1.3: Ragone plot comparing the various battery technologies in terms of volumetric and gravimetric energy density *(Reprinted with the permission of Electrochim. Acta, 2012, 84, 235–249).*

The contribution of American scientist John B. Goodenough in the development of Li ion battery is very significant. In 1980, he proposed a Li containing oxide $LiCoO_2$ (LCO) as cathode material, which actually started Li ion battery era. In the same year graphite anode with solid electrolyte was discovered by Rachid Yazami of Morocco. In 1985, the first prototype of Li ion battery was successfully achieved by Japan. [17] In 1991 the commercialisation of battery was done by Sony. Li ion batteries are now commercially used

for both large scale and small scale applications. Li polymer batteries were initially developed by liquid electrolytes. But these electrolytes which were generally based on carbonates were flammable and posed a threat to the safety of the device. To mitigate this problem, Li polymer batteries were then developed using electrolyte based on polymer or gel. But this led to drastic demands which exploited global lithium resources. So, availability, safety and cost of lithium reserves have to be answered for large-scale applications. This led to the exploration of low cost, abundant resources and safe rechargeable batteries with a long cycle-life.

1.5.1 Working principle of Li-ion battery

In conventional LIBs, graphite is used as an anode electrode material and layered $LiCoO_2$ is used as a cathode electrode acting as intercalate host for Li^+, and both of them are separated by a porous separator (permeable membrane), which allows Li^+ ions to pass through it and hinder the short circuit by avoiding direct contact of the electrodes. During charging process, Li^+ ions de-intercalate from cathode electrode and intercalate into the layered graphite via passing through the Li ion conductive electrolyte. Figure 1.4 shows the schematic diagram which explains the mechanism of LIB. The lithium ion and electron generation occurs through the following reactions:

Cathode: $LiCoO_2 \rightarrow Li_xCoO_2 + xLi^+ + xe^-$

Anode: $6C + xLi^+ + xe^- \rightarrow Li_xC_6$

To pair with the excess positive charge (Li^+) generated in the electrode, the electron travels via the external electric circuit and reverse mechanism takes place in the discharging process.

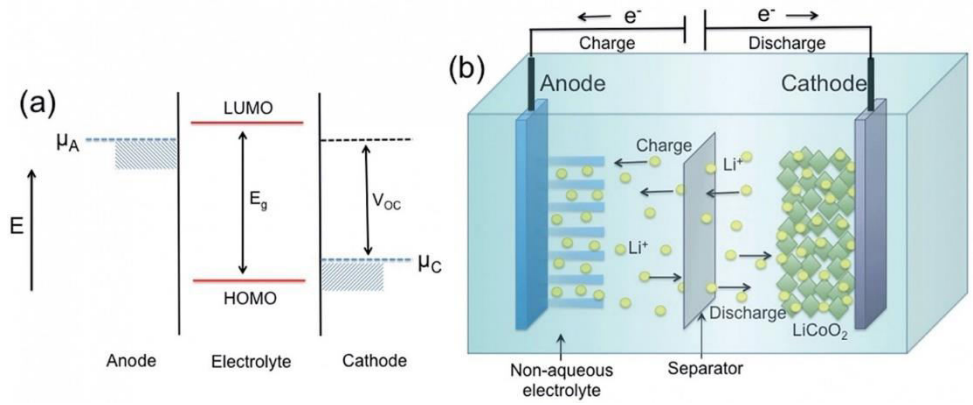

Figure 1.4: (a) Relative energy diagram of electrode potentials and electrolyte energy gap in LIBs; (b) schematic diagram of the lithium intercalation–de-intercalation reaction mechanism in a rechargeable lithium-ion battery containing solid electrodes and a liquid electrolyte *(Reprinted with the permission of J. Mater. Chem. A, 2015, 3, 2454-2484).*

The electrode active material depends upon their electrochemical potential values as well as their relative position with the HOMO-LUMO energy gap of the electrolyte. In an ideal cell, the electrochemical potential of anode should be lower in energy than the LUMO of the electrolyte to avoid the reduction of electrolyte and on the other side electrochemical potential of cathode should be higher in energy than the HOMO of the electrolyte to prevent the oxidation of electrolyte as shown in figure 1.4. [11] In order to achieve high energy density, it is necessary to have maximum electrochemical potential difference between cathode and anode along with high capacity value. While maintaining these parameters, the stability of electrolyte ought not to be neglected. [18]

1.5.2 Cathodes

The cathodes (positive electrodes) are usually Li-ions containing 3d transition metal oxides involving compounds like layered, spinel, olivine and tavorite depending on the crystal structure and atomic arrangement. The various cathodes used in Li ion battery are:

1.5.2.1 Transition metal oxides

Introduction of $LiCoO_2$ (LCO), (proposed by Goodenough and commercialized by Sony) has marked the beginning of layered transition metal oxides as cathode materials. [19, 20] These layered transition metal oxides have a hexagonal geometry in which the Li ions and the transition metal ions in the octahedral voids occupy alternate layers. Even though LCO is an excellent cathode material with several advantages such as high stability, high theoretical capacity (274 $mAhg^{-1}$), low self-discharge rate and high operating voltage (up to 4.2 V), the high cost of Co and the limitations in the supply of the same has been hindering the extensive utilization of LCO in commercial Li ion batteries.[21] In addition to it, LCO also faces challenges such as thermal instability and rapid fading of capacity at higher C-rates. [22, 23]

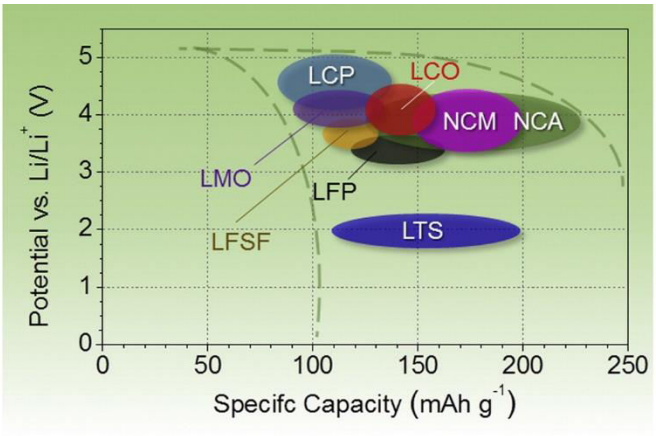

Figure 1.5: Various cathodes and their operating potentials (*Reprinted with the permission of Mater. Today, 2015, 18, 252–264*).

$LiNiO_2$ (LNO) is another promising layered transition metal oxide which possesses similar structure and theoretical capacity to that of LCO. Besides, the low cost of Ni makes LNO a better material in the economical aspect compared to LCO. The main drawback of these materials is that during the synthesis and delithiation process, Li ions were substituted by Ni ions and thereby it blocks the Li diffusion pathways. Also these materials possess a higher thermal instability since Ni^{3+} easily gets reduced.

Thermal instability has been a major concern in these materials and it has been found out that the partial substitution of Co by Ni as well as doping with metals such as Al, Mg are effective in counteracting thermal instability defects. One such material is $LiNi_{0.8}Co_{0.15}Al_{0.05}O_2$ (NCA), which has longer stability and higher discharge capacity (200 $mAhg^{-1}$) compared to conventional cathodes. [24] However the presence of solid electrolyte interfaces and the formation of cracks at the grain boundaries hinders its performance at higher temperatures. $LiMnO_2$ (LMO) is another material explored as cathode in LIBs.[25, 26] Even though Mn is cheap and less toxic than Co and Ni, LMO has less cycling performance since it changes its structure from layered to spinel during the process of Li extraction and Mn dissolution into the electrolyte at higher voltage. [27, 28] Therefore the need of a stable and cheaper cathode material has been very crucial.

1.5.2.2 Polyanionic compounds

Polyanionic compounds are another class of promising cathode materials. As the name implies, these compounds contain a large size of $(XO_4)^{3-}$ ion; where, X= (P, S, Si, Mo). These polyanions are located at the lattice positions. The ability to increase the cathode working potential and thereby increasing the power density of the material makes these compounds a great choice for cathode materials. $LiFePO_4$ (LFP) is a popular polyanionic compound with high power capability and thermal stability. [29] It has an olivine structure where octahedral sites are occupied by Li and Fe ions and tetrahedral voids are filled by P atoms. Oxygen atoms forms an array of distorted hexagonal closed packing symmetry. Even though it serves as a good cathode material, the low working potential and limitations in both ionic and electrical conductivity are the major disadvantages. Using various nanostructures and composites helps to resolve these problems to a greater extent.

There are other olivine class compounds such as $LiMnPO_4$, $LiCoPO_4$. $LiNi_{0.5}Co_{0.5}PO_4$, $LiMn_{0.33}Fe_{0.33}Co_{0.33}PO_4$ etc that has shown an improvement in capacity values but has limited conductivity (figure 1.6).[30, 31] $Li_3V_2(PO_4)_3$ (LVP) is the most promising material among these class since it has high operating voltage (4 V) and high specific

capacity (197 $mAhg^{-1}$). Also the carbon composite of LVP has performed well at higher C rates and their values are in accordance with the theoretical capacity.

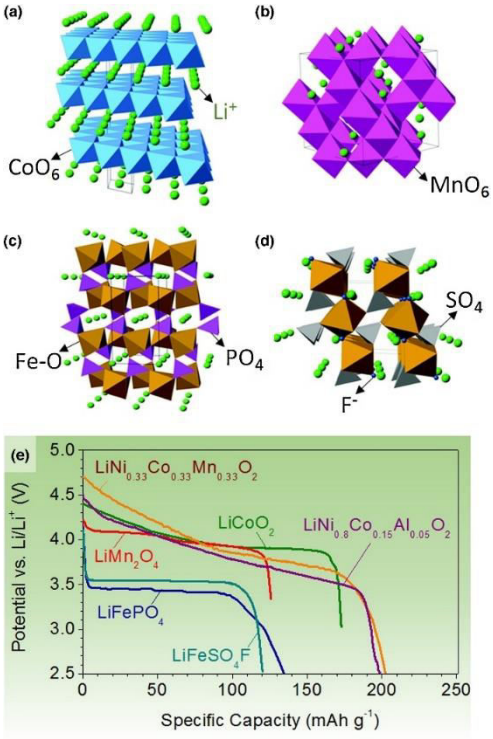

Figure 1.6: Crystal structures of (a) layered ($LiCoO_2$), (b) spinel ($LiMn_2O_4$), (c) olivine ($LiFePO_4$), and (d) tavorite ($LiFeSO_4F$) and (e) their discharge profiles (*Reprinted with the permission of Mater. Today, 2015, 18, 252–264*).

1.5.3 Anodes

Among all alkali metals, Li metal is lightweight with very high specific capacity (3800 $mAhg^{-1}$). Thus, Li is used as an anode material and has very high energy density. But dendrite formation during lithiation delithiation at high C-rate can tear the separator and leads to the shortening of the cell. Also, safety is another major concern with LIBs, as when it comes in contact with moisture, it can easily catch fire. Hence, development of new anode material other than Li metal is mandatory. Currently, conventional anode materials for LIBs are mainly based on carbonaceous materials such as graphite, which have been used in portable electronics for decades. Though, graphite is used as an anode in commercial portable electronic devices, it is still lagging behind to meet the requirements for large scale applications like EVs and HEVs as it has lower specific capacity.[32] To develop high efficient anode materials with high specific capacity, long cycle life, easy diffusivity of Li ions and with less safety issue is more desirable to substitute graphite anodes. The diverse electrode materials have been burst forth, their reaction mechanism with Li ions can be illustrated as intercalation-De intercalation, alloying-dealloying, and Conversion reaction mechanisms, as shown in figure 1.7.

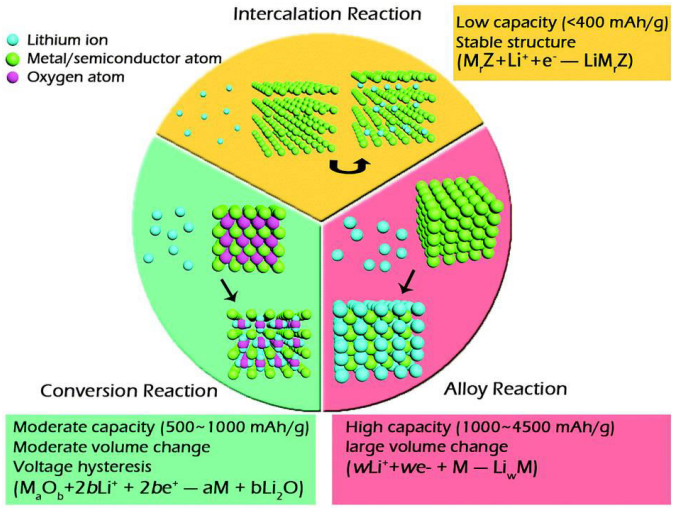

Figure 1.7: Different Reaction mechanism in LIBs (*Reprinted with the permission of J. Power Sources, 257 2014, 421–443*).

1.5.3.1 Intercalation-deintercalation

Carbon allotropes like graphene, CNFs, CNHs and CNTs, TiO_2 based materials, and orthorhombic Nb_2O_5 are showing intercalation and deintercalation reaction mechanism in LIBs. These electrode materials are capable enough to provide fast Li ion kinetics and to maintain their structural integrity on lithiation-delithiation process due to robust open framework with low volume expansion and improve the rate performance and cycle stability. Although, insertion materials with their finite accommodation sites have relatively less theoretical specific capacity (one electron per metal ion). Due to higher electronic conductivity, high surface area, short diffusion path length and more Li ion storage capability (2 times higher than graphite) of graphene, graphene oxide and CNTs got more attention towards high rate applications, but their low lithiation potential causes intrinsic safety issues. [33] Also, these insertion materials are promising candidates as conductive additives or an electrode support due to their mechanical robustness, chemical stability and better electronic conductivity.

Titanium oxides and their composites are also suitable candidates as an anode material for LIBs with safe lithiation potential (>1.5 V *versus* Li^+/Li), excellent reversible capacity and less volume change (<5%). However, very low intrinsic electron and ion conductivity limits its application for fast rechargeable LIBs. [34] Presently, $Li_4Ti_5O_{12}$ has been used commercially in ultrafast charging batteries and exhibit longer cycle stability (>1000 cycles). Similarly, T-Nb_2O_5 materials with intercalation pseudo capacitance mechanism are also suitable candidates for high rate performance of LIBs, offering two dimensional

transport pathways and showed little structural changes upon insertion and deinsertion mechanism.[35]

1.5.3.2 Alloying-dealloying

In alloying-dealloying mechanism, metal like Si, Sn, Ge, *etc.* makes an alloy with Li in Li_xM form and deliver the highest volumetric as well as gravimetric energy densities since they can store multiple Li-ions (per M). Thus, these type of materials are efficient for high performance LIB applications. Silicon forms $Li_{4.4}Si$ alloy with Li which exhibits highest theoretical capacity of 4200 $mAhg^{-1}$. Similarly, Ge has a theoretical capacity of 1600 $mAhg^{-1}$ in the form of $Li_{4.4}Ge$, and Sn has a less specific theoretical capacity of 960 $mAhg^{-1}$ in $Li_{4.2}Sn$ form because of its larger atomic mass. However, poor reaction kinetics and large volume expansion during lithiation and delithiation causes material pulverization and amorphization leading to the severe capacity fade, decrease in the rate performance and cycle life of LIBs.[36] Therefore, it is required to develop several nano structural material and different nanocomposites which can accommodate large volume expansion and contraction while maintaining their mechanical strength during cycling process to improve capacity retention and long cycle life.

1.5.3.3 Conversion reaction

Transition metal oxides are the potential candidates as anode material for LIBs for the substitution of graphite electrode due to very high theoretical specific capacity. Additionally, reversible reaction with Li metal reduces the metal-lithium alloy formation as follows:

$$MO + xLi^+ + xe^- \leftrightarrow Li_2O + M\ (M = Fe, Co, Ni, Cu)$$

The above forward reaction is thermodynamically feasible and involves multi electron transfer per metal atom, leads to high theoretical capacity.[37] However, the backward reaction, formation of the Li^+ ion from Li_2O is a thermodynamically unfavourable and facilitated by metal nanoparticles (M) synthesis during the reaction and this reversibility of the above reaction is well maintained in the nanoscale system and improve the capacity retention as well as the thickness of SEI film at high current density. In conversion mechanism, the normal reaction voltage range is within 0.5-1.0 V, which increases with the ionicity of the M-O bond.[32] So the higher reversible specific capacity and safer lithiation potential of these materials are important parameters for high performance LIBs but poor reaction kinetics, large volume expansion and large potential hysteresis, related to the energy barrier in the breaking of the M-O bond and the change of electronic conductivity, diminish the electrochemical performance and long term cycle life of LIBs for large scale applications.[32] In this context, several researchers have developed nanostructured porous materials and their

nanocomposites with improved reaction kinetics to enhance the cycle life and capacity retentions of LIBs.

1.5.4 Conductive additives

Conductive additives are widely used to decrease the electrical resistance of electrochemical system. Most promising conductive additives are carbonaceous materials like super-P, MesoCarbon MicroBeads (MCMB), graphene and graphene oxides, carbon nanotubes, etc. because of their high electrical as well as thermal conductivity. Also these additives remain unreacted in the electrochemical redox reaction of cell.[38] Conductive additives are very corrosion resistive in acidic and basic medium and have very low weight with relatively low production cost. Optimum quantity of conducting carbon (< 10 %) should be used to enhance the energy density and specific capacity of the electrode.

1.5.5 Binders

Binders in electrochemical cells are mandatory component which hold the electrode material, conductive additive and provide sufficient contact to current collector. An ideal binder should be chemically as well as electrochemically inert, conducting in nature, effective dispersive and easily accessible to electrolyte. Thus, the choice of suitable binder for any particular electrode and electrolyte media affects the rate performance as well as life time of the battery. Most commonly used binder is Polyvinylidene fluoride (PVDF) in current battery industry because of its high stability and bonding performance but excessive use of PVDF in electrode material decreases the battery performance by blocking pores and hinder the electrolyte access to active material. Additionally, at higher temperature PVDF forms lithium fluoride with lithiated carbon which may become the reason of self-heating thermal runway. Polyethylene oxide (PEO), Poly (acrylamide-*co*-diallyldimethylammonium chloride) (AMAC), carboxymethyl cellulose (CMC) and styrene-butadiene rubber (SBR) are another potential binders for electrode fabrication in Li-ion battery. [39-41]

1.5.6 Electrolyte

The electrolytes are the third essential component of rechargeable LIB other than anode and cathode. Electrolytes provide an ionic conductive medium to transport lithium-ions back and forth in between cathode and anode during lithiation/delithiation process. LIB electrolyte is a mixture of non-aqueous organic solutions with dissolved Li-salt. Although, capacity of a cell mostly depends upon the structural and electronic nature of its electrodes, but poor cycle life is due to the side reactions of electrolyte with electrode materials, hence selection of electrolyte plays crucial role in battery performance. Ideally, it should possess extensive electrochemical window (4.5 V for high voltage cathodes) to hamper degradation

of electrolyte, high Li^+ ion conductivity and electronically insulating over a wide range of temperature to diminish self-discharge. It should be less toxic, cost effective, non-flammable, nonexplosive, chemically and thermally stable. [42] Electrolyte should not undergo chemical and mass change during charge and discharge process for long cycle life and safety.

In LIB, most commonly used electrolyte is lithium salts ($LiPF_6$) (1.0 M) dissolved in ethylene carbonate (EC) and ethyl methyl carbonate (EMC) (EC: EMC; 1:1, v/v) or diethyl carbonate (DEC) (EC: DEC; 1:1, v/v). But in case of $LiPF_6$, there is possibility of HF formation which may corrode the Al current collector and cause safety issue. Another alternative electrolyte salt is $LiClO_4$, which is corrosion resistant and has good ionic conductivity but it is explosive in nature and formed passivation layer is unstable. Li-bistrifluoromethane sulphonamide (LiTFSI) has gained interest lately but has low ionic conductivity and relatively high cost.[43]

As carbonates solvents have flammability issue at higher temperature, thus several other solvents like glyme based and ionic liquid electrolytes are also being used to increase thermal stability.[44, 45] Additives like fluoroethylene carbonate (FEC) and vinylene carbonate (VC) are also employed to improve the electrochemical performance of battery. FEC is used to increase LiF content in the SEI layer which provide stability to SEI layer and gives long term cycle life.

1.5.7 Separators

Separator is one of the most essential component of the rechargeable batteries. Separator is a very thin insulating polymeric porous membrane which separates both the anode and the cathode electrodes to prevent short circuit and facilitates ionic transport. It should be mechanically and thermally stable, chemically inert to electrolyte and electrode materials, electronically insulated and ion conducting. Whatmann (cellulose membrane) is the most commonly used separator which provide good ionic conduction for Li ions. Other than Whatmann, polyolefin based separators with semi-crystalline structure like polyethylene, polypropylene and their blends (polyethylene-polypropylene) separators are also used.[46] These polymeric single layer and multilayer separators have high thermal and mechanical stability, excellent porosity and durability. Now a days, grafted polymers with micro-porous nature like poly(methyl methacrylate)-grafted and siloxane grafted polyethylene separators show better electrochemical performance to conventional polyethylene separators. Polytriphenylamine (PTPAn)-modified separator is another polymeric separator, which is electroactive and shows reversible overcharge protection.

1.6 Terminologies used in battery field

1.6.1 Theoretical capacity

The theoretical capacity of any electrode material gives the valuation of the specific capacity attained by that electrode. Theoretical capacity can be calculated by following equation:

$$C = \frac{nF}{(M_w \times 3.6)}$$

Where n is the no. of Li ions participate during charge-discharge, F is the Faraday's constant (96500 C mol^{-1}) and Mw is molecular weight of the material in $gmol^{-1}$. The unit of theoretical capacity is $mAhg^{-1}$.

1.6.2 Energy density and Power Density

Amount of charge stored during charging and discharging by any material is called energy density. [48] The energy density of any battery is calculated by following equation:

$$E = It \times V$$

Where E is the energy density, I is current, t is time of charging and discharging, V is voltage. The unit of gravimetric energy density is $Whkg^{-1}$.

Capability of any electrode material to store or deliver charge during charge-discharge process is called power density and it can be calculated by following formula:

$$P = E \times t$$

Unit of power density is Wkg^{-1}.

1.6.3 Solid electrolyte interphase (SEI)

In battery, during lithiation and delithiation electrolyte decomposition takes place on electrode surface and forms an electronically insulating and ionically conducting polymeric layer which is called as solid electrolyte interphase (SEI) layer.[47] SEI layer formation plays a very crucial role in electrochemical performance of battery. SEI layer prevents further reduction of electrolyte on electrode surface and affords ion conducting interface. As substantial amount of Li ions get utilized in SEI layer formation in initial cycle, which leads to the irreversible capacity loss (IRL). For better battery performance thickness of SEI layer should be optimum. Otherwise too thick SEI causes increase in the charge transfer resistance by preventing the permeation of ions and too thin SEI gets shattered during lithiation-delithiation and exposes electrode for further electrolyte reduction which potentially cause more capacity loss. [48, 49]

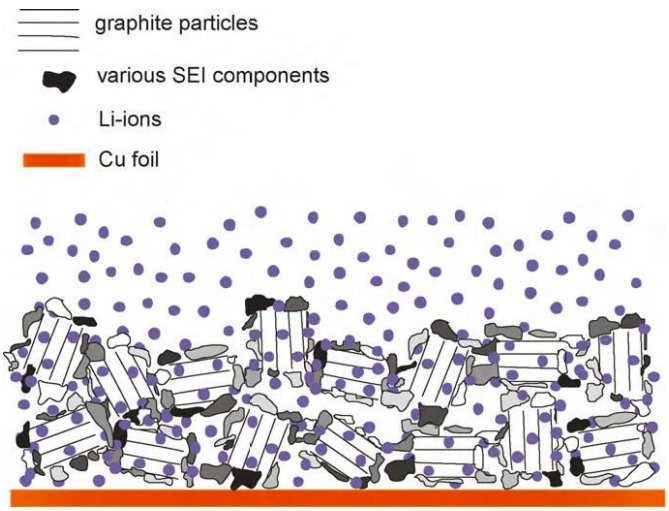

Figure 1.8: Illustration of SEI layer components (*Reprinted with the permission of Electrochim. Acta. 55, 2010, 6332–6341*).

1.6.4 C-rate

A rate at which the battery is charged or discharged relative to its maximum capacity is called as C -rate. 1C rate means a current which charge or discharge the complete battery in 1 hour. The C-rate can be calculated by the theoretical capacity and the active mass loading of electrode material.

1.6.5 Stability

Stable performance of any battery is decisive factor in determining the durability of the LIB. If any battery is showing stable capacity performance for several hundreds of cycles and not losing the initial capacity then that would be the ideal situation. But practically, battery capacity fades during continuous cycling and the capacity retention is calculated for a number of cycles. There are several reasons which increase the capacity fading like poor shelf life (storage of battery for the long time without any use cause capacity decay for the initial cycles), electrolyte degradation, side reaction of electrode and electrolyte etc.

1.6.6 Coulombic efficiency

Coulombic efficiency (CE) is also called current efficiency or faradaic efficiency. CE is the ratio of the total charge delivered during discharge process to the total charge stored during charging process in a full cycle. The Coulombic efficiency (C.E.) is calculated as follows:

$$\text{C.E.} = \frac{Discharge\ Capcity}{Charge\ Capacity} * 100$$

If coulombic efficiency is 100 % then the number of ions extracted and stored are same during discharge and charge process. If it is less than 100 % that means ions are irreversibly lost in discharge process, which is due to the ions can be trapped in nanopores of

the electrode material and can't be release after applying the same potential. Additionally, dissolution of the active material in electrolyte during cycling can be the reason of less coulombic efficiency.

1.7 Factors affecting battery performance

There are several factors which affect the performance of battery at certain points. Primary battery stops working when chemicals present inside the cells are completely exhausted or no longer in their original state to undergo the desired chemical reaction. Secondary battery shows reasonably longer cycle life however in these batteries also some undesirable processes occur which decrease the cycle life. The factors causing these unwelcoming outcomes are:

1.7.1 Aging

Aging is an undeniable procedure which occurs in battery due to some irreversible physical and chemical changes and deteriorates the material and decrease the battery performance during cycling. There are several degradation processes occur such as electrolyte decomposition, the formation of surface films on both electrodes, compromised inter-particle contact at the cathode, etc. causing aging in a cell. The total capacity of any battery can be divided into three states- the empty zone which can be refilled, the available energy region and the rock content which is inactive or dead and increases as battery ages and cannot be rejuvenated.

Figure 1.9: Battery energy utilization zones (*Reprinted with the permission of https://batteryuniversity.com/learn/article/capacity_loss*).

1.7.2 Internal resistance

In less conducting materials, internal resistance is unavoidable process in a battery. On increasing internal resistance, the internal temperature of the cell increases during charge discharge operation and rise the voltage drop which leads to an early shutdown of the device.

So complete energy cannot be employed in such case and the battery needs to be charged sooner than usual.

1.7.3 Self-discharge

In batteries, Self-discharge is a process in which internal chemical reactions reduce the stored charge even in unused condition. Self-discharge decreases the life time of batteries. It also decreases the initial capacity of battery than a full charge state when actually put to use. The rate of self-discharge varies from different battery chemistries and increases with the time. The self-discharge is enhanced at elevated temperature conditions and increased reaction rates.

1.8 Battery challenges

Potentially LIBs are capable of fulfilling energy demands of society and serve its needs. The advent of LIBs has become essential part in our household appliances. But we are not completely independent of fossil fuels till now and as such non-renewable sources of energy are still playing a major role in fulfilling today's energy requirements. This happened because of some key challenges faced by LIBs which are hindering in its complete evolution. These are listed below.[50]

1.8.1. Increase in energy density

The biggest challenge for LIBs and other emerging batteries is the competition by already existing battery types and by gasoline in terms of performance and price. Like gasoline, apart from being cheap it provides 3000 WhL^{-1} energy density as compared to LIB which has energy density of 250 $WhKg^{-1}$ which is 10-15 folds lesser. It is also true for Lead acid battery technology as they span total 60% of automobile applications whereas Li ion batteries are not even close. [51, 52] The performance of current systems and energy density can be increased if cathode materials possess high redox potentials or have capability to take ions in reverse manner (for higher specific capacity). [53, 54]

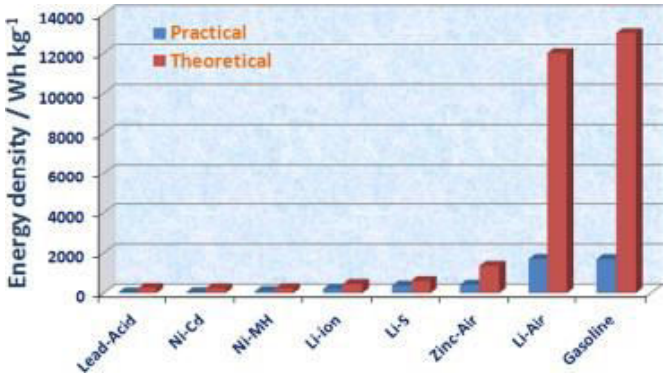

Figure 1.10: Bar graph representation of practical and theoretical energy density of various batteries (*Reprinted with the permission of Nano Energy, 2013, 2, 443–467).*

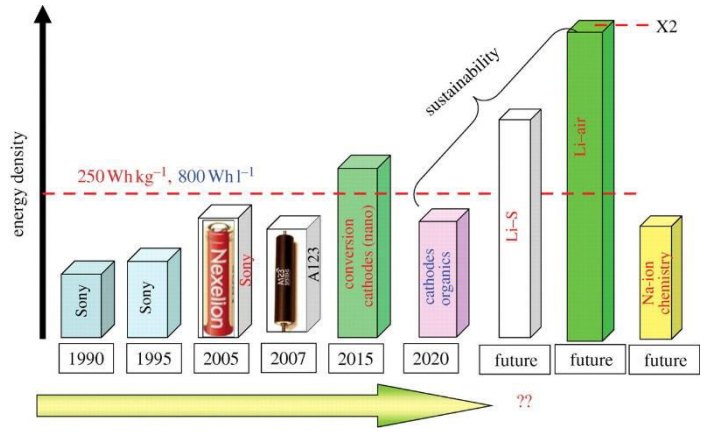

Figure 1.11: Energy density evaluation of various battery chemistries (*Reprinted with the permission of Philos. Trans. R. Soc. A Math. Phys. Eng. Sci., 2010, 368, 3227–3241*).

1.8.2 Safety

In portable electronics and to some extent electric vehicles (EVs), Li ion batteries are in great demand and hence are commercially successful. But they pose risk to safety as happens with the additives which are used to modify electrode electrolyte interface.[55] Though these additives are used for stability and capacity enhancement, beyond certain temperatures and certain chemical environments, these are not safe to use. Such as in case of LIB fabricated using less reducing material LTO as an anode and high oxidising positive electrode like LCO.

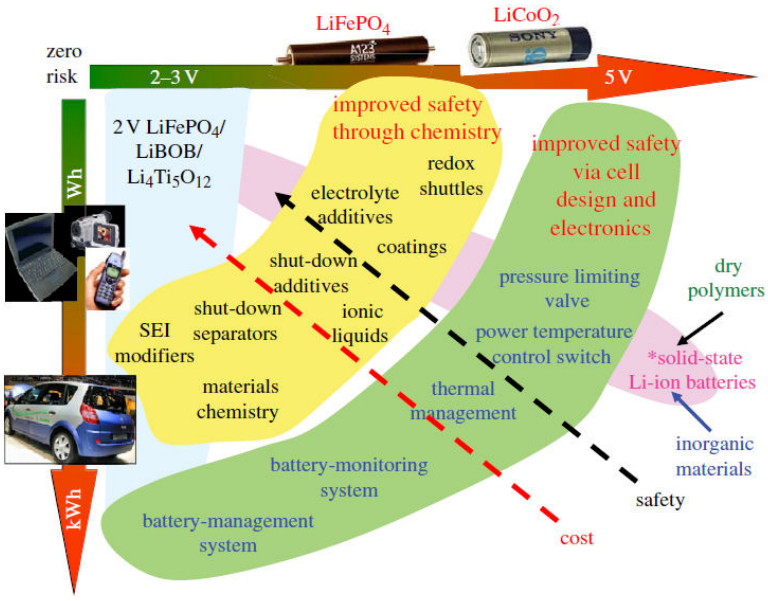

Figure 1.12: Safety aspects of Li ion battery (*Reprinted with the permission of Philos. Trans. R. Soc. A Math. Phys. Eng. Sci., 2010, 368, 3227–3241*).

Moreover instead of liquid electrolytes, solid electrolytes including polymer and inorganic electrolytes may be used to attain safety as well as performance in terms of high energy

density. Figure 1.12 shows the interconnection between all parameters responsible for battery performance.[56] Operating voltage and compatibility of electrolyte has to be taken care of during designing the material as their optimized combination can lead to a prolonged and good battery performance. The quality component should never be compromised at the cost of safety, though it may come at the cost of power density or energy density and at high cost.

1.8.3 Cost

In practical world, cost and safety go hand in hand, where compromise in cost can create safety issues. So we need to shift to materials whose production should not affect the battery industry processes largely and their cost is also within range. [57] Most of the Li reserves are found to be concentrated in Brine (found in Chile). So the given data is based on elemental composition of brine. As the concentration of Li is highly uneven the cost of Li has increased tremendously. The estimated consumption of extracted Li (46%) is done by battery industry.[58] The same is happening to other metals used in this industry as well like Co and Ni which form the core of battery chemistry due to their usage as positive electrodes. Therefore high power and high energy densities should be the criteria of designing new cathodes. They in turn should also be safe and cost effective.

1.8.4 Clean and green Li-ion battery

Li-ion battery chemistry is generally considered as green. But due to added energy consumption caused by electrode production and the battery recycling is unable to satisfy the criteria of green chemistry. Working of LIBs produces CO_2 emissions during charging and discharging which causes harm. [59] The synthesis of LIBs is costly and the processes are also not environment friendly. These factors have to be considered seriously and possibly rectified to get sustainable and green batteries. Hence efforts have to be dedicated to upgrade synthesis procedures and better recycling techniques to make them greener.[60, 61]

1.9 Plan and structure of the thesis

This thesis includes the synthesis of composites of transition metal oxides and different type of carbons (carbon nano onions, 3 D f-CNH foam, and hetero atoms doped carbon) and used as anode materials for LIBs application. Transition metal oxides store charge via conversion reaction with Li ions and deliver high specific capacity. Utilization of carbon material in the composites increases the conductivity of electrodes, provides more surface area, and acts as a buffer to maintain structural integrity of electrode materials and enhances the electrochemical performance.

Chapter 1 explains about energy storage devices, Li ion battery and its working phenomenon. Later it discusses the different type of cell components of Li ion battery, terminologies used in battery and its challenges in practical application.

Chapter 2 gives the detailed explanation of different synthesis procedures of nanomaterials. It also discusses the different material characterization and electrochemical characterization techniques.

Chapter 3 projects the synthesis of ternary nanocomposite of $Ni(OH)_2$-Fe_2O_3/CNOs via two step solution phase method and solvothermal procedure. As synthesized material was used as an anode material for high performance Li ion battery. This ternary hybrid nanocomposite delivers a high reversible discharge capacity of 928 $mAhg^{-1}$ at 50 $mAg^{-1}$and 673 $mAhg^{-1}$ at a higher current density of 1 Ag^{-1} with excellent rate performance.

The chapter 4 presents a synthesis of ternary nanocomposite of Polydopamine Derived N-doped Carbon with NiO/$NiFe_2O_4$ via same method used in previous chapter followed by annealing at 500 ºC temperature in inert atmosphere and utilised as an anode material for Li ion battery. It exhibit a reversible discharge capacity of 786 $mAhg^{-1}$ at 0.1 Ag^{-1} and 463 $mAhg^{-1}$ at a higher current density of 2 Ag^{-1} with excellent rate performance.

The chapter 5 emphasizes the synthesis of well-designed Co_3O_4 nanoparticles anchored on functionalized carbon nano horn foam nanocomposite via freeze drying process and demonstrated as anode material for Li-ion battery with improved electrochemical properties. As synthesized electrode material displays a reversible capacity of 797 $mAhg^{-1}$ at 0.1 Ag^{-1} of current density and excellent rate performance with 702 $mAhg^{-1}$ at 5 Ag^{-1} of high current density.

The chapter 6 includes the synthesis of nanocomposite of N and S co-doped Carbon spheres (NSCS) with Co_3O_4. N and S doped carbon spheres are prepared by hydrothermal reaction of saccharose with L-cysteine and followed by its carbonization in inert atmosphere. Co_3O_4 and heteroatom doped carbon spheres composite synthesized via solvothermal method and further used as an anode material for Li ion battery. It shows stable cycling behavior at 1 Ag^{-1} with 1285 $mAhg^{-1}$ of specific capacity retained after 350 cycles along with more than 99% of coulombic efficiency. This material shows an excellent rate capability with specific capacity retained to 745 $mAhg^{-1}$ even at high current density of 5 Ag^{-1}.

1.10 References

[1] C. Tugcu, I. Ozturk and A. Aslan, *Renewable and non-renewable energy consumption and economic growth relationship revisited: Evidence from G7 countries*, 2012, vol. 34.

[2] R. Perez and M. Perez, *Int. Energy Agency SHC Program. Sol. Updat*, 2015, **62**, 4-6.

[3] A. K. Tiwari, *Econ. Bull.*, 2011, **31**, 2356-2372.

[4] K. Ellegård and J. Palm, *Appl. Energy*, 2011, **88**, 1920-1926.

[5] B. R. Keeble, *Med. War*, 1988, **4**, 17-25.

[6] M. Gu, I. Belharouak, J. Zheng, H. Wu, J. Xiao, A. Genc, K. Amine, S. Thevuthasan, D. R. Baer, J.-G. Zhang, N. D. Browning, J. Liu and C. Wang, *ACS Nano*, 2013, **7**, 760-767.

[7] L. Guan, L. Yu and G. Z. Chen, *Electrochim. Acta*, 2016, **206**, 464-478.

[8] D. P. Dubal, O. Ayyad, V. Ruiz and P. Gomez-Romero, *Chem. Soc. Rev.*, 2015, **44**, 1777-1790.

[9] E. P. Murray, T. Tsai and S. A. Barnett, *Nature*, 1999, **400**, 649-651.

[10] C. Wang, E. Zhou, W. He, X. Deng, J. Huang, M. Ding, X. Wei, X. Liu and X. Xu, *Nanomater.* , 2017, 7.

[11] J. B. Goodenough and K.-S. Park, *J. Am. Chem. Soc.*, 2013, **135**, 1167-1176.

[12] B. G. Pollet, I. Staffell and J. L. Shang, *Electrochim. Acta*, 2012, **84**, 235-249.

[13] R. S. Treptow, *J. Chem. Educ.*, 2002, **79**, 334.

[14] P. Ruetschi, *J. Power Sources*, 1977, **2**, 3-120.

[15] F. Putois, *J. Power Sources*, 1995, **57**, 67-70.

[16] A. M. Zelinsky, M. J. Koch and K.-H. Young, *Batter.* , 2018, 4.

[17] C. Pillot, The Rechargeable Battery Market and Main Trends 2015-2025, Adv. Automot. Batter. Conf. (2016).

[18] G.-N. Zhu, H.-J. Liu, J.-H. Zhuang, C.-X. Wang, Y.-G. Wang and Y.-Y. Xia, *Energy Environ. Sci.*, 2011, **4**, 4016-4022.

[19] N. Recham, M. Armand, L. Laffont and J.-M. Tarascon, *Electrochem. Solid-State Lett.*, 2009, **12**, A39-A44.

[20] K. Ozawa, *Solid State Ionics*, 1994, **69**, 212-221.

[21] S. Choi and A. Manthiram, *J. Electrochem. Soc.*, 2002, **149**, A162-A166.

[22] J. Cho, Y. J. Kim, T.-J. Kim and B. Park, *Angew. Chemie Int. Ed.*, 2001, **40**, 3367-3369.

[23] I. D. Scott, Y. S. Jung, A. S. Cavanagh, Y. Yan, A. C. Dillon, S. M. George and S.-H. Lee, *Nano Lett.*, 2011, **11**, 414-418.

[24] N. Nitta, F. Wu, J. T. Lee and G. Yushin, *Mater. Today*, 2015, **18**, 252-264.

[25] F. Amalraj, D. Kovacheva, M. Talianker, L. Zeiri, J. Grinblat, N. Leifer, G. Goobes, B. Markovsky and D. Aurbach, *J. Electrochem. Soc.*, 2010, **157**, S19-S19.

[26] T. J. Welgemoed and C. F. Schutte, *Desalination*, 2005, **183**, 327-340.

[27] M. Gu, I. Belharouak, J. Zheng, H. Wu, J. Xiao, A. Genc, K. Amine, S. Thevuthasan, D. R. Baer, J.-G. Zhang, N. D. Browning, J. Liu and C. Wang, *ACS Nano*, 2013, **7**, 760-767.

[28] M. M. Thackeray, S.-H. Kang, C. S. Johnson, J. T. Vaughey, R. Benedek and S. A. Hackney, *J. Mater. Chem.*, 2007, **17**, 3112-3125.

[29] Y. Nishi, ed. G. B. T.-L.-I. B. Pistoia, Elsevier, Amsterdam, 2014, pp. 21-39.

[30] D. Choi, D. Wang, I.-T. Bae, J. Xiao, Z. Nie, W. Wang, V. V Viswanathan, Y. J. Lee, J.-G. Zhang, G. L. Graff, Z. Yang and J. Liu, *Nano Lett.*, 2010, **10**, 2799-2805.

[31] J. M. Lloris, C. Pérez Vicente and J. L. Tirado, *Electrochem. Solid-State Lett.* , 2002, **5**, A234-A237.

[32] Y. Tang, Y. Zhang, W. Li, B. Ma and X. Chen, *Chem. Soc. Rev.*, 2015, **44**, 5926-5940.

[33] C. M. Hayner, X. Zhao and H. H. Kung, *Annu. Rev. Chem. Biomol. Eng.*, 2012, **3**, 445-471.

[34] G.-N. Zhu, H.-J. Liu, J.-H. Zhuang, C.-X. Wang, Y.-G. Wang and Y.-Y. Xia, *Energy Environ. Sci.*, 2011, **4**, 4016-4022.

[35] V. Augustyn, J. Come, M. A. Lowe, J. W. Kim, P.-L. Taberna, S. H. Tolbert, H. D. Abruña, P. Simon and B. Dunn, *Nat. Mater.*, 2013, **12**, 518.

[36] M. M. Thackeray, C. Wolverton and E. D. Isaacs, *Energy Environ. Sci.*, 2012, **5**, 7854-7863.

[37] P. Poizot, S. Laruelle, S. Grugeon, L. Dupont and J.-M. Tarascon, *Nature*, 2000, **407**, 496.

[38] M. E. Spahr, eds. M. Yoshio, R. J. Brodd and A. Kozawa, Springer New York, New York, NY, 2009, pp. 117-154.

[39] L. Chen, X. Xie, J. Xie, K. Wang and J. Yang, *J. Appl. Electrochem.*, 2006, **36**, 1099-1104.

[40] W.-R. Liu, M.-H. Yang, H.-C. Wu, S. M. Chiao and N.-L. Wu, *Electrochem. Solid-State Lett.* , 2005, **8**, A100-A103.

[41] H. Buqa, M. Holzapfel, F. Krumeich, C. Veit and P. Novák, *J. Power Sources*, 2006, **161**, 617-622.

[42] A. Ponrouch, E. Marchante, M. Courty, J.-M. Tarascon and M. R. Palacín, *Energy Environ. Sci.*, 2012, **5**, 8572-8583.

[43] Q. Li, J. Chen, L. Fan, X. Kong and Y. Lu, *Green Energy Environ.*, 2016, **1**, 18-42.

[44] J. M. Tarascon and D. Guyomard, *Solid State Ionics*, 1994, **69**, 293-305.

[45] M. Dahbi, F. Ghamouss, F. Tran-Van, D. Lemordant and M. Anouti, *J. Power Sources*, 2011, **196**, 9743-9750.

[46] https://batteryuniversity.com/learn/article/bu_306_battery_separators.

[47] G. Ramos-Sanchez, F. A. Soto, J. M. Martinez de la Hoz, Z. Liu, P. P. Mukherjee, F. El-Mellouhi, J. M. Seminario and P. B. Balbuena, *J. Electrochem. Energy Convers. Storage*, 2016, **13**, 31002-31010.

[48] G. Fitzgerald, J. DeJoannis and M. Meunier, in *Woodhead Publishing Series in Electronic and Optical Materials*, eds. V. K. Tewary and Y. B. T.-M. Zhang Characterization, and Production of Nanomaterials, Woodhead Publishing, 2015, pp. 3-53.

[49] P. Verma, P. Maire and P. Novák, *Electrochim. Acta*, 2010, **55**, 6332-6341.

[50] P. Poizot and F. Dolhem, *Energy Environ. Sci.*, 2011, **4**, 2003-2019.

[51] J. Wang, Y. Li and X. Sun, *Nano Energy*, 2013, **2**, 443-467.

[52] X. G. Zhang, *J. Power Sources*, 2006, **163**, 591-597.

[53] Q. Pang, D. Kundu, M. Cuisinier and L. F. Nazar, *Nat. Commun.*, 2014, **5**, 4759.

[54] E. Deiss, F. Holzer and O. Haas, *Electrochim. Acta*, 2002, **47**, 3995-4010.

[55] T. J.-M., *Philos. Trans. R. Soc. A Math. Phys. Eng. Sci.*, 2010, **368**, 3227-3241.

[56] H. Chen, M. Armand, G. Demailly, F. Dolhem, P. Poizot and J.-M. Tarascon, *ChemSusChem*, 2008, **1**, 348-355.

[57] B. Dunn, H. Kamath and J.-M. Tarascon, *Science*, 2011, **334**, 928-935.

[58] C. Vaalma, D. Buchholz, M. Weil and S. Passerini, *Nat. Rev. Mater.*, 2018, **3**, 18013.

[59] N. Recham, M. Armand, L. Laffont and J.-M. Tarascon, *Electrochem. Solid-State Lett.* , 2009, **12**, A39-A44.

[60] D. Ilic, M. Kilb, K. Holl, H. W. Praas and E. Pytlik, *J. Power Sources*, 1999, **80**, 112-115.

[61]J.-M. Tarascon, N. Recham, M. Armand, J.-N. Chotard, P. Barpanda, W. Walker and L. Dupont, *Chem. Mater.*, 2010, **22**, 724-739.

Chapter 2

Material Synthesis and Characterization Techniques

In this chapter, the general synthesis protocols of the nanomaterials (metal oxides and carbon) are discussed. The advantages of synthetic protocols are also outlined. The second section of the chapter describes detailed study of various characterization techniques such as X-Ray Diffraction, Thermogravimetric analysis, X-ray Photoelectron Spectroscopy, BET surface area measurements and electron microscopy (SEM and TEM) which are indispensable for nanomaterials characterization. Also a detailed account of electrochemical characterization techniques like cyclic voltammetry, galvanostatic charge-discharge measurements and impedance measurements employed for analysing Li-ion battery performance is presented.

2.1 Material synthesis

Over few decades, lot of fundamental studies are performed on nanomaterials, especially on their synthesis and characterization. The key challenging aspect in ensuring the efficient utilization of nanomaterials for several applications lies in the synthesis of the materials. Synthetic protocols have a major role in controlling the morphology as well as various properties of the nanomaterials and composites. Since these engineered nanomaterials provides a space for extensive applications, it is vital to explore the domain of it by developing more nanomaterials and extend their applications. The most widely used synthetic methods for nanomaterials include sol-gel method, microemulsion technique, hydrothermal synthesis, chemical vapour deposition, high-temperature pyrolysis and laser-based synthesis techniques.

2.1.1 Sol-gel method

The sol-gel method comprises of two components sol and gel, respectively. Sol is a colloidal suspension of solid in a liquid while the gel is the polymer containing liquid. This process involves the network formation of discrete particles or polymers by connecting the sol particles. [1] The sol-gel process comprises of two important steps called hydrolysis and condensation in which the bonds of the precursor are disintegrated using water in the former and the nanomaterials are formed in the latter. The final structure of the material is determined after the removal of excess water. [2, 3]

2.1.2 Microemulsion techniques

Microemulsions are clear, isotropic mixtures of three components such as water (polar phase), surfactant and oil or hydrocarbon liquid (non-polar phase). Microemulsions are characterized by their thermal stability and homogeneity. Each component plays a significant role in maintaining the stability of microemulsions. Surfactants reduce the interfacial tension by creating a layer separating the aqueous and organic solvents and thereby preventing the merging of droplets. [4] Depending upon the nature of the surfactant used, microemulsions constitutes monodispersed droplets like water- in- oil (w/o) or oil- in- water (o/w). These droplets are generally in the range of 600-8000 nm in size. The water-in-oil system which forms the reverse micelle organization where the non-polar ends of the surfactant protruding outside forms the centre for nanoparticle synthesis. The polar head groups of the surfactant are directed towards the interior and as shown in figure 2.1a. It has been reported that there are two different microemulsion strategies for the synthesis of nanoparticles, namely (1) one microemulsion method and (2) two microemulsion method (figures 2.1b and c). The one microemulsion method can be subdivided into two types namely the energy triggering

method and microemulsion plus reactant method. As the name suggests, the energy triggering method requires a triggering agent which would initiate the synthesis within a single emulsion droplet containing the precursor whereas the latter method is started with the addition of a reactant into the microemulsion containing the second reactant. [5]

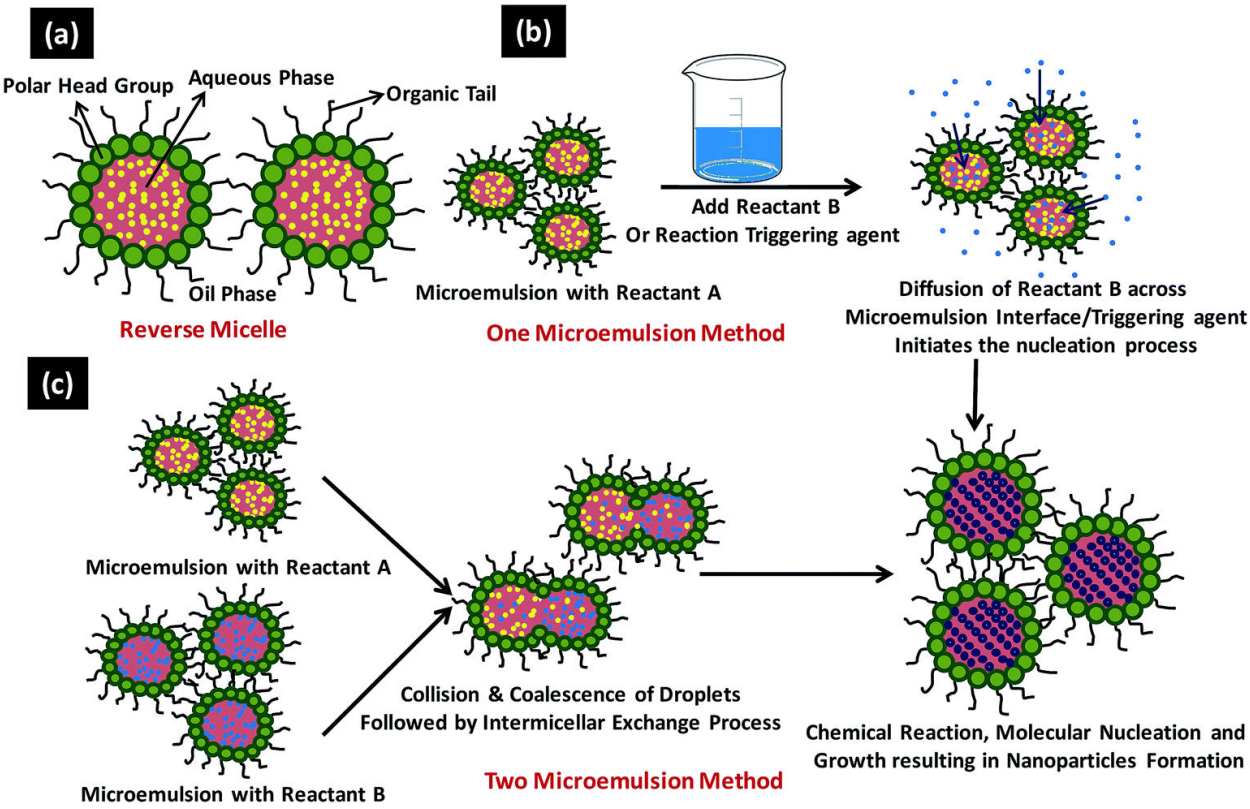

Figure 2.1: Shows (a) typical reverse micelle system, (b) various steps involved in one microemulsion process and (c) reaction sequence involved in the two microemulsion nanoparticles synthesis (*Reprinted with the permission of RSC Adv., 2015, 5, 105003-105037*).

2.1.3 Hydrothermal/Solvothermal process

In hydrothermal synthesis technique, the key factor controlling the synthesis of single crystals is the solubility of minerals in water under high temperature and pressure. The synthesis and growth are carried out in an apparatus called autoclave, which is a steel pressure vessel that has nutrient supply along with water. In order to dissolve the nutrients, a temperature gradient is maintained at the opposite ends of the growth chamber. The seeds will have additional growth in the cooler end. [6, 7]

The advantages of the hydrothermal method include the ability to synthesize crystals of substances which are unstable near the melting point, and the ability to synthesize large crystals of high quality. This process is referred as a solvothermal synthesis for the solvent other than water. [8-10]

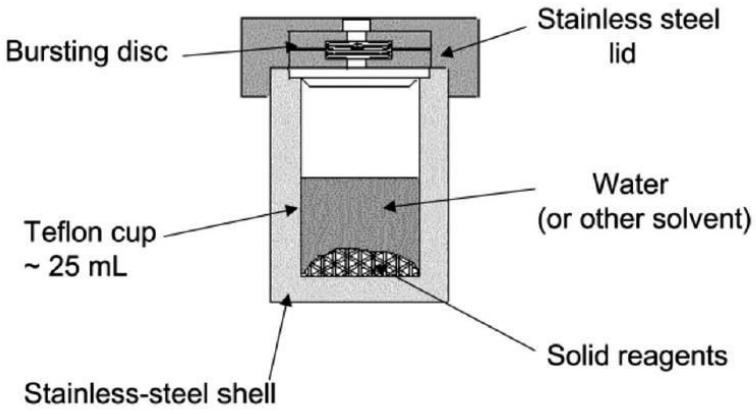

Figure 2.2: The construction of a hydrothermal autoclave is shown here. A typical autoclave consists of a removable Teflon cup inside a stainless steel shell with tight fixable stainless steel lid (*Reprinted with the permission of Chem. Soc. Rev., 2002, 31, 230–238*).

2.1.4 Chemical vapor deposition and chemical vapor synthesis

As the name implies, CVD is a deposition technique in which solid films are deposited from vapor phase by chemical reaction under very high temperature. It has been observed that these films under certain conditions contain ultrafine particles. So CVD can be used as a potential synthetic strategy for the synthesis of nanoparticles. To have an efficient nanoparticle synthesis, CVD has to tune in such a way that the conditions are to be high temperatures, high supersaturation, and long residence times, along with small substrates. So by tuning the reaction conditions in this way would lead to the synthesis of NPs instead of forming solid films and this process is known as chemical vapor synthesis or chemical vapor reaction. During synthesis, the precursors exist in three states were produced as vapors in the reactor which requires particles to undergo nucleation. This method can also be used to generate a multi-component or doped NPs. Figure 2.3 shows the schematic of general CVD instrument. [11-14]

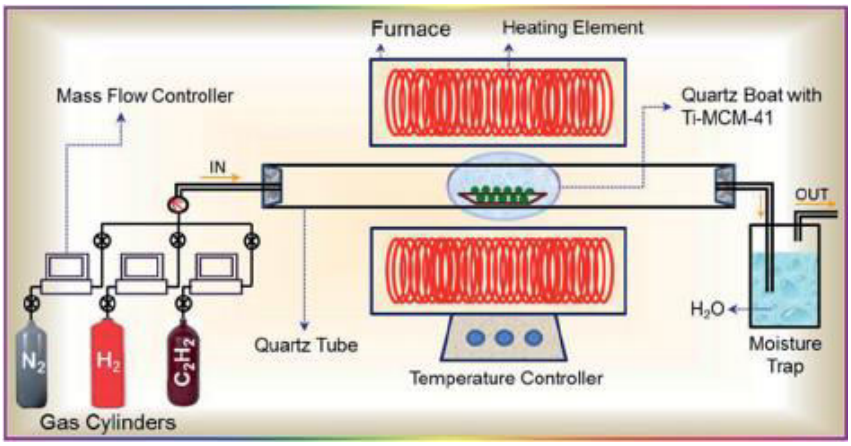

Figure 2.3: Schematic of a CVD instrument. (*Reprinted with the permission of RSC Adv., 2015, 5, 93364-93373).*

2.1.5 Microwave irradiation

Microwave chemistry has come into the limelight since it has been used in the preparative and material synthesis recently. In this method, a high frequency electric/magnetic field applied to a system which contains the electric/magnetic dipoles and mobile charges such as electrolytic solutions, polar solvents and molten salts. Hence, heat is generated by conversion of applied electric energy to heat energy by dipole rotation (electric /magnetic) and ionic conduction. Microwave irradiation provides a uniform heating to the material as compared to conventional heating where heat conduction occurs through the boundaries. Microwave strategy for the synthesis of various types of metal oxides (ZnO, TiO_2, and CeO_2), sulphides, and other one dimensional structures is already well documented. [15-17]

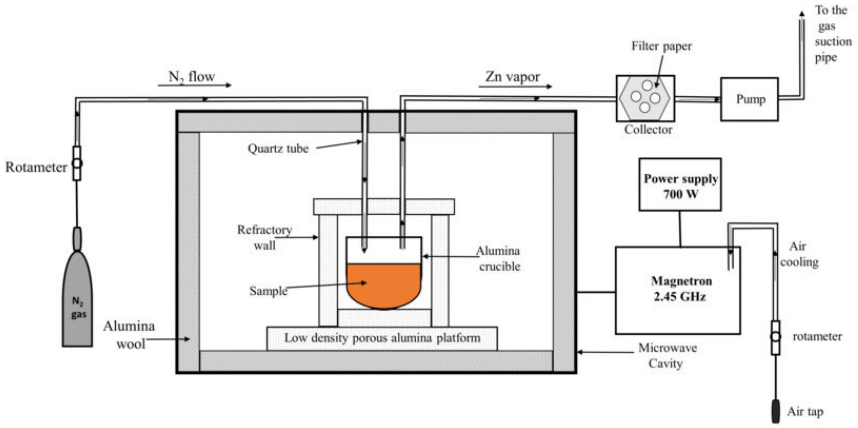

Figure 2.4: Schematic diagram of the microwave experimental setup (*Reprinted with the permission of R Soc Open Sci. 2017 Sep; 4(9): 170710).*

2.1.6 High temperature pyrolysis

High-Temperature Pyrolysis synthesis is used for large scale production of carbon materials. Carbon-containing precursors like lab synthesised high molecular weight compounds, synthetic and natural polymers and biomass are annealed at a high temperature of 600 to 2400 ^{0}C with different heating rate and dwelling time to produce charcoal, coke, porous and non-porous carbon. During heating, this method involves breakage of the existing bond between carbon and hetero atoms with the multiple bond formation of carbon atoms. [18, 19] On the increasing temperature, the content of heteroatoms decreases and the overall percentage of heteroatoms in the carbon material depends on the heating rate and the final temperature.

Tubular furnace has been used for the pyrolysis of material, in which carbon precursor kept in a tube made of either alumina or quartz. In tubular furnace, there is an inlet for the entrance of carrier gases like nitrogen and argon to maintain the inert environment inside the

tube and an outlet to pass these gases through the oil trap. Generation of bubbles in oil trap helps to maintain the proper gas flow through the tube. The furnace is associated with the programmable control unit to programme the ramping rate and the dwelling time of the annealing process.

Figure 2.5: Photograph of the tubular furnace used for the synthesis of carbon materials.

2.1.7 Laser-based synthesis

The laser-based preparation method includes exposure of organic molecules, biomass and polymer with high energy laser for a very short period of time. When carbon precursor comes in contact with the laser radiation then local heating effect leads to the breaking of bonds between carbon and other non-carbon atoms and removes the non-carbon atoms from the precursor. Simultaneously, heating from radiation also initiates the formation of new carbon-carbon bonds for the carbon backbone of nano/micro materials. This method has been used for the synthesis of different types of carbon materials like graphene, carbon dots, SWCNTs, diamond and hydrophobic carbon films. In this technique, appropriate heating can be maintained by varying wavelength, energy density and power density of laser. [20-23]

2.2 Characterization and measurement techniques

When material's dimensions are reduced to the nanoscale, they will exhibit different properties than their bulk counterparts. Thus, their structural, electronic and optical properties changed drastically when the size is reduced, such changes in the properties can make the analysis complicated at times. Further, a detailed study of nanomaterial's properties is very crucial in order to employ them for any specific applications. In general, nanomaterials characterization performed for investigation of their morphological (shape and size), microstructure (crystallinity, phase), composition (element analysis, phase), interface (surface area, surface charge), physiochemical (conductivity, density), transport (diffusion, convention) and functional properties and all these properties are interrelated. Therefore, it

is very important to select the appropriate characterization technique that provides precise and clear information about the nanomaterials under study.

2.2.1 Powder X-ray diffraction

X-ray powder diffraction is a rapid and non-destructive analytical technique routinely used as an initial and primary characterization for powdered microcrystalline samples in material science laboratory. [24-25] It reveals information about crystalline nature, phase purity, crystallite size, crystal planes, interlayer spacing, lattice parameters, and defects present in the lattice of nanomaterials. [26] Intensities of XRD peaks depend on atomic distribution within the 3D crystal lattice and their scattering power. Thus, the XRD pattern is the fingerprint of individual atoms present in the materials. X-ray diffractometers consist of mainly three components, first one is X-ray tube, which generates monochromatic X-rays beam, second is a sample compartment where the homogeneous nanomaterial under study is placed and the third one is X-ray detector which collects and detect the intensity of scattered X-ray.

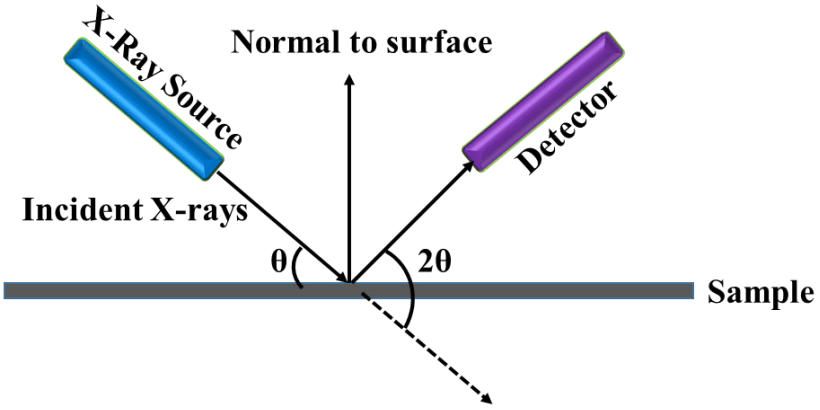

Figure 2.6: Schematic representation of X-ray diffractometer.

When a collimated monochromatic beam of X-rays falls on the sample, atoms present in the crystalline sample act as a diffraction grating and produces bright spots at certain angles (θ). These specific angles for bright spots can be measured and correlating to (hkl) planes of the crystalline sample by Bragg's law.

$$n\lambda = 2d\ sin\theta \text{.....2.1}$$

Where, n is a positive integer (order of diffraction), λ is the wavelength of the incident X-rays, d is the inter planer distance, and 'θ' is the scattering angle. When sample scanned through a range of 2θ angles, random alignment of powdered material produces all attainable diffraction patterns of the crystal lattice. Since, the value of θ and λ is experimentally known, inter planar spacing can be calculated by using the above Bragg's law equation. It permits the identification of the compound, their crystalline nature and phase

purity due to the distinctive set of d-spacing values for individual materials. Nanomaterials have smaller crystallites size and significant surface strains that can cause broadening of peak and little shift in the peak positions with respect to a standard reference. The average crystallite size (D) can be calculated by using Scherrer's formula, which is as follows: [27]

$$D = k\lambda/\beta cos\theta \text{.....2.2}$$

Where, k is Scherrer's Constant ≈ 0.9 (for spherical particles), λ is the wavelength of X-rays used, β is Full Width at Half Maximum (FWHM) of the peak corresponding to the diffraction angle θ after correcting for the instrumental contribution to the peak broadening,

$$\beta^2 = \beta_M^2 - \beta_S^2 \text{ .....2.3}$$

Where, β_M is the measured full width of a peak at half maximum for the sample, β_S is the instrumental input for peak broadening, and β is the peak broadening due to crystallite size.

In this study, all the powder X-ray diffraction patterns were collected from PANalytical XPERT PRO model X-ray diffractometer equipped with Cu Kα (1.5418 Å) radiation and Ni filter. XRD patterns of the synthesized samples were recorded in the 2θ range 10-80 degrees with the scan rate of 2 degrees/minute and obtained pattern was compared with the standard Joint Committee on Powder Diffraction Standards (JCPDS) data or international centre for diffraction (ICDD) data. [28]

2.2.2 Thermogravimetric analysis

Thermogravimetric analysis (TGA) is a classical destructive analytical technique in which weight loss or gain of a sample is measured as a function of temperature. [29, 30] The change in the weight of a sample is plotted against temperature, is called the thermogravimetric (TGA) curve. The rate of change in the mass can also be plotted against temperature, is called a differential thermogravimetric (DTG) curve. It provides information about physical properties, such as absorption, desorption of adsorbate molecules and phase transitions temperature of material; as well as chemical characteristics such as chemisorption and thermal decomposition of the material. Activation energies of the decomposition process can be measured by using the Kissinger method. [31] Thermogravimetric analyser contains a precision balance and a sample pan which is placed inside a programmable temperature controlled furnace. It is performed in various atmospheres like ambient air, inert gas, vacuum, oxidizing/reducing gases, corrosive gases, vapours or liquids or "self-generated atmosphere "; [32] with controlling the vacuum and pressure. In thermogravimetric data analysis, materials show weight loss when materials undergo desorption, decomposition, vaporization, oxidation, reduction, sublimation, etc. and weight gain is observed when materials form

stable solid oxides or compound with atmospheric molecules. Thermogravimetric analysis is not useful technique to find phase change temperature, in this situation differential scanning calorimetry (DSC) is used. [33] In the present study, thermogravimetric analysis of powder samples was carried out on an SDT Q600 TG-DTA analyser in the temperature range 25-1000 °C, at a heating rate 10 °C per minute, under air atmosphere.

2.2.3 Surface area measurement

Brunauer-Emmett-Teller (BET) analysis is a widely used non-destructive analytical technique to estimate surface area of materials. It gives the information of specific surface area, pore size distribution and heat of adsorption of a material. It works on the multilayer adsorption system unlike Langmuir theory (single layer adsorption). The specific surface area and pore size distribution of material are calculated by measuring the physical adsorption of gas molecules on a solid surface; like N_2 gas which is chemically inert with the material surface. There are three main hypotheses, which work during the adsorption-desorption process of gas in surface area measurement.

1. Multilayer adsorption of gas molecules takes place on a solid sample.
2. The interaction of gas molecules occurs with only adjacent layers; and
3. The Langmuir theory is applicable for one molecular layer.

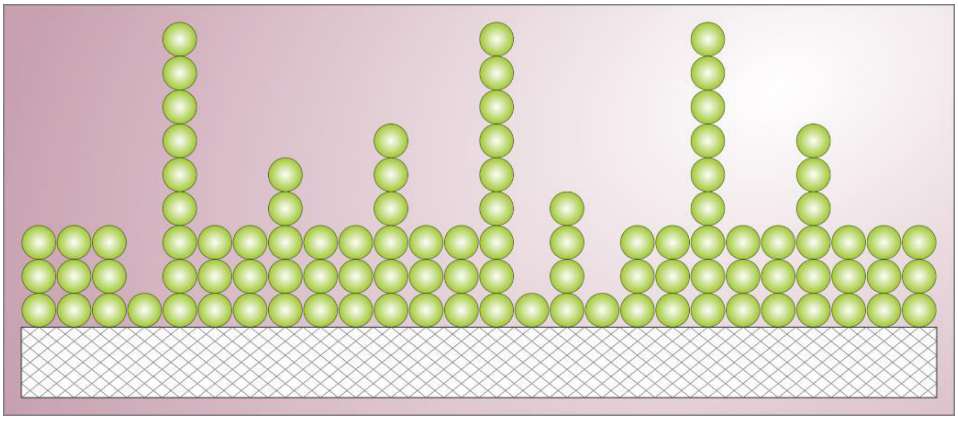

Figure 2.7: BET model showing the multilayer adsorption of gas molecules on the solid surface. The random distribution of sites covered with different number of adsorbed molecules. (*https://commons.wikimedia.org/wiki/File:BET_Multilayer_Adsorption.svg*)

Surface area measurement of the sample carried out by calculating multilayer adsorption of N_2 as a function of relative pressure. The resulting BET equation is as follows:

$$\frac{1}{v\left[\left(\frac{P_0}{P}\right)-1\right]} = \frac{C-1}{V_m C}\left(\frac{P}{P_0}\right) + \frac{1}{V_m c} \quad \text{.....2.4}$$

Where, V represents the adsorbed gas quantity, V_m represents the quantity of gas adsorbed to form a monolayer on the solid surface, P_0 is saturation pressure and P is the equilibrium pressures of adsorbate at the adsorption temperature and C is the BET constant.

The above equation 2.4 can be plotted as P / P_0 on the x-axis and 1 / v [(P_0 / P) − 1] on the y-axis. It gives a straight line at very low pressure range of 0.05 < P / P_0 < 0.35. This BET plot is also called as adsorption-desorption isotherm. [33-35] BET constant C can be calculated as follows-

$$C = \exp\left(\frac{E_1}{RT} - \frac{E_L}{RT}\right) \ldots\ldots\ldots\ldots 2.5$$

Where, E_1 is the heat of adsorption for the first layer and E_L is the heat of adsorption for the next and higher layer and is equal to the heat of liquefaction and heat of vaporization, respectively. The total surface area and specific surface area (SSA) is calculated by the following equation

$$S_{total} = \frac{(V_m N S)}{V} \ldots\ldots\ldots\ldots 2.6$$

$$S_{BET} = \frac{S_{total}}{a} \ldots\ldots\ldots\ldots 2.7$$

Where, V_m is the molar adsorbed gas volume experimentally obtained from the BET plot, N is Avogadro's number, S is the cross-section of the adsorbing species (N_2 as probe gas with 16.2 Å cross-section value), V is the volume of a gas molecule, and a is the adsorbent mass. Using adsorption-desorption isotherm, the porous nature of the sample can be analysed. Total pore volume is obtained from the amount of vapour of probe gas adsorbed at a relative pressure close to one by assuming pores are filled with liquid probe gas having same density as bulk liquid.

$$V_{liq} = \frac{PV_{ads}V_m}{RT} \ldots\ldots\ldots\ldots 2.8$$

Where, V_{ads} is the volume of gas adsorbed, V_m is the molar adsorbed gas volume, R, P, T have usual meaning, such as universal gas constant, the ambient pressure and temperature, respectively. Macro and mesopores are analysed by BJH method and micropores are analysed by DFT method. [36]

2.2.4 X-Ray photoelectron spectroscopy

X-ray photoelectron spectroscopy (XPS) is a non-destructive surface analytical technique. It is used to examine the oxidation state of metals, elemental composition, empirical formula and nature of chemical bonding between the elements that present in the nanomaterial. [37, 38] XPS is also known as electron spectroscopy for chemical analysis (ESCA). Al K_α and Mg K_α are used as X-ray sources, which emits the electron from atom present in the nanomaterial. The energy of incident photon ($h\nu$) and kinetic energy (KE) of

emitted electrons is experimentally known then the electron binding energy (BE) of emitted electrons can be calculated by using Ernest Rutherford equation:

$$BE = h\nu - (KE + \varphi) \text{.....2.9}$$

Where, h and ν are the Plank's constant and frequency of an incident photon respectively and φ is the work function. In XPS, the emitted electron from the material is counted and their kinetic energy is measured. The XPS spectra is plotted between electrons count and their kinetic energy. The binding energy of a core electron is used as a fingerprint for elemental analysis. The composition of the nanomaterial is estimated by using intensity and sensitivity factor, [39] the following general expression is used for composition calculation

$$C_i = \frac{I_i/S_i}{\Sigma_i^n I_i/S_i} \text{.....2.10}$$

Where, I is the peak intensity for the element i and S is the sensitivity factor for peak i.

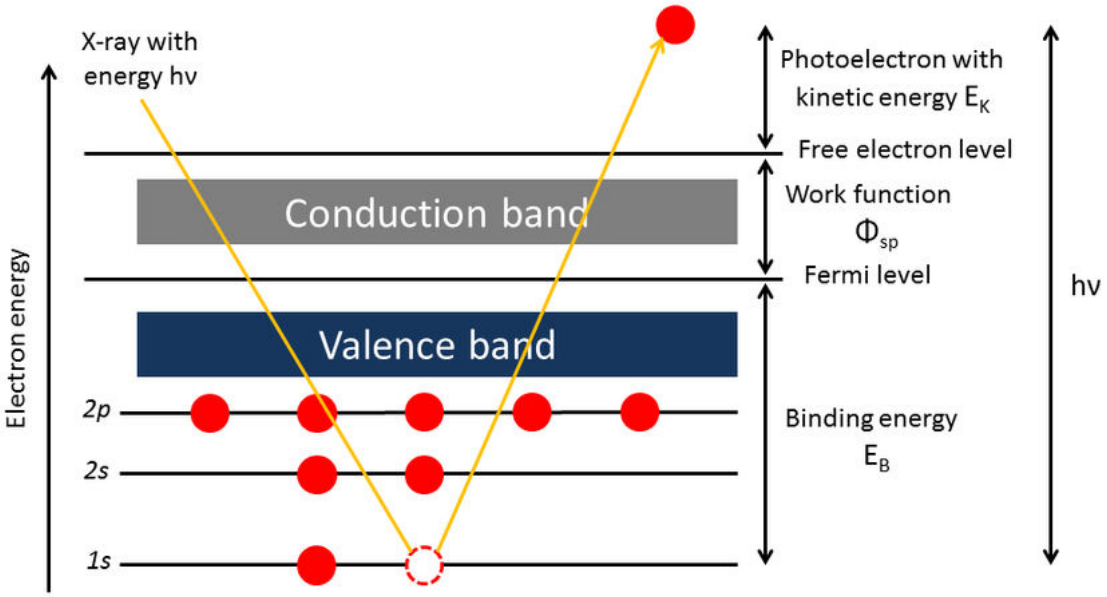

Figure 2.8 Schematic diagram of working principle of XPS.

(*Reprinted with the permission of A. Vandenbroucke, Diss. Ghent University, 2015*).

The schematic of working of XPS is shown in figure 2.8. XPS instrument consists of the X-ray source, a moderate vacuum sample introduction chamber, sample stage, an ultra-high vacuum (UHV) stainless steel chamber with UHV pumps, an electron collection lens, an electron energy analyzer, Mu-metal magnetic field shielding, an electron detector system.

XPS plot comprises the binding energy of electron detected on x-axis and intensity (number of electrons detected) on the y-axis. Each element shows a specific set of XPS peaks at their specific binding energy values to identify their presence in the material. In the present work, the XPS measurements of various samples were carried out on VG Microtech Multilab

ESCA-3000 spectrometer equipped with a nonmonochromatic Mg Kα X-ray (1253.6 eV) source.

2.2.5 Scanning electron microscopy

Scanning electron microscopy (SEM) is the non-destructive surface analytical tool. [40] Schematic diagram of the SEM shown in figure 2.9. A focused beam of high-energy electrons blasted on the sample surface at various depths, which produces a variety of signals. These signals collected and analysed to get the information about surface topography, crystalline structure, chemical composition, and orientation of materials. Raster scan pattern has been employed for electron beam scanning and then the image is being produced by correlating electron beam position and their detected signal intensity.

In SEM, elastically scattered secondary electrons are used for image topography which is detected by secondary electron detector. Also, this electron sample interaction produces back scattered electrons which are used for chemical composition analysis using Energy Dispersive X-rays Spectroscopy (EDS) technique. [41, 42] In the present work, Morphology and chemical composition of the samples were examined by using Quanta 200 3D, FEI scanning electron microscope (SEM).

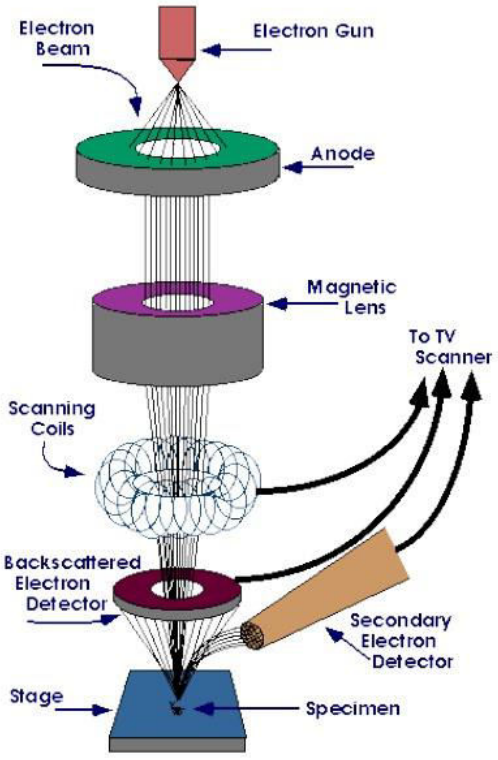

Figure 2.9: Scanning electron microscope.

(https://shambaditya2014.wordpress.com/scanning-electron-microscope/)

2.2.6 Transmission electron microscopy

Transmission electron microscopy (TEM) is the most powerful technique to characterize the nanostructured materials. High energy electrons beam is transmitted through a very thin film of the sample (< 100 nm) or a suspension on a grid to form an image. TEM can also be used to analyse the chemical composition at the sub-nanometer scale with the support of energy-dispersive X-ray spectroscopy (EDS) as a complementary technique. [43, 44] The schematic diagram of the TEM is shown in figure 2.10**.**

Selected area electron diffraction (SAED) pattern gives information about the angular distribution of scattering. It can be used to identify the crystalline nature of materials and crystal defects. Moreover, Kikuchi lines obtained by multiple diffractions within the crystalline lattice is also very useful for understanding the crystallographic orientation and sample thickness.

Sample preparation for TEM analysis is an essential part. TEM specimen should be very thin to transmit sufficient electrons with minimum energy loss. . In the present work, Transmission Electron microscopy was carried out by Tecnai F30 FEG machine operated at an accelerating voltage of 300 kV.

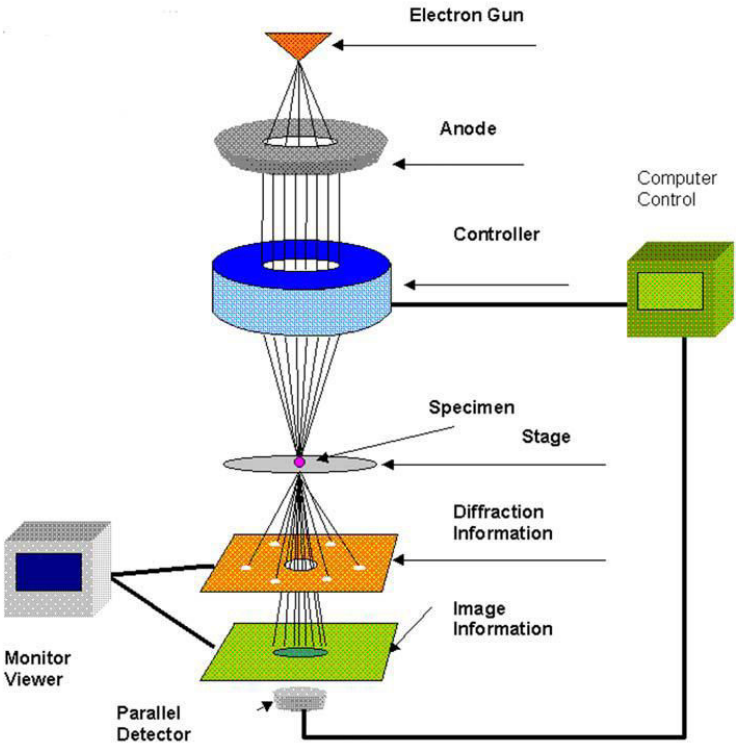

Figure 2.10: Schematic diagram of the Transmission Electron Microscope. (*http://www.rpi.edu/dept/materials/COURSES/NANO/shaw/Page5.html*)

2.3 Electrochemical characterization

2.3.1 Electrode fabrication and cell assembly

For the preparation of the electrode, first the right proportion of active material, conducting carbon and PVDF binder are blended and made into a slurry with NMP solvent. The above-prepared slurry has been coated on the metallic Cu foil using Elcometer bar coater and dried at 100ºC for overnight. The next step is hot roll pressing to guarantee a homogeneous surface of electrode material, to increase the particle-particle contact, and decrease the diffusion paths. Hot roll pressed electrode sheet was punched into many circular electrodes to fabricate electrochemical coin cells. Fabrication of coin cells performed inside the glove box in an inert atmosphere, where H_2O and O_2 level were maintained less than 1 ppm.

2.3.2 Electrochemical measurements

Current, voltage and time are the most important parameter in electrochemistry. All electrochemical processes occur at the interface between electrode and electrolyte. Electrodes are generally an electronically conductive solid material. The electrode has a certain Fermi level, which can be tuned by applying a positive or negative potential. Fermi level of the electrode is lowered by applying the positive potential to the electrode. In case of battery, when the Fermi level of electrode reduced to electrolyte solution potential, then electron transfer occurs from electrolyte to electrode and it is called the oxidation process.

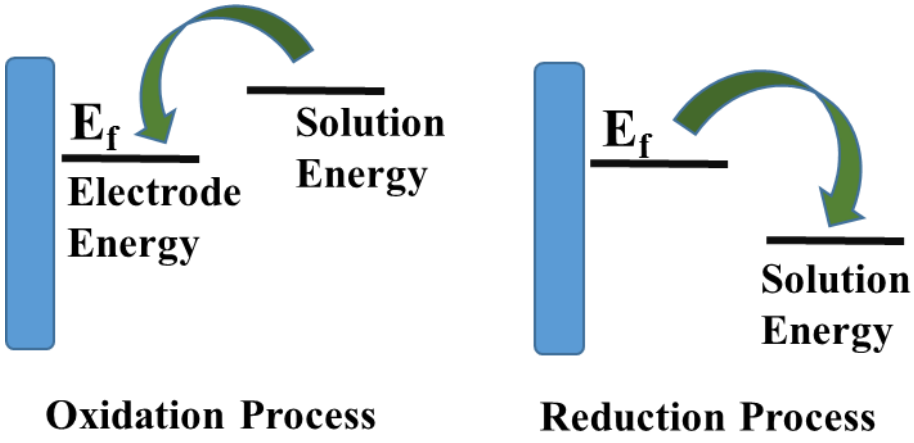

Figure 2.11: Schematic diagram of electrochemical oxidation and reduction process.

Once, the Fermi level of electrode rise above the electrolyte solution potential, then the electrons flow from electrode to electrolyte and it is called the reduction process. All the electrochemical techniques are based on the way of manipulating the electrode potential by means of applying the potential, current or both for predetermined time duration. [45-47]

2.3.2.1 Cyclic voltammetry

Cyclic voltammetry (CV) is a versatile and primary electroanalytical technique used to study the electro-active species. CV involves the linear scanning of the potential of a stationary working electrode using a triangular waveform. [48, 49] During the CV experiment, the potential at the working electrode is controlled against the reference electrode, the reference potential is constant throughout the experiment. The potential which is applied across the working electrode and counter electrodes is the excitation signal. The excitation signal varies linearly with time at a specific sweep rate. Initially, the potential is scanned in the positive direction and later the potential is scanned in reverse causing a negative scan back to the original voltage to complete the cycle. Hence it is called as cyclic voltammetry as shown in figure 2.12. In CV, resulting current measured during a potential sweep as a function of applied potential and this current-potential plot is known as Cyclic Voltammogram.

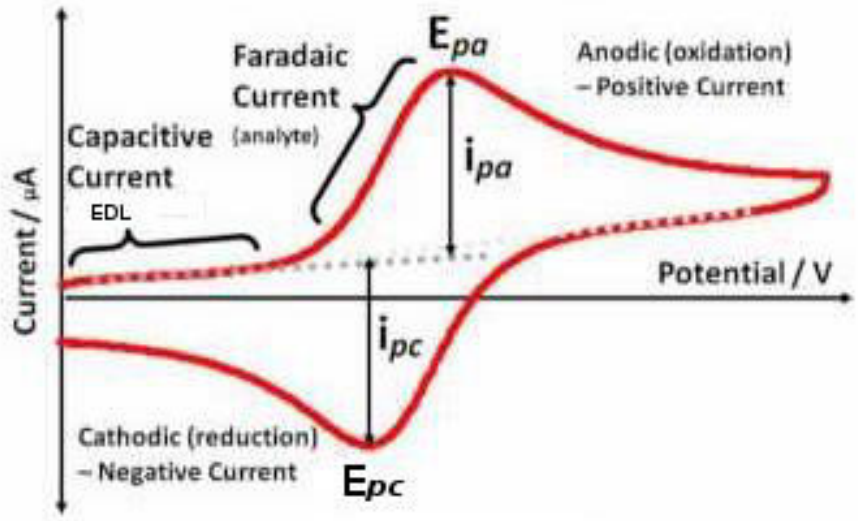

Figure 2.12: Cyclic voltammetry plot of a faradic system displaying peaks corresponding to redox reactions *(http://urrjaa.blogspot.com/2013/08/cyclic-voltammetry-urrjaa-p0110-2013.html)*.

The CV profile provides information about quantitative analysis of redox reactions. [50] It also provides information on various aspects such as thermodynamics of redox process, the kinetics of coupled reactions, the kinetics of heterogeneous electron transfer process, etc. In this study operating potential of the fabricated battery determined using CV experiment, it also gives the information about the kinetics of Faradic reaction and capacity fading of the material.

2.3.2.2 Charge-Discharge Measurement

Battery dynamic performance is determined by using a galvanostatic charge and discharge technique. The speed at which current can be put into and taken from battery is

called charge and discharge current rate, respectively. In the ideal battery, the voltage of the battery is constant throughout the constant current discharge experiment. [67] However, in real battery voltage rises and falls during charging and discharging. The charge and discharge dynamics of batteries can be characterized by measurements of voltage under constant charge and discharge current inputs. The potential drop is due to activation, and mass transport loss and they are dominating in particular depth of discharge are shown in figure 2.13 a. [68-69]

Battery discharged at low, medium and high rates is shown in figure 2.13 b. In high rate discharge, the battery voltage drops quickly and only a part of capacity can be realized than the lower rate discharge.

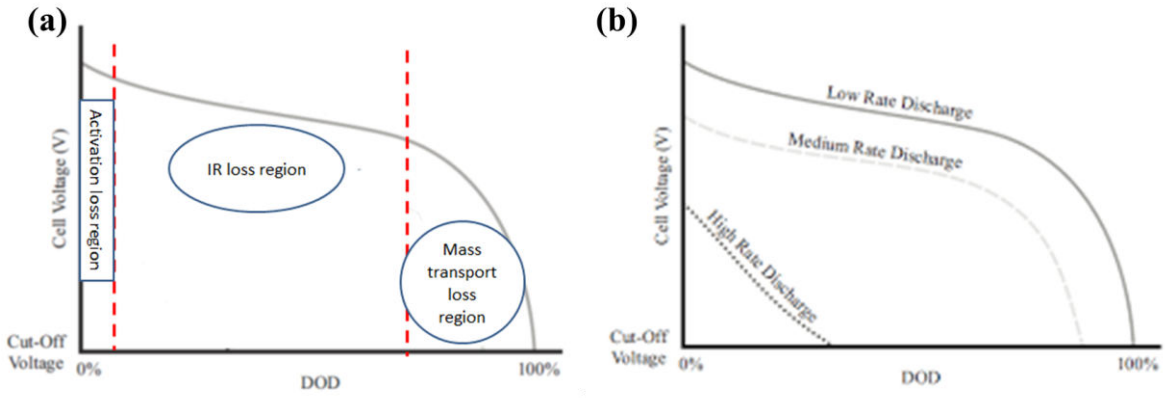

Figure 2.13: (a) Energy due to activation, IR and mass transport loss and they are dominating the region. (b) Example of voltage curves for different discharge rates (*Reprinted with the permission of Battery systems engineering, John Wiley & Sons, 2013*).

The coulombic efficiency (CE) of the lithium-ion battery calculated as follows. [54]

$$CE = \frac{Discharge\ Capacity}{Charge\ Capacity} \text{.....2.11}$$

2.3.2.3 Electrochemical Impedance Spectroscopy (EIS)

Cyclic voltammograms and Galvanostatic charge-discharge measurements required DC current source whereas EIS involved AC current source and EIS measurements setup is similar to the other above mentioned techniques. Like other spectroscopic techniques (UV, FTIR etc), in EIS measurement, the response is noted after applying electrical frequency in the range of mHz to KHz. EIS has been used for the study of the electrochemical reaction mechanism, kinetics and thermodynamics of several redox reactions. Additionally, EIS measurements quantitatively characterize the interfacial behaviours of electrode and electrolyte. The EIS spectral data were investigated with the help of Nyquist plot, in which, X-axis represents the real part of the impedance and Y-axis represents the imaginary part. [55, 56] The Nyquist plot can portray the real-time changes occurring at the interfaces during charging-discharging. Semicircles appear in high-frequency region attribute to faradic

resistance or charge transfer resistance, straight line in the low-frequency region indicates the diffusive nature of ions in cell assembly. In the Nyquist plot, a region where the first frequency point cut occurs is due to the electrolyte and contact resistance R_S. For better performance of the device, the semicircle diameter (R_{ct}) and R_s of impedance spectra should be minimum. The straight line in the low-frequency region should be parallel to Y axis for fast diffusion of ions in the device. The Nyquist plot and its corresponding equivalent circuit of the LIBs is shown below in figure 2.14 (a) and 2.14 (b), respectively. [54, 57]

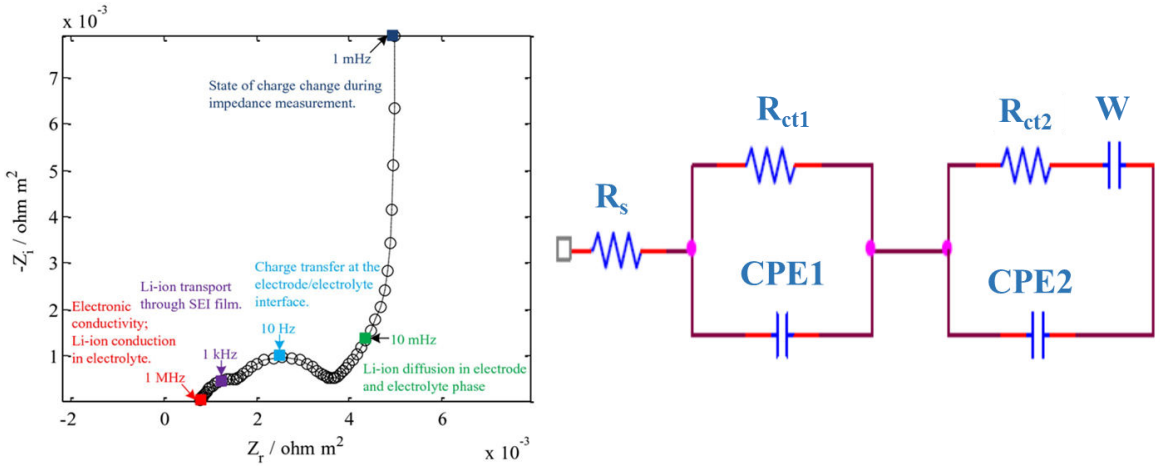

Figure 2.14: (a) Nyquist Plot (b) Equivalent circuit of Li-ion battery (*Reprinted with the permission of J. Electrochem. Soc., 2015, 162, A7037-A7048*).

Where R_{ct}, (including R_{ct1} and R_{ct2}), is internal resistance of electrochemical reaction. R_s is series resistance and the CPE (including CPE1 and CPE2) is battery polar plate's surface electric double layer capacitance, correlated with battery capability. In this study, the EIS data collected at open circuit voltage in galvanostatic mode.

2.4 References

[1] C. J. Brinker and G. W. Scherer, *Sol-gel science: the physics and chemistry of sol-gel processing*, Academic press, 2013.

[2] M. A. Behnajady, H. Eskandarloo, N. Modirshahla and M. Shokri, *Desalination*, 2011, **278**, 10–17.

[3] M. Aziz, S. S. Abbas and W. R. W. Baharom, *Mater. Lett.*, 2013, **91**, 31–34.

[4] J. N. Solanki and Z. V. P. Murthy, *Ind. Eng. Chem. Res.*, 2011, **50**, 12311–12323.

[5] M. A. Malik, M. Y. Wani and M. A. Hashim, *Arab. J. Chem.*, 2012, **5**, 397–417.

[6] N. Murayama, H. Yamamoto and J. Shibata, *Int. J. Miner. Process.*, 2002, **64**, 1–17.

[7] C. S. Cundy and P. A. Cox, *Microporous mesoporous Mater.*, 2005, **82**, 1–78.

[8] A. Lagazzo, E. Finocchio, P. Petrini, C. Ruggiero and L. Pastorino, *Mater. Lett.*, 2016, **171**, 212–215.

[9] M. M. Titirici, A. Thomas, S.-H. Yu, J.-O. Müller and M. Antonietti, *Chem. Mater.*, 2007, **19**, 4205–4212.

[10] B. Hu, K. Wang, L. Wu, S. Yu, M. Antonietti and M. Titirici, *Adv. Mater.*, 2010, **22**, 813–828.

[11] M. T. Swihart, *Curr. Opin. Colloid Interface Sci.*, 2003, **8**, 127–133.

[12] S. Polarz, A. Roy, M. Merz, S. Halm, D. Schröder, L. Schneider, G. Bacher, F. E. Kruis and M. Driess, *Small*, 2005, **1**, 540–552.

[13] S. Hartner, M. Ali, C. Schulz, M. Winterer and H. Wiggers, *Nanotechnology*, 2009, **20**, 445701.

[14] Y. Li, J. Liu, Y. Wang and Z. L. Wang, *Chem. Mater.*, 2001, **13**, 1008–1014.

[15] M. Hasanpoor, M. Aliofkhazraei and H. Delavari, *Procedia Mater. Sci.*, 2015, **11**, 320–325.

[16] W. X. Chen, J. Y. Lee and Z. Liu, *Chem. Commun.*, 2002, 2588–2589..

[17] S. Wang, S. P. Jiang and X. Wang, *Electrochim. Acta*, 2011, **56**, 3338–3344.

[18] A. G. Pandolfo and A. F. Hollenkamp, *J. Power Sources*, 2006, **157**, 11–27.

[19] Y. Zhu, S. Murali, M. D. Stoller, K. J. Ganesh, W. Cai, P. J. Ferreira, A. Pirkle, R. M. Wallace, K. A. Cychosz and M. Thommes, *Science*, 2011, **332**, 1537–1541.

[20] F. C. B. Maia, R. E. Samad, J. Bettini, R. O. Freitas, N. D. V. Junior and N. M. Souza-Neto, *Sci. Rep.*, 2015, **5**, 11812.

[21] R. Gokhale, S. Agarkar, J. Debgupta, D. Shinde, B. Lefez, A. Banerjee, J. Jog, M. More, B. Hannoyer and S. Ogale, *Nanoscale*, 2012, **4**, 6730–6734.

[22] S.-L. Hu, K.-Y. Niu, J. Sun, J. Yang, N.-Q. Zhao and X.-W. Du, *J. Mater. Chem.*, 2009, **19**, 484–488.

[23] C. T. Kingston, Z. J. Jakubek, S. Dénommée and B. Simard, *Carbon N. Y.*, 2004, **42**, 1657–1664.

[24] B. D. Cullity, *Am. J. Phys.*, 1957, **25**, 394–395.

[25] V. Pecharsky and P. Zavalij, *Fundamentals of powder diffraction and structural characterization of materials*, Springer Science & Business Media, 2008.

[26] A. R. West, *Solid state chemistry and its applications*, John Wiley & Sons, 2014.

[27] A. L. Patterson, *Phys. Rev.*, 1939, **56**, 978.

[28] X. Zhou, D. Liu, H. Bu, L. Deng, H. Liu, P. Yuan, P. Du and H. Song, *Solid Earth Sci.*, 2018, **3**, 16–29.

[29] A. W. Coats and J. P. Redfern, *Analyst*, 1963, **88**, 906–924.

[30] T. Ozawa, *Thermochim. Acta*, 2000, **355**, 35–42.

[31] P. E. Sánchez-Jiménez, J. M. Criado and L. A. Pérez-Maqueda, *J. Therm. Anal. Calorim.*, 2008, **94**, 427–432.

[32] A. E. Newkirk, *Thermochim. Acta*, 1971, **2**, 1–23.

[33] E. Lopez-Capel, S. P. Sohi, J. L. Gaunt and D. A. C. Manning, *Soil Sci. Soc. Am. J.*, 2005, **69**, 136–140.

[34] D. Dollimore, P. Spooner and A. Turner, *Surf. Technol.*, 1976, **4**, 121–160.

[35] K. S. Walton and R. Q. Snurr, *J. Am. Chem. Soc.*, 2007, **129**, 8552–8556.

[36] E. P. Barrett, L. G. Joyner and P. P. Halenda, *J. Am. Chem. Soc.*, 1951, **73**, 373–380.

[37] A. Cros, *J. Electron Spectros. Relat. Phenomena*, 1992, **59**, 1–14.

[38] I. Lindgren, *J. Electron Spectros. Relat. Phenomena*, 2004, **137**, 59–71.

[39] C. J. Powell and A. Jablonski, *Surf. Interface Anal.*, 2000, **29**, 108–114.

[40] J. I. Goldstein, D. E. Newbury, J. R. Michael, N. W. M. Ritchie, J. H. J. Scott and D. C. Joy, *Scanning electron microscopy and X-ray microanalysis*, Springer, 2017.

[41] L. Reimer, *Scanning electron microscopy: physics of image formation and microanalysis*, Springer, 2013, vol. 45.

[42] W. Zhou and Z. L. Wang, *Scanning microscopy for nanotechnology: techniques and applications*, Springer science & business media, 2007.

[43] D. B. Williams and C. B. Carter, in *Transmission electron microscopy*, Springer, 1996, pp. 3–17.

[44] B. Fultz and J. M. Howe, *Transmission electron microscopy and diffractometry of materials*, Springer Science & Business Media, 2012.

[45] A. J. Bard and L. R. Faulkner, *Electrochem. Methods*.

[46] R. C. Alkire, Y. Gogotsi and P. Simon, *Nanostructured materials in electrochemistry*, John Wiley & Sons, 2008.

[47] D. Pletcher, R. Greff, R. Peat, L. M. Peter and J. Robinson, *Instrumental methods in electrochemistry*, Elsevier, 2001.

[48] P. T. Kissinger and W. R. Heineman, *J. Chem. Educ.*, 1983, **60**, 702.

[49] J. F. Rusling and S. L. Suib, *Adv. Mater.*, 1994, **6**, 922–930.

[50] R. S. Nicholson, *Anal. Chem.*, 1965, **37**, 1351–1355.

[51] A. Nyman, T. G. Zavalis, R. Elger, M. Behm and G. Lindbergh, *J. Electrochem. Soc.* , 2010, **157**, A1236–A1246.

[52] Y. Yamada, M. Yaegashi, T. Abe and A. Yamada, *Chem. Commun.*, 2013, **49**, 11194–11196.

[53] B. Scrosati, F. Croce and S. Panero, *J. Power Sources*, 2001, **100**, 93–100.

[54] C. D. Rahn and C.-Y. Wang, *Battery systems engineering*, John Wiley & Sons, 2013.

[55] E. Barsoukov and J. R. Macdonald, *Impedance spectroscopy: theory, experiment, and applications*, John Wiley & Sons, 2018.

[56] U. Tröltzsch, O. Kanoun and H.-R. Tränkler, *Electrochim. Acta*, 2006, **51**, 1664–1672.

[57] D. Andre, M. Meiler, K. Steiner, H. Walz, T. Soczka-Guth and D. U. Sauer, *J. Power Sources*, 2011, **196**, 5349–5356.

Chapter 3

$Ni(OH)_2$-Fe_2O_3/CNOs Ternary Nanocomposite Designed as an Anode with Complementary Properties for High-Performance Li-ion Battery

Synthesis of the new ternary hybrid composite with excellent electrochemical performance for Li-ion battery is demonstrated. The ternary hybrid composite of $Ni(OH)_2$-Fe_2O_3/Carbon Nano Onions (NFOC) is synthesized by using two-step solution phase method delivers a high reversible discharge capacity of 928 $mAhg^{-1}$ at 50 $mAg^{-1}$and 673 $mAhg^{-1}$ at a higher current density of 1000 mAg^{-1} with excellent rate performance. Additionally, it shows stable cycle life up to 1000 cycles with 96% capacity retention and more than 99% of coulombic efficiency. The synergetic effect between $Ni(OH)_2$, Fe_2O_3 and carbon nano onions (CNOs) as well as the unique feature of heterostructures are responsible for the improved electrochemical performance of the battery. The reversible reaction of Fe_2O_3 and $Ni(OH)_2$ with Li, maintains its long cycle life with higher reversible discharge capacity and CNOs improves the efficient electronic transfer, accommodate substantial volume expansion and maintain the structural integrity of the material during lithiation-delithiation process.

3.1 Introduction

Recently, the importance of renewable energy sources has increased with gradually limiting conventional sources of fossil fuel. Most of the renewable energy sources like solar energy or wind energy are intermittent and need high energy density storage devices to be used when required. Additionally, technological advances in electronics and transportation pushes forward the requirement of suitable energy storage options. So far, lithium-ion batteries (LIBs) have occupied a primary position in fulfilling energy storage requirements in the electronic applications, principally for their high energy density and long cycle life with good coulombic efficiency. To meet the ever-changing energy storage requirements, it becomes necessary to work on active materials like anode, cathode or electrolyte materials, to increase their relative performance in a battery. Especially, anode materials are more important to increase energy density as well as power density of LIBs. Mostly, battery research is focused on developing novel electrode materials which possess properties like high energy density, high rate capability along with longer cycle life to replace conventional graphite anode materials.[1, 2] Since the introduction of LIBs, graphite has been widely used anode material for LIBs, owing to its less redox potential towards Li-ion as well as superior stability along with the theoretical specific capacity of ~372 $mAhg^{-1}$. However, comparatively low specific capacity of graphite and other carbon materials compels to look for alternative materials. Potential alternatives to intercalation carbonaceous materials are Li-alloying materials such as Si, Ge. and/or conversion materials like transition metal oxides.[1] Transition metal oxides are promising anode materials for their high theoretical capacity (~1000 $mAhg^{-1}$). In conversion reaction, Li-ons react reversibly with metal oxide which involves the formation and decomposition of Li_2O resulting in the reduction and oxidation of metal oxides as in following equation 1.[3,4]

$$M_xO_y + 2yLi^+ + 2ye^- \leftrightarrow yLi_2O + xM \ldots\ldots\ldots\ldots (1)$$

The forward reaction is thermodynamically favorable and involves multiple electron transfer per unit of metal atoms leading to high theoretical lithium storage. However, significant volume expansion occurs during Lithiation/delithiation, which perhaps leads to the cracking and pulverization of the electrode owing to internal strain. Also, many particular phases of oxides have low electronic conductivity. These issues with transition metal oxides reflect in the form of low rate capability and poor cyclic behavior of the electrode. Hybrid materials' systems comprising different transition metal oxides are proposed to alleviate these problems.[5-8] Hybridization can integrate multiple functional materials with complementary properties that can potentially improve electrical as well as ionic conductivity, mechanical

stability and electrochemical reactivity of overall electrode. The hybridization concept efficiently being applied in the LIBs and mostly the enhancement in the performance can be achieved by overcoming the limits of one material in the composite by the other.[9, 10] Apart from the metal oxides, recently, metal hydroxides are also being investigated as electrode materials for the LIBs. It is hypothesized that hydroxyl group gives an additional reversible capacity by the formation of LiOH followed by Li_2O at relatively lower voltages.[11, 12] However, these studies are scant and still at nascent level. More investigation of the lithium storage capabilities of these hydroxides are required to understand and improve their electrochemical performance in LIBs. A couple of studies have reported $Ni(OH)_2$ as an active anode material for LIB, but its low electrical conductivity (10 to 17 Scm^{-1}) leads to the rapid capacity fade at a higher current density in addition to volume expansion and contraction issue causing poor cycling stability.[13] Conversely, $Ni(OH)_2$ has many advantages like high natural abundance, low cost and less toxicity.[14, 15] To use the suitable properties of $Ni(OH)_2$ more effectively an approach of making a composite with carbon has been proposed.[16] It has been demonstrated that carbon coating can significantly enhance the electronic conductivity of electrode materials and provide cycle stability. Subsequently, a composite of reduced graphene oxide and $Ni(OH)_2$ showed specific discharge capacity of 507 $mAhg^{-1}$ at 200 mAg^{-1} after 30 cycles. [15] Nanowalls of $Ni(OH)_2$/Ni composite exhibited specific capacity of 0.59 $mAhcm^{-1}$ on completion of 100 cycles.[16] Nanoflakes of $Ni(OH)_2$/ RGO composite, synthesized by co-precipitation method, showed the specific capacity of 1003 $mAhg^{-1}$after 40 cycles at 100 mAg^{-1}.[17] Nevertheless, these materials are still facing unsatisfactory specific capacity and cycle lifetime, particularly at higher current density. Therefore, instead of these binary $Ni(OH)_2$/Carbon composites, it would be intriguing to explore ternary composite by adding a metal oxide to provide oxide/hydroxide/carbon kind of synergistic assembly. Such an assembly can potentially alleviate aggregation of metal hydroxide and metal oxide while increasing the overall conductivity of the composite, leading to substantial enhancement in capacitance as well as cycle life of a battery. Among metal oxides, iron oxide has excellent potential as an anode material for LIB because of its excellent theoretical capacity (~1007 $mAhg^{-1}$ for Fe_2O_3 and ~924 $mAhg^{-1}$ for Fe_3O_4), low cost, and environmental benignity. [5, 6] However poor charge/ion transport kinetics restricts battery performance of this material. Considering all these advantages and issues we have conceived an idea to develop ternary nanocomposite including $Ni(OH)_2$, Fe_2O_3 and carbon wherein each component will play a role to enhance the complementary properties of each other while leading to overall enhancement in its performance as an anode for LIB.

Here, we have synthesized an excellent ternary hybrid composite of $Ni(OH)_2$-Fe_2O_3/CNOs as an anode material for LIB with longer cycle life and superior rate capability. The combination of both transition metal oxides and metal hydroxide in the electrode leads to their sequential volume expansion, and they do not expand simultaneously, therefore, provides mechanical support to each other during lithiation and delithiation avoiding sizeable structural stress. Additionally, the long conductive chains of CNOs act as percolating network which is suitable for the efficient electronic transfer and spacing of the nanostructures for expansion/contraction during charge-discharge operation. When tested as an electrode for LIB, this ternary composite material showed good specific capacity and cycling stability.

3.2 Experimental section

3.2.1 Synthesis of $Ni(OH)_2$-Fe_2O_3/CNOs composites

CNOs were synthesized by collecting black carbon from the flame of the burning ghee followed by annealing at 800 ^oC for 3 hours in an inert atmosphere, thereby carbon black turns into multishell graphitized CNOs.[18] In a typical synthesis of the ternary composite, as prepared CNOs were first dispersed in N, N-dimethyl formamide (20 ml) followed by sonication for 10 minutes to uniformly disperse the CNOs in the solvent. 90mg of Methenamine was then added to above solution under vigorous stirring for 10 min followed by the addition of 800 µl aqueous solutions of 0.2M $Ni(NO_3)_2.6(H_2O)$ and 0.2M $Fe(NO_3)_3.9H_2O$ respectively. Stirring was continued for 5 h at a temperature of 90 ^oC and then allowed to cool. Then this uniformly dispersed solution was transferred into a 40 ml Teflon lined stainless steel autoclave to carry out a solvothermal reaction at 160 ^oC for 5 hours. Then the product was washed several times with DI water. This ternary composite product, i.e., $Ni(OH)_2$-Fe_2O_3/CNOs is named as NFOC. For comparison, a binary composite containing only $Ni(OH)_2$-Fe_2O_3 was synthesized by above procedure without the addition of CNOs and named as NFO, $Ni(OH)_2$ nanosheets and Fe_2O_3 nanoparticles are synthesized individually by a same solvothermal process using $Ni(NO_3)_2.6(H_2O)$ and $Fe(NO_3)_3.9H_2O$ separately. Different composites of CNOs with NFO were synthesized by varying the corresponding weight of the CNOs such as 10, 20, and 30 mg and as resulted composites are named as NFOC-10, NFOC-20, and NFOC-30 respectively. These synthesis routes are depicted schematically in figure 3.1.

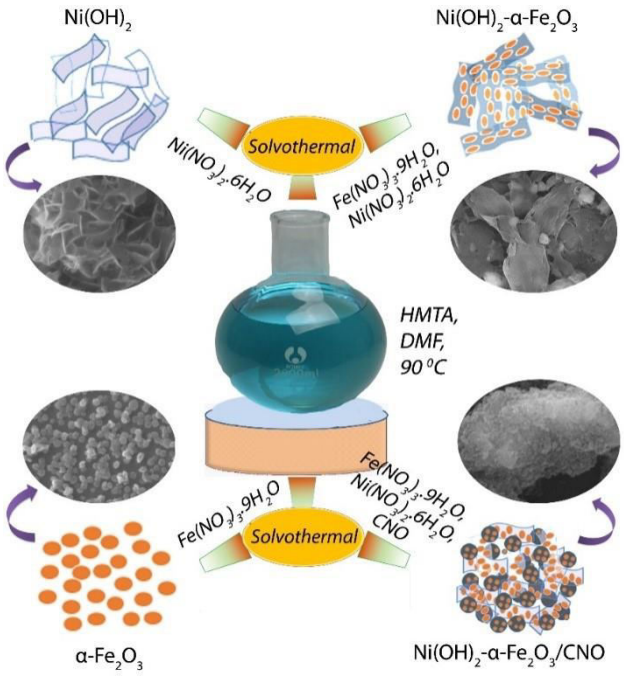

Figure 3.1: Schematic representation of the overall synthetic route towards the formation of $Ni(OH)_2$, α-Fe_2O_3, $Ni(OH)_2$-α-Fe_2O_3 and $Ni(OH)_2$-α-Fe_2O_3/CNO.

3.2.2 Material Characterization

Powder X-ray Diffraction patterns were recorded on a Phillips PAN analytical diffractometer with CuKα radiation (λ = 1.5406 Å). Transmission Electron microscopy was carried out by Tecnai F30 FEG machine operated at an accelerating voltage of 300 kV. Morphology and chemical composition of the ternary hybrid composite were examined by using Quanta 200 3D, FEI scanning electron microscope (SEM). X-ray photoelectron spectroscopic (XPS) measurements were carried out on a VG Micro Tech ESCA 3000 instrument. Thermogravimetric analysis were performed with SDT model Q600 of TA instrument with heating rate at 10degree per minutes in air atmosphere.

3.2.3 Electrochemical Characterization

The electrochemical properties of the ternary composite NFOC are examined by two-electrode coin cell (CR2016) configuration. The composite anode was prepared by mixing the active material NFOC with the conductive additive (super P) and the binder(polyvinylidene difluoride, PVDF).This mixture was coated on Cu foil, which serves as a current collector, subsequently dried at 90ºC overnight before making a cell assembly in an Ar-filled glovebox. The coin cells were assembled by using lithium metal foil as a counter electrode, a quartz microfiber paper (Whatman) as a separator and 1 M $LiPF_6$ in ethylene carbonate (EC)–diethyl carbonate (DEC) (1: 1 by volume) as an electrolyte. Cyclic voltammetry (CV) was performed using SP-300 EC Biologic potentiostat at a scan rate of 0.25 mVs^{-1} between 5 mV and 3.0 V. The galvanostatic discharge-charge cycling of the cells

was carried out at different current densities between potentials of 0.005 and 3.0 V by using MTI battery analyzer. The electrochemical impedance spectroscopy (EIS) was used to measure impedance in the frequency range from 100 KHz to 50 mHz with an AC amplitude of 10 mV.

3.3 Results and discussion

3.3.1 Powder X-ray diffraction

The crystalline structure and phase purity of the electrode materials were analysed by p-XRD, and the corresponding diffraction patterns are shown in the figure 3.2. In the diffraction pattern of CNOs, two diffraction peaks are observed at 24.5°, and 44.0° corresponds to the (002) and (001) planes of the graphitized carbon, respectively. From the diffraction patterns of $Ni(OH)_2$ and Fe_2O_3, it was observed that the corresponding diffraction planes at the respective 2 theta values are for the hexagonal phase [JCPDS no. 22-0444] of the $Ni(OH)_2$ nanosheets along with a space group of $P\bar{3}1m$ (no. 162) and rhombohedral phase [JCPDS no. 84-0306] of the Fe_2O_3 nanoparticles along with the space group of $R\bar{3}c$ (no.167) . From the diffraction patterns of the hybrid samples (NFO and NFOC), it was observed that the diffraction planes of $Ni(OH)_2$ and Fe_2O_3 were appeared without shift in the 2 theta values confirming that there is no formation of mixed phase oxide or hydroxides (bimetallic oxide or hydroxide). Apart from that no other peaks of impurities were detected, demonstrating that materials with high purity could be obtained under controlled experimental conditions.

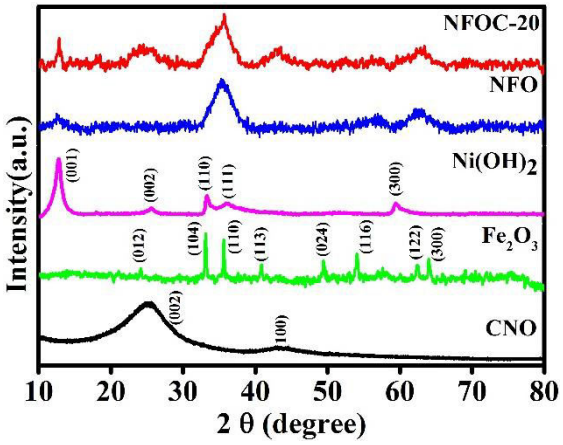

Figure 3.2: p-XRD pattern of CNO, Fe_2O_3, $Ni(OH)_2$, , NFO and NFOC-20

3.3.2 X-Ray photoelectron spectroscopy

XPS analysis was performed for the binary and ternary composite material (NFO & NFOC), to know the oxidation state of the metal ion as well as elemental composition in the composite. The survey scan spectra of NFO and NFOC in the range of 0-1000 eV is shown in the figure 3.3a, and the high-resolution elemental scan spectra of Fe 2p, Ni 2p, C1s and O1s in the ternary composite material are shown in figure 3.3 (b-e). Ni $2P_{3/2}$ and Ni $2P_{1/2}$ peaks at

binding energies of 855.3 eV and 873.0 eV with the spin-energy splitting of 17.7 eV along with the satellite peaks at 861.1 eV are observed in the Ni 2p elemental spectra confirming the presence of Ni in +2 oxidation state.[19] XPS results are in agreement with p-XRD studies of $Ni(OH)_2$. Elemental spectra of Fe2p shows the presence of Fe $2P_{3/2}$ and Fe $2P_{1/2}$ peaks at the binding energies of 711.3 eV and 724.6 eV along with the satellite peak in between these peaks, confirms that Fe is in +3 oxidation state. [20] The elemental spectra of C 1s consist of five deconvoluted peaks at 284.4, 285.6, 286.3, 287.3 and 289.3 eV. The high intense peak obtained at 284.4 eV of the binding energy confirms the presence of the sp^2 hybridized C–C bond; the other peaks at 285.6 eV, 286.3, 287.3 and 289.3 eV demonstrate the presence of sp^3 hybridized C–C, C– O (epoxy), C–OH and O-C=O bonds in CNOs, respectively. [21-23] O 1s spectra of the ternary composite (figure 3.3e) is deconvoluted into 4 peaks at 532.7, 531.7, 530.6 and 529.3 eV assigned to the hydroxyl oxygen, surface adsorbed oxygen and lattice oxygen, respectively. [24]

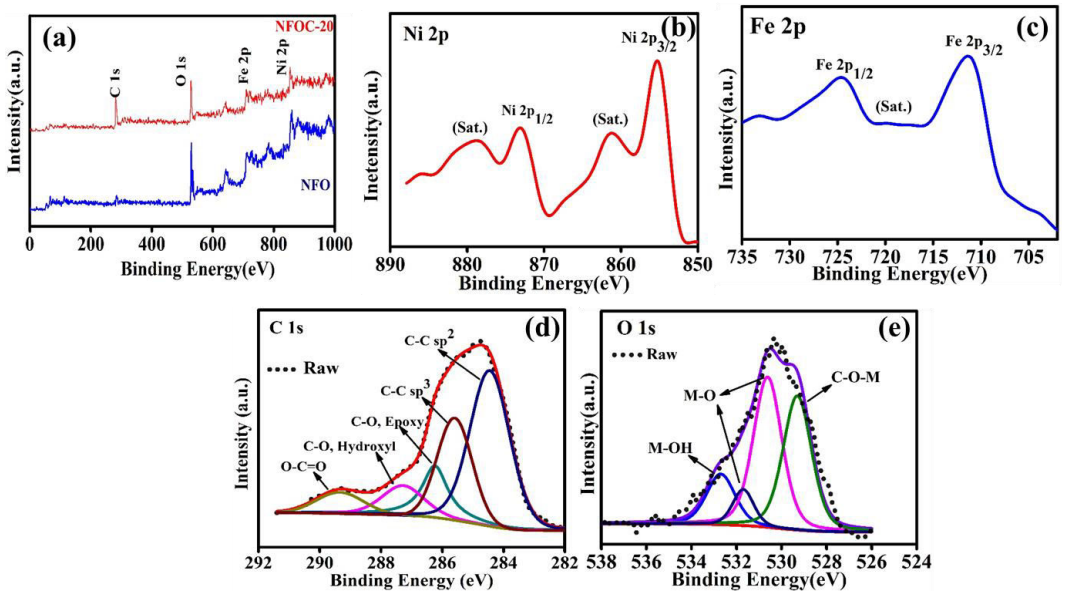

Figure 3.3: (a) XPS survey spectrum of NFOC-20 (b-e) XPS spectra of Fe 2p, Ni 2p, C 1s, and O 1s, respectively.

3.3.3 Scanning electron microscopy

The structural morphology of the as-prepared materials is studied by FESEM, and the corresponding images are shown in figure 3.4. SEM images (figure 3.4a and 3.4b) show that Fe_2O_3 nanoparticles are agglomerated and $Ni(OH)_2$ have nanosheets like morphology with several irregular interspaces. The SEM image of NFO (figure 3.4c) indicates that Fe_2O_3 nanoparticles are decorated on the $Ni(OH)_2$ nanosheets. SEM image of ternary composite NFOC-20 (figure 3.4d) shows that addition of CNOs has made the composite very dense and compact in arrangements. Fe_2O_3 decorated $Ni(OH)_2$ nanosheets are wrapped on and in

between CNOs that can potentially reduce the cracking and pulverization of active material during lithiation/delithiation. The higher resolution SEM images are shown in the inset of figure 3.4(a-d). SEM elemental mapping of Ni, Fe, C and O (figure 3.5) taken at the same area on the ternary composite is demonstrating the homogeneous distribution of all the elements in the ternary composite.

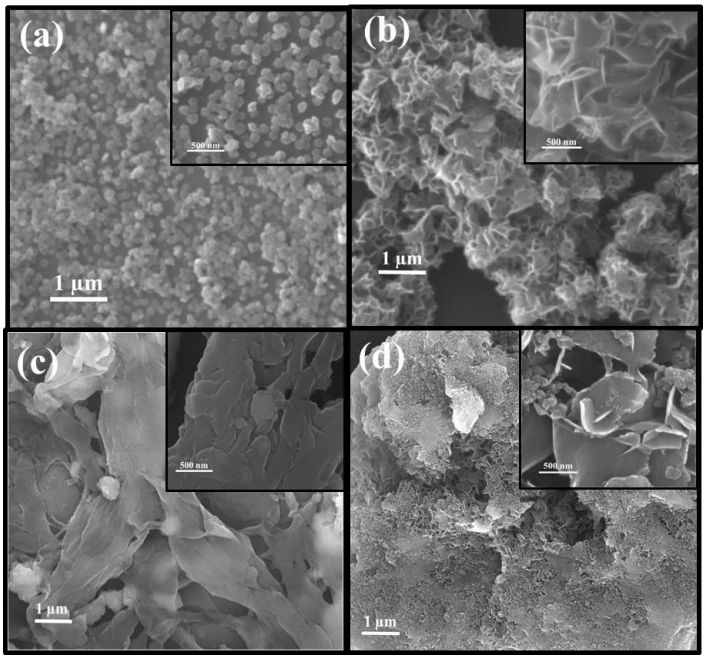

Figure 3.4: SEM images of (a) Fe_2O_3, (b) $Ni(OH)_2$, (c) NFO (d) NFOC-20.

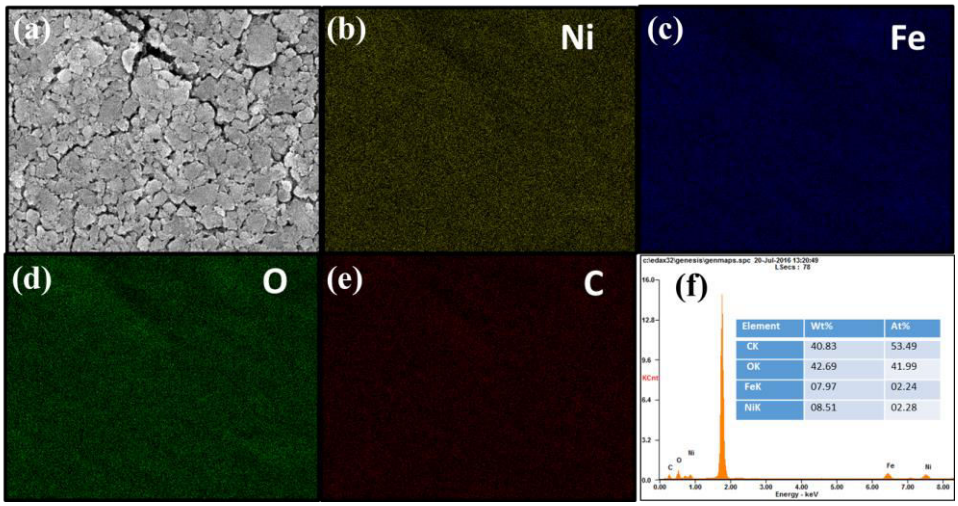

Figure 3.5: (a-e) SEM elemental mapping of Ni, Fe, O and C in NFOC-20 and (F) EDX spectrum of NFOC-20.

3.3.4 Transmission electron microscopy

TEM analysis was carried out to investigate the structural morphology of the as-prepared materials. Figure 3.6(a-c) shows the TEM images of $Ni(OH)_2$, Fe_2O_3 and CNO. TEM image of $Ni(OH)_2$ have nanosheets like morphology in which irregular interspaces of

nanoflowers as shown in figure 3.6a. Figure 3.6 (b and c) confirms the cubic structure of Fe_2O_3 nanoparticles and spheroidal structure of carbon nanoonions, respectively. The decoration of Fe_2O_3 nanoparticles on the $Ni(OH)_2$ nanosheets is confirmed by TEM imaging and the corresponding TEM images of NFO and NFOC-20 are shown in figure 3.6d and 3.6e, respectively. From these pictures, it is observed that Fe_2O_3 nanoparticles are decorated on $Ni(OH)_2$ nanosheets and these sheets are wrapped on and in between CNOs. The HRTEM images in the inset of figure 3.6e exhibit the lattice fringes of NFOC-20. The d-spacing value of 0.37 nm and 0.25 nm corresponds to the (012) plane of Fe_2O_3 and (111) plane of $Ni(OH)_2$.

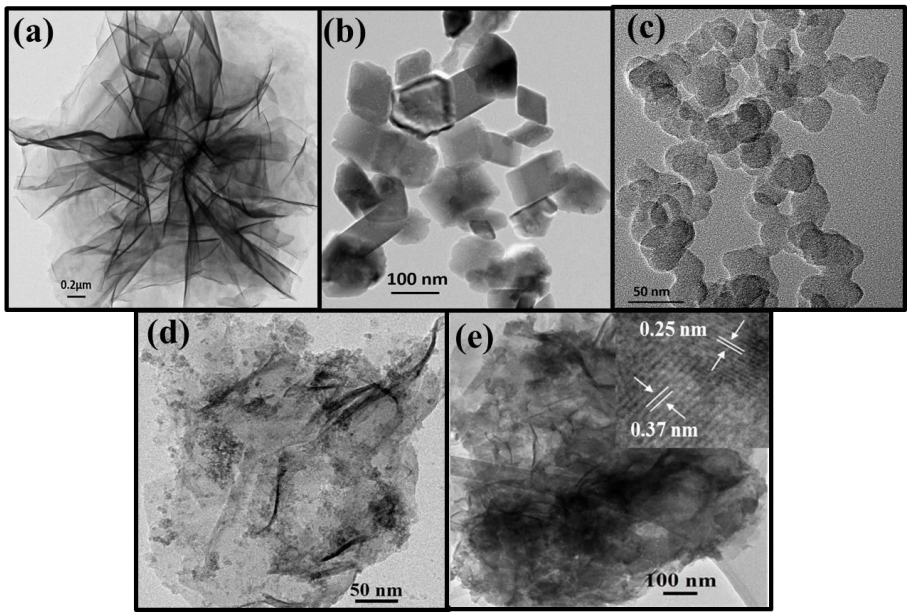

Figure 3.6: TEM images of (a) $Ni(OH)_2$, (b) Fe_2O_3, (c) CNO (d) NFO and (e) NFOC-20 (inset of figure e showing lattice fringes with d-spacing values).

3.3.5 Thermogravimetric analysis

Thermal stability of all the above samples were analysed by thermogravimetric analysis (TGA) under air atmosphere at a scan rate of 10 °C min^{-1} up to 1000 °C (figure 3.7). As we can see that the pure α-Fe_2O_3 sample remains stable up to 96.5 % over the whole temperature range while $Ni(OH)_2$ begins to decompose at 230 °C and complete weight loss occurred at 295 °C with 33.6 % weight loss associated with the conversion of $Ni(OH)_2$ into NiO. The TGA curve of the binary composite shows the combined effect of Fe_2O_3 and $Ni(OH)_2$ with 28.5 % of weight loss, whereas in case of ternary composite 50 % weight loss at 500 °C confirm the presence of 50 % of CNOs by weight in the ternary composite of NFOC.

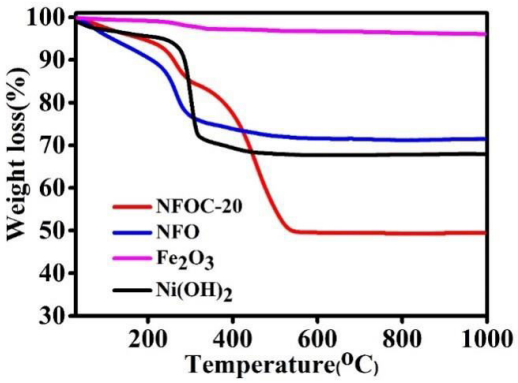

Figure 3.7: Thermo-gravimetric analysis of $Ni(OH)_2$, Fe_2O_3, NFO and NFOC-20.

3.3.6 Cyclic voltammetry

To evaluate the electrochemical behavior of these materials as an anode for LIB, standard coin-type cells were assembled with as-synthesized materials as a working electrode and lithium foil as a reference and counter electrode. The electrochemical reaction of the ternary composite as an anode material for LIB can be explained by the following reactions:

$$Ni(OH)_2 + 2Li^+ + 2\,e^- \leftrightarrow Ni + LiOH \ldots\ldots\ldots\ldots (2)$$

$$Fe_2O_3 + 6Li^+ + 6e^- \leftrightarrow 2Fe + 2Li_2O \ldots\ldots\ldots\ldots (3)$$

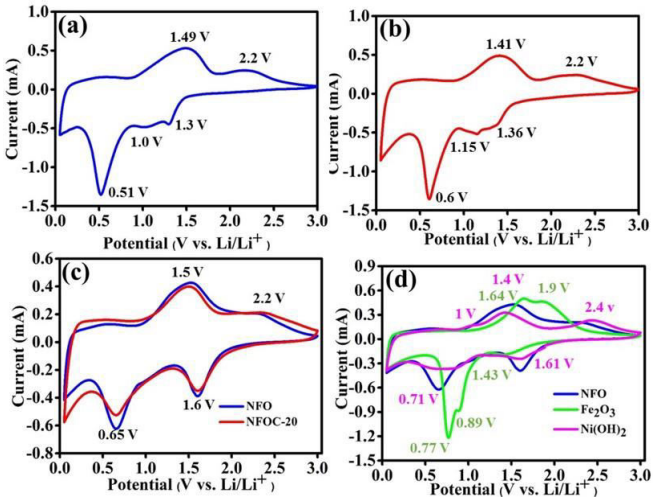

Figure 3.8: Cyclic voltammograms of (a) first cycle of NFO (b) first cycle of NFOC-20 (c) second cycle of NFO and NFOC-20 (d) second cycles of $Ni(OH)_2$, Fe_2O_3, and NFO electrodes in the voltage range of 0.05-3.0 V.

Cyclic voltammetry (CV) was employed to investigate the electrochemical activity of these electrodes in the potential window of 0.05 V to 3.0 V vs. Li/Li^+ at 0.25 mVs^{-1} of scan rate. From figure 3.8a we can see that in the first cycle of NFO, three peaks appear at 1.3 V, 1.0 V, and 0.5 V in the cathodic region ascribed to the initial reduction of Ni^{2+} and Fe^{3+}. The solid electrolyte interface (SEI) layer formed on the surface of the electrode material and in the anodic region two peaks appear at 1.49 V and 2.2 V which corresponds to the oxidation

of Fe to Fe^{2+}/ Fe^{3+} and Ni to Ni^{2+}. Whereas in the first cycle of NFOC-20 (figure 3.8b) a slight shift in the corresponding reduction and oxidation peaks is observed due to the structural modification of the electrode material by the addition of the CNOs. In the second cycle of both the electrodes, i.e., NFO and NFOC-20 (figure 3.8c), anodic and cathodic peaks are broadened and not as distinguishable as those of individual $Ni(OH)_2$ and the Fe_2O_3 component shown in figure 3.8d. This might be because of their different composition and addition of the CNOs. Figure 3.8d shows second cycle of CV curve of $Ni(OH)_2$ nanosheets, Fe_2O_3 nanoparticles and NFO.

Two cathodic peaks at 0.71 V & 1.61 V and three anodic peaks at 1 V, 1.40 V & 2.4 V are observed in the CV of $Ni(OH)_2$ nanosheets which corresponds to the reduction of Ni^{2+} to Ni and decomposition of LiOH at the electrode-electrolyte interface, respectively and vice-versa in case of oxidation.[11] In Fe_2O_3, two cathodic peaks at 0.89 V & 0.77 V and two anodic peaks at 1.64 V and 1.9 V are observed which corresponds to the reduction of Fe^{3+} to Fe^{2+} and Fe^{2+} to Fe and vice-versa.[25, 26] From the CV analysis of these samples it can be reiterated that the reduction and oxidation processes in the $Ni(OH)_2$ and Fe_2O_3 components of hybrid electrodes happens sequentially (with their maximal electrochemical redox activity at different potentials), which is accompanied by the sequential volume expansion and contraction in $Ni(OH)_2$ and Fe_2O_3 components of the electrode. As a result, the development of stress in the electrode is subdued, and the structural integrity of the hybrid electrode is retained.

3.3.7 Charge-discharge measurements

The Galvanostatic charge-discharge studies are performed to estimate the Lithium-ion storage properties of all the electrode materials at an applied current density of 0.05 Ag^{-1} in the voltage range of 0.01-3 V vs. Li/Li^+ and the corresponding charge-discharge profiles are shown in figure 3.9. From the charge-discharge profiles, it is observed that all the electrode materials ($Ni(OH)_2$, Fe_2O_3, NFO, and NFOC-20) have shown very high irreversible discharge capacity. The discharge capacities of $Ni(OH)_2$, Fe_2O_3, NFO and NFOC-20 in the 2^{nd} cycle are found to be 1139, 1029, 1485 and 928 $mAhg^{-1}$, respectively at an applied current density of 50 mAg^{-1}. The discharge capacity of $Ni(OH)_2$ nanosheets electrode has decreased to 1044 $mAhg^{-1}$ in the sixth cycle while maintaining 91 % capacity retention compared to the second discharge capacity. Similarly, 88% of capacity retention was observed in the Fe_2O_3 electrode. In case of binary composite (NFO), the second discharge capacity was obtained to be 1485 $mAhg^{-1}$, higher than the $Ni(OH)_2$ and Fe_2O_3 electrodes; however, it decreases rapidly by the sixth cycle. On addition of CNOs, the discharge capacity of 928 $mAhg^{-1}$ is observed for

NFOC-20 electrode. Comparatively less capacity for this ternary composite was expected due to the addition of 50% of carbon material (CNOs) in the composite, which is having low theoretical specific capacity than the metal oxide or hydroxide. But after the addition of CNOs, the loss of specific capacity over few cycles is also lesser than other electrodes, confirming the enhancement in the stability of the electrode.

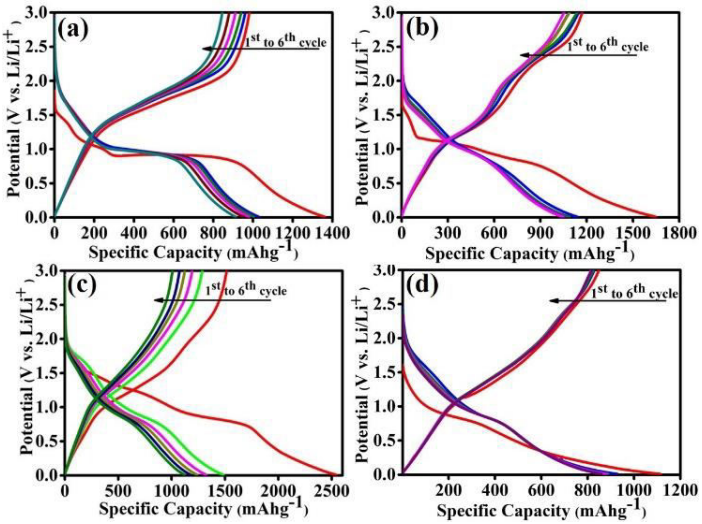

Figure 3.9: Charge/discharge profiles of (a) Fe_2O_3, (b) $Ni(OH)_2$ (c) NFO and (d) NFOC-20 electrodes up to 6 cycles at 50 mAg^{-1} current density.

3.3.8 Rate Performance

The rate capability is also an essential parameter for LIBs, mainly because of its significance in evaluating power capability. Figure 3.10 (a and b) demonstrates the rate capability performance of all the samples at different applied current densities from 0.05 to 1 Ag^{-1}. It can be seen in figure 3.10a that with an increase in the applied current density there is a rapid decrease in the specific capacity of all non-CNO electrodes. Whereas on the addition of CNOs, the rate capability also enhances and delivers average reversible discharge capacities of 1112, 831, 815, 753, and 673 $mAhg^{-1}$ at the current densities of 0.05, 0.10, 0.25, 0.50, and 1.00 Ag^{-1} respectively for the NFOC-20. As mentioned earlier, for comparison various weight % of CNOs were used to make a ternary composite. The rate capabilities of these ternary composite electrodes are shown in figure 3.10b along with the data for NFO as well. NFOC-20 retained 60.5 % specific discharge capacity even when applied current density was increased to 1.0 Ag^{-1} from 0.05 Ag^{-1}. As the current density reverted to 0.1 Ag^{-1}, the reversible capacity of the NFOC-20 electrode showed the specific capacity of 890 $mAhg^{-1}$ after 36 cycles. Given that the initial reversible specific capacity of NFOC-20 at 0.1 Ag^{-1} current density was 811 $mAhg^{-1}$ these results exemplify more than 100% capacity recovery for NFOC-20. In figure 3.10 (a and b) it is seen that $Ni(OH)_2$, Fe_2O_3, NFO and NFOC-10

electrodes experience significant capacity fading and capacity recovery after 36 cycles are unsatisfactory. NFOC-30 ternary composite showed enhanced rate capability but with somewhat less specific capacity value because of an excess of carbon content. Therefore, it can be concluded that improved electrochemical performance of the ternary composite NFOC-20 is because of the addition of an optimum quantity of CNOs, which increases the electronic conductivity and provides mechanical integrity to the electrode.

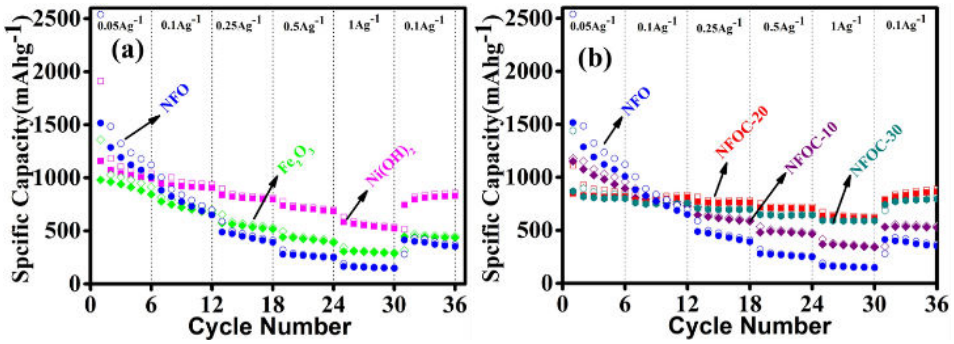

Figure 3.10: Rate capability of (a) Fe_2O_3, $Ni(OH)_2$, NFO and NFOC-20 electrodes (b) NFO, NFOC-10, NFOC-20 and NFOC-30 electrodes at various current densities.

3.3.9 Electrochemical impedance spectroscopy

To understand the role of CNOs on Li-ion diffusion into the electrode, we have performed electrochemical impedance spectroscopic studies and the corresponding Nyquist plots are shown in the figure 3.11. The Nyquist plots were measured at an open circuit potential condition in the frequency range of from 100 KHz to 50 mHz at 10 mV after running the cyclic voltammograms. The Nyquist plots of electrodes for $Ni(OH)_2$, Fe_2O_3, NFO and NFOC-20 consists of semicircle at high-to-medium frequency region and a sloping line at the low-frequency region. This semicircle is attributed to the charge transfer resistance (R_{ct}) between the electrolyte and the electrode. The slope line might be related to the Warburg impedance (Z_w) induced by lithium ion diffusion in the electrodes. Based on the circuit fitting model, α-Fe_2O_3, $Ni(OH)_2$ and NFO electrodes have R_{ct} value of 29.42, 35.70, 18.32 Ω, respectively as shown in figure 3.11. Impedance measurements indicate that upon mixing both the $Ni(OH)_2$ and Fe_2O_3 in a composite, the charge transfer resistance decreased due to the synergistic effect of both components enhancing the conductivity of the electrode. Further, the addition of CNO into this composite makes it more conducting and decreases the charge transfer resistance to 13.23 Ω, implying that the addition of CNOs into the hybrid material significantly promote the charge transfer at the electrode/electrolyte interface, and thus benefit the electrochemical performance.

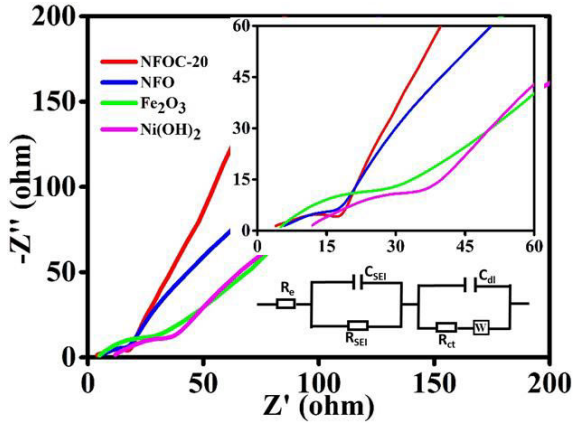

Figure 3.11: Nyquist plots of the AC impedance spectra for the electrodes based on Fe_2O_3, $Ni(OH)_2$ and NFO, NFOC-20

3.3.10 Cycling stability

The stability performance of NFOC-20 was evaluated by charge-discharge cycling at an applied current density of 1.0 Ag^{-1} for 1000 cycles and corresponding plot is shown in the figure 3.12. It is interesting to note that the discharge capacity decreases rapidly up to 70 cycles. After that, the specific capacity of the ternary composite electrode material increases gradually from 350 $mAhg^{-1}$ to 593 $mAhg^{-1}$ up to 400 cycles with a coulombic efficiency of more than 99%. From the 400th cycle the specific capacity is retained at 590 $mAhg^{-1}$ till 1000 cycles. The increasing trend in discharge capacity is probably due to the reversible growth of a polymeric gel-like film resulting from the kinetically activated electrolyte degradation. as Also, the presence of CNOs network enhances the electrochemical activation process and also prevents the materials from pulverization and alleviate the volume changes, consequently offering long cycle life of the ternary hybrid material.[27-29]

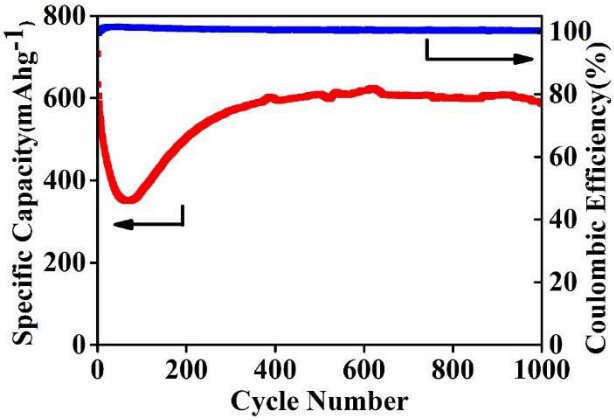

Figure 3.12: Cycling stability of NFOC-20 at 1 Ag-^{1}

3.3.11 Post cycling study

The TEM image of the NFOC-20 after 70, 400 and 1000 cycles at 1 Ag^{-1} have been shown in figure 3.13 (a-c). Figure 3.13c confirms that the morphology of the electrode

material is sustained significantly even after 1000 cycles of charge and discharge at high current density. Figure 3.13d shows the Nyquist plots for NFOC-20 electrode in a fresh cell then after 70 and 400 cycles of charge-discharge at 1 Ag^{-1} of current density. It can be seen in the impedance spectrum taken after 70 cycles that the charge transfer resistance and Warburg impedance increased, probably due to some structural changes for few initial cycles. In an impedance spectrum taken after 400 cycles of charge and discharge, two prominent semicircles appeared at high-frequency region and comparatively more vertical slopping line at the low-frequency region. In general, the first semicircle at high-frequency region corresponds to the SEI layer resistance.[30] The second semicircle observed in the impedance spectra after cycling is related to the charge transfer resistance. It is noted that after charging and discharging for 400 cycles the Warburg impedance decreases as well as charge transfer resistance of the cell is also reduced; most probably due to formation of SEI layer with optimum thickness on the electrode material and penetration of electrolyte in to the electrode which improves electronic/ionic transport and leads to enhance specific capacity of the electrode.[30] These features observed in impedance spectra taken at different levels of cycling corroborate with cycle life study as in figure 3.13d where the capacity initially decreased for few cycles (~ 70 cycles) and then increased up to ~ 400 cycles to finally be stable for more cycling.

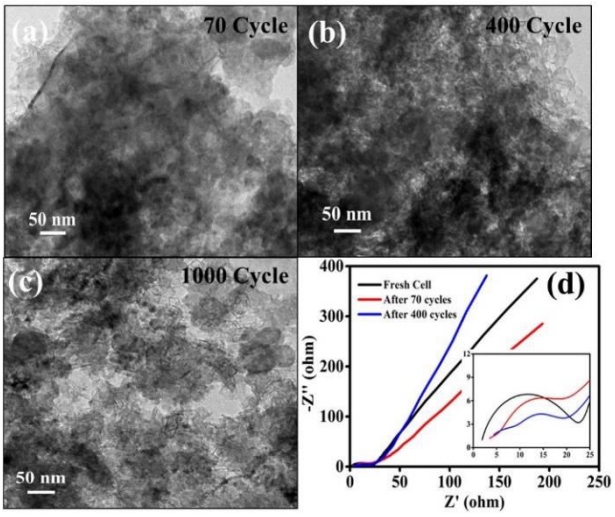

Figure 3.13: (a) TEM image of NFOC-20 at 1Ag^{-1}after 70 cycles (b) 400 Cycles (c) 1000 cycles (d) Nyquist plots of AC impedance spectra NFOC-20 electrode at different cycles of Charge-discharge.

3.4 Conclusions

In summary, we have successfully developed the novel ternary hybrid electrode material of NFOC with different morphological structures by simple two-step solution phase method. In this composite, $Ni(OH)_2$ nanosheets are decorated with Fe_2O_3 nanoparticles and

further these sheets are wrapped on CNOs as observed in the TEM images. Electrochemical measurements suggest that it has excellent rate capabilities, long cycle life with high reversible specific discharge capacity. NFOC electrode material delivers 1112 $mAhg^{-1}$ in 1st discharge cycle at 50 mAg^{-1} of current density and retains its specific capacity up to 60.5% at a higher current density of 1000 $mAhg^{-1}$. Also, at 1 Ag^{-1} of higher current density, as prepared anode material shows 96% capacity retention after 1000 charge-discharge cycles with more than 99% of coulombic efficiency. Hence, the improved electrochemical performance is due to the synergistic effect of the individual components, in which the Fe_2O_3 and $Ni(OH)_2$ increases the reversible discharge capacity and CNOs network maintain the structural integrity of the electrode material on continuous charging and discharging process, with efficient electronic transport and shortened the Li-ion diffusion path.

3.5 References

[1] S. Goriparti, E. Miele, F. De Angelis, E. Di Fabrizio, R. Proietti Zaccaria and C. Capiglia, *J. Power Sources*, 2014, **257**, 421-443.

[2] D. P. Dubal, O. Ayyad, V. Ruiz and P. Gomez-Romero, *Chem. Soc. Rev.*, 2015, **44**, 1777-1790.

[3] J. Jiang, Y. Li, J. Liu and X. Huang, *Nanoscale*, 2011, **3**, 45-58.

[4] D. Larcher, C. Masquelier, D. Bonnin, Y. Chabre, V. Masson, J.-B. Leriche and J.-M. Tarascon, *J. Electrochem. Soc.*, 2003, **150**, A133-A139.

[5] X. Gu, L. Chen, Z. Ju, H. Xu, J. Yang and Y. Qian, *Adv. Funct. Mater.*, 2013, **23**, 4049-4056.

[6] S. Saadat, J. Zhu, D. H. Sim, H. H. Hng, R. Yazami and Q. Yan, *J. Mater. Chem. A*, 2013, **1**, 8672-8678.

[7] H. Wu, M. Xu, Y. Wang and G. Zheng, *Nano Res.*, 2013, **6**, 167-173.

[8] Y.-Y. Hu, Z. Liu, K.-W. Nam, O. J. Borkiewicz, J. Cheng, X. Hua, M. T. Dunstan, X. Yu, K. M. Wiaderek, L.-S. Du, K. W. Chapman, P. J. Chupas, X.-Q. Yang and C. P. Grey, *Nat Mater*, 2013, **12**, 1130-1136.

[9] J. Cabana, L. Monconduit, D. Larcher and M. R. Palacín, *Adv. Mater.*, 2010, **22**, E170-E192.

[10] M. V Reddy, G. V Subba Rao and B. V. R. Chowdari, *Chem. Rev.*, 2013, **113**, 5364-5457.

[11] Y. Zhu and C. Cao, *RSC Adv.*, 2015, **5**, 83757-83763.

[12] S. Cabanas-Polo, Z. Gonzalez, A. J. Sanchez-Herencia, B. Ferrari, A. Caballero, L. Hernán and J. Morales, *J. Eur. Ceram. Soc.*, 2015, **35**, 573-584.

[13] J. Ji, L. L. Zhang, H. Ji, Y. Li, X. Zhao, X. Bai, X. Fan, F. Zhang and R. S. Ruoff, *ACS Nano*, 2013, **7**, 6237-6243.

[14] Y. Tao, C. Jinfei, Y. Tingting and L. Zaijun, *Mater. Res. Bull.*, 2014, **60**, 612-620.

[15] B. Li, H. Cao, J. Shao, H. Zheng, Y. Lu, J. Yin and M. Qu, *Chem. Commun.*, 2011, **47**, 3159-3161.

[16] S. Ni, X. Lv, T. Li, X. Yang and L. Zhang, *J. Mater. Chem. A*, 2013, **1**, 1544-1547.

[17] X. Zhu, Y. Zhong, H. Zhai, Z. Yan and D. Li, *Electrochim. Acta*, 2014, **132**, 364-369.

[18] V. K. A. Muniraj, C. K. Kamaja and M. V Shelke, *ACS Sustain. Chem. Eng.*, 2016, **4**, 2528-2534.

[19] L. Sciortino, F. Giannici, A. Martorana, A. M. Ruggirello, V. T. Liveri, G. Portale, M. P. Casaletto and A. Longo, *J. Phys. Chem. C*, 2011, **115**, 6360-6366.

[20] X. Lu, Y. Zeng, M. Yu, T. Zhai, C. Liang, S. Xie, M.-S. Balogun and Y. Tong, *Adv. Mater.*, 2014, **26**, 3148-3155.

[21] P. Mérel, M. Tabbal, M. Chaker, S. Moisa and J. Margot, *Appl. Surf. Sci.*, 1998, **136**, 105-110.

[22] V.-D. Dao, N. T. Q. Hoa, L. L. Larina, J.-K. Lee and H.-S. Choi, *Nanoscale*, 2013, **5**, 12237-12244.

[23] H.-T. Fang, C.-G. Liu, C. Liu, F. Li, M. Liu and H.-M. Cheng, *Chem. Mater.*, 2004, **16**, 5744-5750.

[24] M. C. Biesinger, B. P. Payne, L. W. M. Lau, A. Gerson and R. S. C. Smart, *Surf. Interface Anal.*, 2009, **41**, 324-332.

[25] N. Yan, X. Zhou, Y. Li, F. Wang, H. Zhong, H. Wang and Q. Chen, *Sci. Rep.*, 2013, **3**, 3392.

[26] C. T. Cherian, J. Sundaramurthy, M. Kalaivani, P. Ragupathy, P. S. Kumar, V. Thavasi, M. V Reddy, C. H. Sow, S. G. Mhaisalkar, S. Ramakrishna and B. V. R. Chowdari, *J. Mater. Chem.*, 2012, **22**, 12198-12204.

[27] X. Wang, Z. Yang, X. Sun, X. Li, D. Wang, P. Wang and D. He, *J. Mater. Chem.*, 2011, **21**, 9988-9990.

[28] X. W. Lou, C. M. Li and L. A. Archer, *Adv. Mater.*, 2009, **21**, 2536-2539.

[29] S. Grugeon, S. Laruelle, R. Herrera-Urbina, L. Dupont, P. Poizot and J.-M. Tarascon, *J. Electrochem. Soc.*, 2001, **148**, A285-A292.

[30] T. Liu, A. Garsuch, F. Chesneau and B. L. Lucht, *J. Power Sources*, 2014, **269**, 920-926.

Chapter 4

Polydopamine Derived N-doped Carbon with $NiO/NiFe_2O_4$ Nanocomposite as an Anode Material for High Performance Li-Ion Battery

Multicomponent metal oxide $NiO/NiFe_2O_4$ composite with N doped Carbon (NDC/NiO/ $NiFe_2O_4$) has been successfully synthesized via hydrothermal method followed by annealing in inert atmosphere which exhibit excellent electrochemical performances for Li-ion battery anode. NiO prevents the aggregation of $NiFe_2O_4$ nanoparticles and increases the conductivity of active material. Polydopamine derived N doped carbon in the composite provides more active sites, increases the conductivity and acts as a buffer to sustain volumetric expansion of the ternary composite during cycling. The resulting ternary composite of NDC/NiO/ $NiFe_2O_4$ delivers a reversible discharge capacity of 786 $mAhg^{-1}$ at 0.1 Ag^{-1} and 463 $mAhg^{-1}$ at a higher current density of 2 Ag^{-1} with excellent rate performance. Additionally, it exhibits stable cycle life over 1000 cycles with 98% capacity retention and more than 99% of coulombic efficiency.

4.1 Introduction

As discussed in 1st and 3rd chapter transition metal oxides (TMOs) like Fe_2O_3, ZnO, NiO, Co_3O_4, etc. are promising as alternative high-capacity conversion anode materials to substitute the commercially used graphite for LIBs with good electrochemical performance. Among several ferrites, $NiFe_2O_4$ exhibit high theoretical capacity (915 $mAhg^{-1}$) via reacting with 8 moles of Li ions and exhibit inverse spinel structure in which octahedral sites occupied by Ni^{2+} and half of the Fe^{3+} cations and tetrahedral sites occupied by the remaining Fe^{3+}. [1] Significantly both Ni and Fe are environment-friendly and abundant in nature.[2] Hence we have explored this Ni and Fe based TMO in this chapter. The major challenge with $NiFe_2O_4$ electrodes is massive phase transformations accompanied by severe volume expansion during long cycling of charge-discharge, which cause disorientation of electrode material. On this account, anode materials suffer from rapid capacity fade because of the loss of electronic contact between the active material and current collector.[1-3] Additionally the low conductivity of $NiFe_2O_4$ anodes leads to poor rate performance.[4] Synthesis of heterostructures with smart design is an evolving strategy to improve the electrochemical performance of $NiFe_2O_4$ anodes. [5, 6] High theoretical capacity of NiO (718 $mAhg^{-1}$) and its environment friendly behaviour makes it more suitable component to synthesize the hybrid nanocomposite of NiO with $NiFe_2O_4$ as a promising anode material for Li ion battery. [7, 8] However, synthesis of an integrated smart architecture of binary composite by using a simple and facile tactic is challenging, where structural features and electrochemical activities of individual components are fully manifested. [9] Moreover, interface/chemical distributions should be homogeneous at the nanoscale level. Though binary composites provide advantage of two electrochemical active components, poor electrical conductivities and large volume expansion during lithiation-delithiation which leads to the rapid capacity fade during cycling is still a challenging task to tackle. [10]

Usually carbon is used in the composite to improve the cycle life and rate performance of metal oxide based electrode materials.[10] Defects in the form of heteroatoms can improve the efficiency of carbon by providing nucleation sites for TMOs.[11, 12] Besides, nitrogen-doping can improve the electronic conductivity and chemical reactivity of the carbon material which is suitable to enhance the electrochemical performance of battery. [13]

We have synthesized a ternary nanocomposite of N doped Carbon (NDC)/NiO/$NiFe_2O_4$ as an anode material for Li ion battery application via hydrothermal method. In this, N doped carbon was prepared by relatively simple and eco-friendly method by using Polydopamine (PDA), as a nitrogen-rich biomimetic polymer.[14] PDA-derived nitrogen-enriched carbon shows

resemblance with the N-doped multi-layered graphene in structure and electrical conductivity which enables it to deliver large specific capacity.[14, 15] In NDC/NiO/$NiFe_2O_4$ composite, NiO/ $NiFe_2O_4$ increases the specific capacity whereas N doped carbon acts as a buffer to sustain the mechanical stress during charge-discharge process, also improves the electronic conductivity, decreases the path length of Li transport and increases the kinetics of lithiation-delithiation. It delivers 778 $mAhg^{-1}$ of specific capacity at 0.1 Ag^{-1} of current density and retains its capacity to 98% over 1000 cycles.

4.2 Experimental section

4.2.1 Synthesis of $NiFe_2O_4$ and NiO/ $NiFe_2O_4$

$NiFe_2O_4$ and NiO/$NiFe_2O_4$ were prepared by using 'nikel(II)nitrate' ($[Ni(NO_3)_2].6H_2O$) and 'iron(III)nitrate nonahydrate' ($[Fe(NO_3)_3].9H_2O$) in 1:2 and 1:1 ratio respectively as precursors in the solution of 20 ml N-N-Dimethylformamide (DMF) and 90 mg Hexamethyltetraamine (HMTA). Above prepared solution was stirred in an oil bath for 5 h at 90 ºC temperature and subsequently transferred to autoclave for hydrothermal synthesis. The hydrothermal reaction was carried out for 5 h at 160 ºC. Further, the solution was filtered and washed several times with DI water and ethanol and dried at 100 ºC. Further above prepared materials were annealed at 500 ºC in inert atmosphere for 3 h.

4.2.2 Synthesis of NDC/NiO/$NiFe_2O_4$ composite

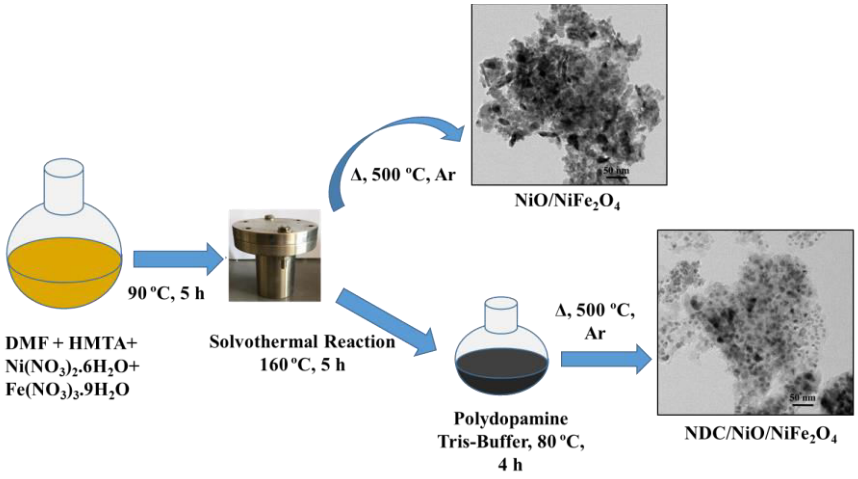

Figure 4.1: Schematic representation of the overall synthetic route towards the formation of NiO/ $NiFe_2O_4$ and NDC/NiO/ $NiFe_2O_4$.

To synthesize the NDC/NiO/$NiFe_2O_4$ ternary nanocomposite, 100 mg of Dopamine with 78 mg of tris buffer were dissolved in 50 ml DI water with 150 mg of NiO/ $NiFe_2O_4$. Here, Tris-buffer was used to maintain a constant pH level. Reaction mixture was stirred at 80 ºC for 4 hours. In order to form the composite of NiO/ $NiFe_2O_4$ with N doped carbon,

above prepared material was annealed at 500 ºC temperature in an inert atmosphere for 3 h. Synthesis routes of NiO/ $NiFe_2O_4$ and NDC/NiO/ $NiFe_2O_4$ are shown schematically in figure 4.1.

4.2.3 Material Characterization

Powder X-ray Diffraction patterns were recorded on a Phillips PAN analytical diffractometer with CuKα radiation (λ = 1.5406 Å). Transmission Electron microscopy was carried out by Tecnai F30 FEG machine operated at an accelerating voltage of 300 kV. Morphology and chemical composition of the ternary hybrid composite were examined by using Quanta 200 3D, FEI scanning electron microscope (SEM). X-ray photoelectron spectroscopic (XPS) measurements were carried out on a VG Micro Tech ESCA 3000 instrument. Thermogravimetric analysis were performed with SDT model Q600 of TA instrument with heating rate at 10degree per minutes in air atmosphere.

4.2.4 Electrochemical Characterization

The electrochemical properties of the electrode materials are examined by two-electrode coin cell (CR2032) configuration. The composite anode was prepared by mixing the active material with the conductive additive (super P) and the binder(polyvinylidene difluoride, PVDF).This mixture was coated on Cu foil, which serves as a current collector, subsequently dried at 90 ºC overnight before making a cell assembly in an Ar-filled glovebox. The coin cells were assembled by using lithium metal foil as a counter electrode, a quartz microfiber paper (Whatman) as a separator and 1 M $LiPF_6$ in ethylene carbonate (EC)-diethyl carbonate (DEC) (1: 1 by volume) as an electrolyte. Cyclic voltammetry (CV) was performed using SP-300 EC Biologic potentiostat at a scan rate of 0.25 mVs^{-1} between 0.01 V and 3.0 V. The galvanostatic discharge-charge cycling of the cells was carried out at different current densities between potentials of 0.01 and 3.0 V by using MTI battery analyzer. The electrochemical impedance spectroscopy (EIS) was used to measure impedance in the frequency range from 100 KHz to 50 mHz with an AC amplitude of 10 mV.

4.3 Results and discussion

4.3.1 Powder X-ray diffraction

Phase purity and lattice structure analysis of $NiFe_2O_4$, NiO/$NiFe_2O_4$ and NDC/NiO/$NiFe_2O_4$ composites were investigated with the help of Powder XRD pattern as shown in figure 4.2. The p-XRD pattern of $NiFe_2O_4$ consists of diffraction peaks at 18.51º, 30.42º, 35.81º, 37.44º, 43.51º, 54.0º, 57.50º and 63.11º which corresponds to (220), (311), (400), (511) and (440) indexing to cubic inverse spinel structure of $NiFe_2O_4$ (JCPDS No. 74-

2081). It should be noted that the (111), (200) and (220) peaks of NiO (JCPDF 47-1049) have nearly the same 2 theta values as those of the (311), (440) and (400) peaks of $NiFe_2O_4$ (JCPDF 10-0325).

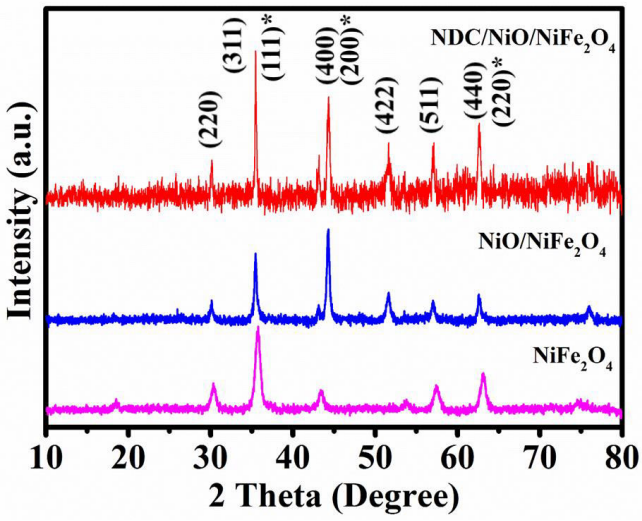

Figure 4.2: p-XRD patterns of $NiFe_2O_4$, $NiO/NiFe_2O_4$ and $NDC/NiO/NiFe_2O_4$.

4.3.2 X-ray photoelectron spectroscopy

The oxidation state of elements and their molecular environment in $NiFe_2O_4$, $NiO/NiFe_2O_4$ and $NDC/NiO/NiFe_2O_4$ were characterized by XPS. Figure 4.3a represents a XPS survey spectra of all the nanomaterials, which indicate the presence of Ni, Fe and O in $NiFe_2O_4$ and $NiO/NiFe_2O_4$ nanocomposites, whereas ternary composites of $NDC/NiO/NiFe_2O_4$ shows additional intense peak of C and N in the survey spectra. Figure 4.3b shows the Fe 2p spectra in $NDC/NiO/NiFe_2O_4$ nanocomposite which consists of the two spin-orbit doublets characteristic of Fe^{2+} and Fe^{3+} with their respective satellite peaks. The Fe 2p spectra of the ternary composite shows two main peaks at binding energies of 711.2 eV for Fe $2p_{3/2}$ and 724.5 eV for Fe $2p_{1/2}$, which are the characteristic peaks of $NiFe_2O_4$.[5, 16] Figure 4.3c shows the Ni 2p spectrum of Ni in $NDC/NiO/NiFe_2O_4$ nanocomposite, which consists of the main peaks observed at binding energies of 855.8 eV for Ni $2p_{3/2}$ and 873.4 eV for Ni $2p_{1/2}$ which are the characteristic peak of Ni^{2+} of NiO and $NiFe_2O_4$. In the Ni 2p spectrum, difference between the binding energy of main peak (855.8 eV, Ni 2p3/2) and its satellite peak at 860.8 eV is 5 eV which is the characteristic nature of Ni^{2+} bond in NiO and $NiFe_2O_4$.[5, 17] Figure 4.3d shows the 5 deconvoluted peaks in high resolution C1s XPS spectra of $NDC/NiO/NiFe_2O_4$ nanocomposites. Peaks appeared at 284.4 eV, 285.5 eV, 286.9 eV and 288.6 eV corresponds to the sp^2 carbon, sp^3 carbon, C-N bond, C=O bond and peak at 290.6

eV shows the presence of Π-Π* bond ‘‘shake-up’’ satellites which are the characteristic peaks of graphitic carbon confirming graphitic nature of NDC.[18,] The high-resolution N1s XPS spectrum of NDC/NiO/$NiFe_2O_4$ nanocomposites is shown in figure 4.3e indicating the 3 deconvoluted peaks which corresponds to different types of binding configurations related to N atoms. Three peaks appeared with binding energies centred at 398.8 eV, 400.0 eV, and 401.0 eV, assigned to pyridine-, pyrrole- and quaternary nitrogen species, respectively.[18, 19]

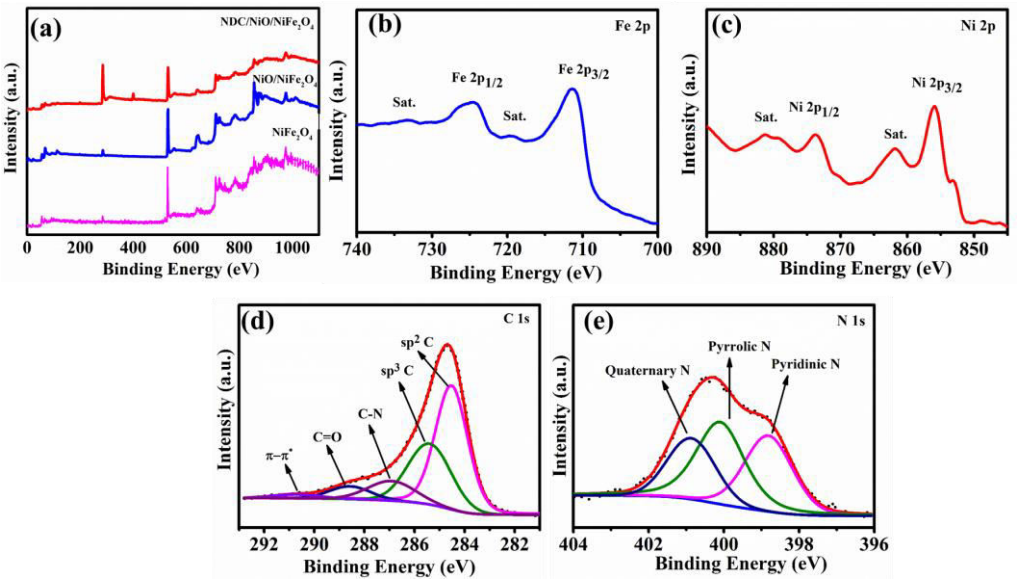

Figure 4.3: (a) XPS survey spectrum of NDC/NiO/$NiFe_2O_4$ (b-e) XPS spectra of Fe 2p, Ni 2p, C 1s, and N 1s, respectively.

4.3.3 Scanning electron microscopy

FESEM imaging was carried out to investigate structural morphology of as prepared sample. Figure 4.4a-c shows FESEM images of the $NiFe_2O_4$, NiO/$NiFe_2O_4$ and NDC/NiO/$NiFe_2O_4$ composites respectively. From figure 4.4a we can see that agglomerated $NiFe_2O_4$ nanoparticles are formed with 10-20 nm size. Figure 4.4b shows the FESEM image of NiO/$NiFe_2O_4$, in which $NiFe_2O_4$ nanoparticles are distributed on the NiO sheet. Figure 4.4c represents the mixed morphology of NDC/NiO/$NiFe_2O_4$ comprised of nanosheets of NiO and N doped carbon along with $NiFe_2O_4$ nanoparticles.

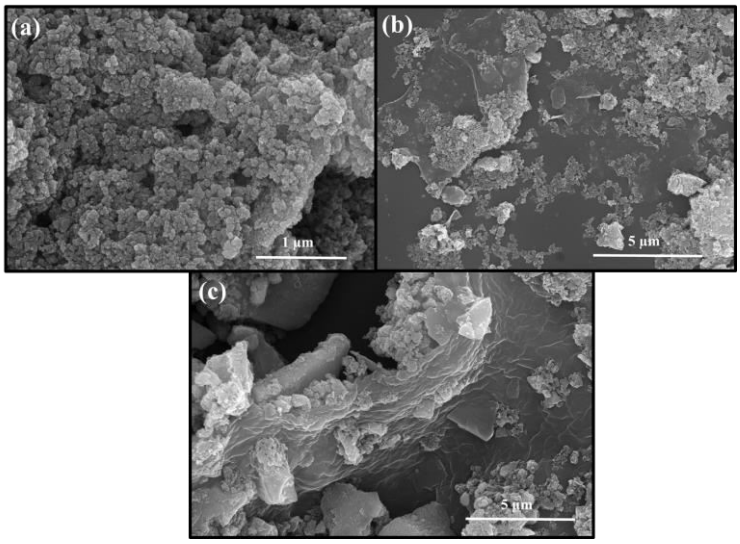

Figure 4.4: FESEM image of (a) $NiFe_2O_4$ (b) $NiO/NiFe_2O_4$ (c) $NDC/NiO/NiFe_2O_4$.

The SEM elemental mapping images revealed the homogeneous distribution of Ni, Fe, C, N and O elements over the selected area of $NDC/NiO/NiFe_2O_4$ composite as shown in figure 4.5.

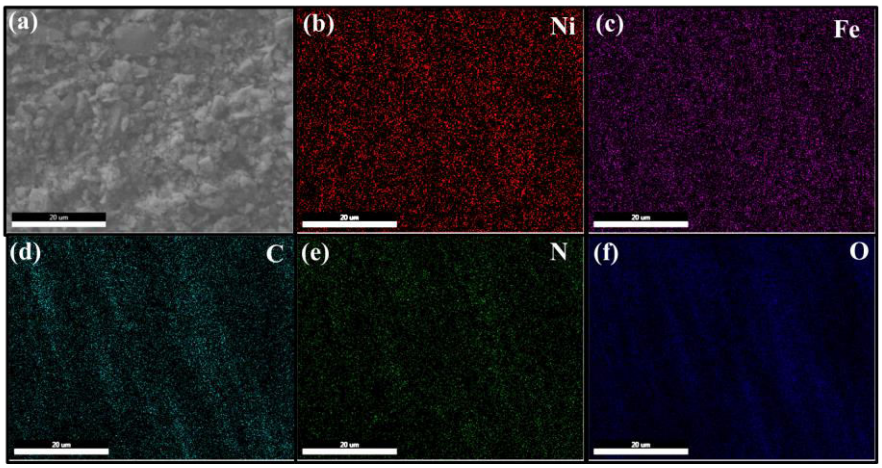

Figure 4.5: Elemental mapping of **(a)** selected area of $NDC/NiO/NiFe_2O_4$ composite (b) Ni (b) Fe (c) C (d) N and (f) O.

4.3.4 Transmission electron microscopy

Figure 4.6 Shows TEM images of $NiFe_2O_4$, $NiO/NiFe_2O_4$ and $NDC/NiO/NiFe_2O_4$ materials to further investigate the structural morphology. Figure 4.6a shows agglomerated nanoparticles of $NiFe_2O_4$ with uniform size distribution of 10-20 nm. Formation of NiO nanosheets along with $NiFe_2O_4$ nanoparticles is evident from figure 4.6b. Low magnification TEM image of $NDC/NiO/NiFe_2O_4$ has been shown in figure 4.6c and high magnification image in 4.6d where it shows mixed morphology of nanosheets of NiO and N doped C with

uniform distribution of $NiFe_2O_4$ nanoparticles. The HRTEM image presented in figure 4.6e exhibit the lattice fringes of $NiFe_2O_4$ and NiO. The d-spacing value of 0.24 nm and 0.29 nm corresponds to the (111) plane of NiO and (220) plane of $NiFe_2O_4$.[20, 21] Figure 4.6f represents the SAED pattern of NDC/NiO/$NiFe_2O_4$ which consist of diffuse rings with bright spots indicate the polycrystalline nature of nanocomposite.

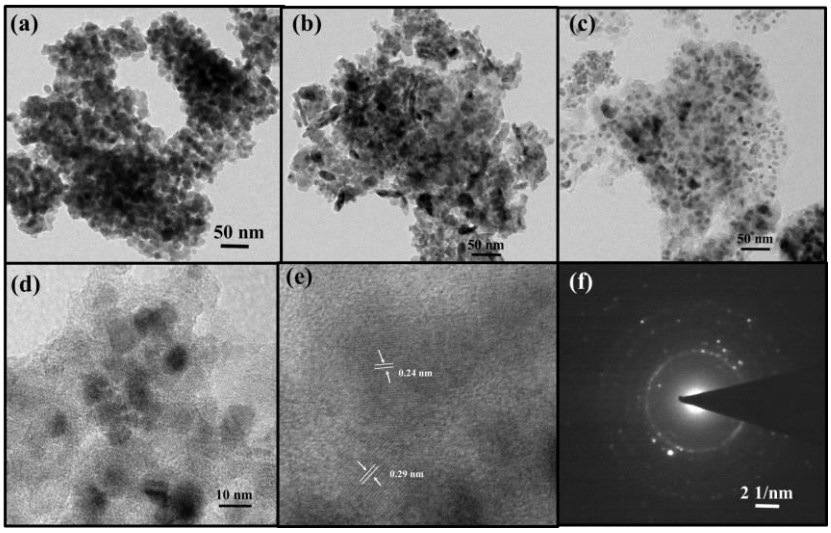

Figure 4.6: TEM image of (a) $NiFe_2O_4$ (b) NiO/$NiFe_2O_4$ (c-e) low to high magnification image of NDC/NiO/$NiFe_2O_4$ (f) SAED pattern of NDC/NiO/$NiFe_2O_4$ composite.

4.3.5 Cyclic voltammetry

To investigate the electrochemical nature of $NiFe_2O_4$, NiO/$NiFe_2O_4$ and NDC/NiO/$NiFe_2O_4$ composites, cyclic voltammetry was performed at a scan rate of 0.25 mVs^{-1} from 0.01 V - 3.00 V. Figure 4.7(a-c) represents CV curves of $NiFe_2O_4$, NiO/$NiFe_2O_4$ and NDC/NiO/$NiFe_2O_4$ composites respectively. In case of $NiFe_2O_4$, in the first cycle one sharp reduction peak is observed at around 0.6 V is due to lithium insertion in to the electrode surface, reduction of Ni^{2+} to Ni and Fe^{3+} to Fe and the irreversible formation of SEI layer on the electrode surface with amorphous Li_2O formation. From second cycle onwards, cathodic peak shifts to 0.78 V with lesser intensity which is due to the presence of some irreversible transformation which gives structure modification in the first cycle. Two anodic peaks are observed at 1.64 V and 1.94 V due to oxidation of metallic Ni to Ni^{2+} and metallic Fe to Fe^{3+}. This multiple electron process can be represented by equations (2) to (5).[5, 22, 23]

$$NiO + 2Li^+ + 2e^- \rightarrow Ni + Li_2O \ldots\ldots\ldots (2)$$

$$NiFe_2O_4 + 8Li^+ + 8e^- \rightarrow Ni + 2Fe + 4Li_2O \ldots\ldots\ldots (3)$$

$$Ni + Li_2O \leftrightarrow NiO + 2Li^+ + 2e^- \ldots\ldots\ldots (4)$$

$$2Fe + 3Li_2O \leftrightarrow Fe_2O_3 + 6Li^+ + 6e^- \ldots\ldots\ldots (5)$$

Figure 4.7b and 4.7c indicate the similar CV curves of $NiO/NiFe_2O_4$ and $NDC/NiO/NiFe_2O_4$ composites to that of $NiFe_2O_4$ with slight shifting in reduction and oxidation peaks. By incorporation of N-doped carbon in $NiFe_2O_4$, the difference between cathodic and anodic potential is reduced indicating that carbon addition in the composites increases the kinetics of lithiation and delithiation and SEI film formation on the electrode surface.[24] From second cycle onwards, overlapping of cathodic and anodic curve in CV indicate the excellent cycling stability of $NDC/NiO/NiFe_2O_4$ composite.

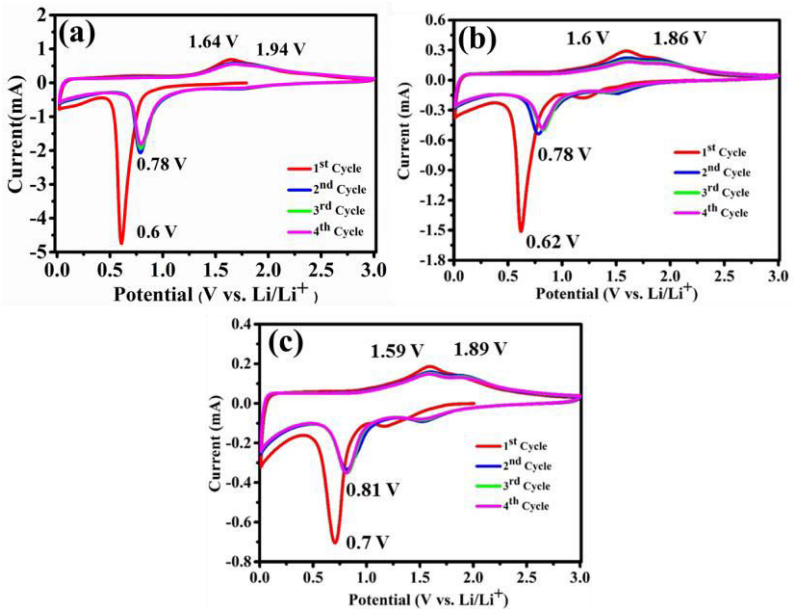

Figure 4.7: Cyclic voltammetry curve of (a) $NiFe_2O_4$ (b) $NiO/NiFe_2O_4$ (c) $NDC/NiO/NiFe_2O_4$ electrodes for 4 cycles at 0.25 mVs^{-1} of scan rate.

4.3.6 Charge-discharge measurements

Figures 4.8 a-c represent galvanostatic charge-discharge curves of initial six cycles for $NiFe_2O_4$, $NiO/NiFe_2O_4$ and $NDC/NiO/NiFe_2O_4$ nanocomposites, respectively at 0.1 Ag^{-1} with reference to Li/Li^+. In The first cycle, discharge capacities of $NiFe_2O_4$, $NiO/NiFe_2O_4$ and $NDC/NiO/NiFe_2O_4$ are noted to be 1211, 1138 and 1166 $mAhg^{-1}$ respectively. The extended potential plateaus of initial discharge were obtained at around 0.65 V for all three electrodes. Similarly, the plateaus obtained in case of initial charging are located near 1.6 V and 1.9 V. This as well as the subsequent data is nearly consistent with corresponding reduction and oxidation peaks obtained in CV. The initial capacity loss is imputed to Solid Electrolyte Interface (SEI) layer formation and side reactions. $NiFe_2O_4$, $NiO/NiFe_2O_4$ and $NDC/NiO/NiFe_2O_4$ deliver second discharge capacity of 908, 774 and 786 $mAhg^{-1}$

respectively and maintain 82%, 87% and 92% capacity retention up to 6th cycles. More capacity retention for ternary composite is due to the more conducting nature of N doped carbon that improves the specific capacity and also act as a buffer for volume expansion during cycling to maintain the structural integrity of electrode material.[25]

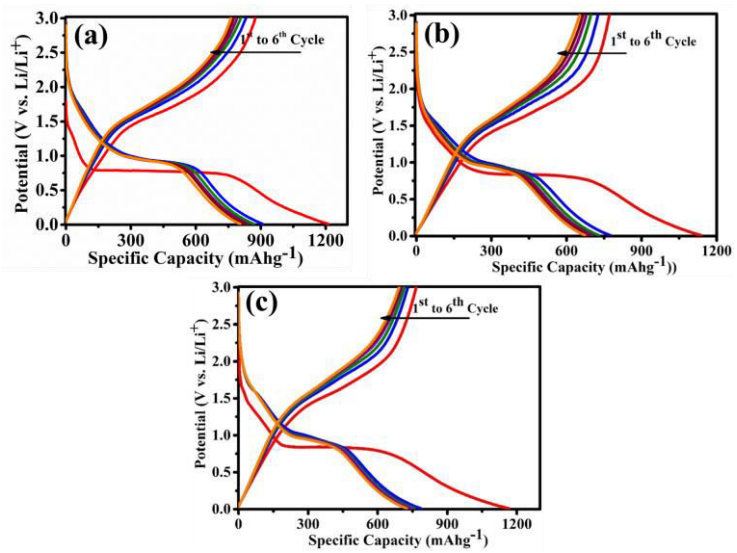

Figure 4.8: Charge/discharge profiles of (a) $NiFe_2O_4$ (b) $NiO/NiFe_2O_4$ (c) $NDC/NiO/NiFe_2O_4$ electrodes for 6 cycles at 100 mAg^{-1} current density.

4.3.7 Rate performance

The rate performance is a crucial parameters to evaluate the electrochemical performance of the electrode materials for the LIBs applications. The rate capability of $NiFe_2O_4$, $NiO/NiFe_2O_4$ and $NDC/NiO/NiFe_2O_4$ were examined at different current densities of 0.1, 0.25, 0.5, 1 and 2 Ag^{-1} as shown in figure 4.9. Ternary composite of $NDC/NiO/NiFe_2O_4$ delivers specific capacity of 786, 701, 619, 545 and 463 $mAhg^{-1}$ at 0.1, 0.25, 0.5, 1 and 2 Ag^{-1} of current density respectively and retains 59% of initial capacity. When the current density reverted to 0.1 Ag^{-1}, specific discharge capacity of 653 $mAhg^{-1}$ could be obtained. Whereas, in case of $NiFe_2O_4$ and $NiO/NiFe_2O_4$ electrodes, the specific capacity of 908 and 774 $mAhg^{-1}$ is obtained at 0.1 Ag^{-1} current density. At higher current density of 2 Ag^{-1} $NiFe_2O_4$ and $NiO/NiFe_2O_4$ electrodes show 226 and 311 $mAhg^{-1}$ of specific capacity with 25% and 40% capacity retention respectively. After returning to 0.1 Ag^{-1} from 2 Ag^{-1} both the electrodes exhibit 393 and 479 $mAhg^{-1}$ of specific capacity respectively which is less in compare to ternary nanocomposite of $NDC/NiO/NiFe_2O_4$. In case of $NiFe_2O_4$, $NiO/NiFe_2O_4$ electrode, $NiO/NiFe_2O_4$ exhibit better rate performance due to addition of NiO sheet which potentially prevents the particle aggregation of $NiFe_2O_4$ nanoparticles during cycling. Among all three electrode material, $NDC/NiO/NiFe_2O_4$ shows

excellent rate performance due to the hetero atom doped conducting carbon matrix which improve the capacity and hinder the material pulverization during cycling at higher current density.

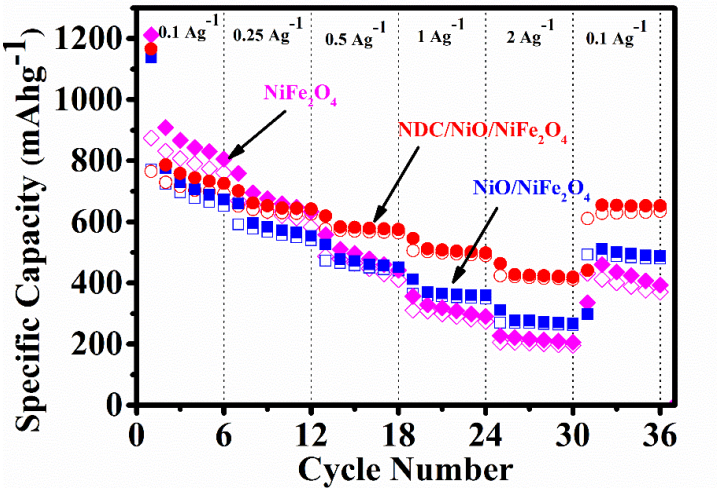

Figure 4.9: Rate Performance of $NiFe_2O_4$, $NiO/NiFe_2O_4$ and $NDC/NiO/NiFe_2O_4$ electrodes from 0.1 Ag^{-1} to 2 Ag^{-1} of current density.

4.3.8 Cycling stability

Figure 4.10 shows the cycling stability of $NDC/NiO/NiFe_2O_4$ ternary nanocomposite for 1000 cycles at a current density of 1 Ag^{-1}. For initial 50 cycles, specific capacity decreases to 350 $mAhg^{-1}$ from 518 $mAhg^{-1}$ and then gradually increases till 650 cycles and become stable up to 1000 cycles. This initial capacity loss occurs due to the formation and conditioning of the electrodes during initial cycles which happens due to the structural rearrangements to form good electrical contacts with the conducting carbon matrix. Thus, while cycling the electrochemical grinding effect promotes to disaggregation of the active material agglomerations and provokes capacity fading. Over 1000 cycles of continuous charge-discharge it deliver specific capacity of 510 $mAhg^{-1}$ with nearly 98% capacity recovery. The increase in capacity after 50 cycles can be attributed to the reversible polymeric/gel film formation on the electrode surface caused by electrolyte degradation during cycling.[26] Additionally it exhibits more than 99% of coulombic efficiency over 1000 cycles of charge-discharge.

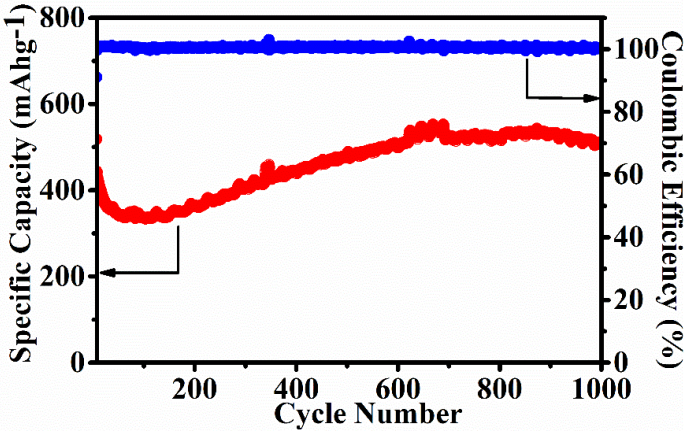

Figure 4.10: Cycling stability of NDC/NiO/$NiFe_2O_4$ electrode at Ag^{-1} of current density for 1000 cycles.

4.3.9 Electrochemical impedance spectroscopy

EIS measurement was carried out in the frequency range of 100 kHz to 0.05 Hz to examine the charge transfer resistance of $NiFe_2O_4$, NiO/$NiFe_2O_4$ and NDC/NiO/$NiFe_2O_4$ electrodes at 10 mV and at room temperature. As shown in figure 4.11, Nyquist plot consists of indented semi-circles in the high to medium frequency region corresponds to charge transfer resistance (R_{ct}) and steep line in the low frequency region that represents Warburg diffusion resistance.[27] Charge transfer resistance of all electrode materials was calculated by circuit fitting model. Among all three electrodes, $NiFe_2O_4$ exhibits very high R_{ct} value (250 Ω), whereas NiO/$NiFe_2O_4$ and NDC/NiO/$NiFe_2O_4$ electrodes have less charge transfer resistance of 118 Ω and 67 Ω respectively. Reduced R_{ct} value for NiO/$NiFe_2O_4$ is due to to the active participation of both the components to increase the conductivity of electrode. Whereas in case of ternary nanocomposite addition of N doped carbon improve the conductivity of electrode significantly which increases the electrochemical performance of the battery by reducing the path of Li ion diffusion process.[28]

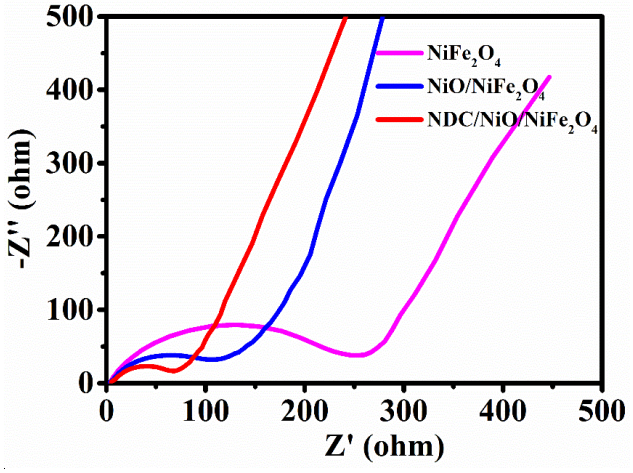

Figure 4.11: Nyquist plot of $NiFe_2O_4$, $NiFe_2O_4$/NiO and NDC/NiO/$NiFe_2O_4$ electrode at 10 mV.

4.3.10 Post cycling study

EIS measurements were carried out to calculate the charge transfer and Warburg resistance of electrode while charge discharge cycling of NDC/NiO/$NiFe_2O_4$ ternary nanocomposite electrode. Figure 4.12a shows the Nyquist plot of NDC/NiO/$NiFe_2O_4$ electrode at different intervals (fresh cell and after 10^{th}, 50^{th}, 100^{th} and 200^{th} cycles of charge-discharge) of cycling at 1 Ag^{-1} of current density. It is clearly observed that after 10^{th} cycle charge transfer resistance and Warburg diffusion resistance of electrode decreases on increasing cycle number. After 50^{th}, 100^{th} and 200^{th} cycles two prominent semicircles observed in which first semicircle in higher frequency region corresponds to SEI layer resistance and another semicircle at mid frequency region corresponds to charge transfer resistance. [29] On increasing cycling number, SEI layer formation with optimum thickness as well as electrolyte penetration on the electrode surface increase the electronic/ionic transport during cycling and reduce the charge transfer and Warburg diffusion resistance of the electrode. This decreased resistance during cycling helps to improve the specific capacity of the electrode. Thus, impedance measurement of the NDC/NiO/$NiFe_2O_4$ electrode validates the cycle life study at different levels of cycling. Cyclic voltammetry was also performed after 1000 cycles at 0.25 mVs^{-1} scan rate for the six cycles in the same cell. As shown in figure 4.12b, it can be seen that one broad reduction peak appeared at around 0.6 V which is due to the reduction of Ni^{2+} to metallic Ni and Fe^{3+} to metallic Fe and in oxidation region broad peak observed at around 1.6 V due to the oxidation of Ni and Fe to Ni^{2+} and Fe^{3+}. Hence appearance of these redox peaks in the CV of NDC/NiO/$NiFe_2O_4$ electrode after 1000 cycles indicate the maintenance of structural integrity of electrode material.

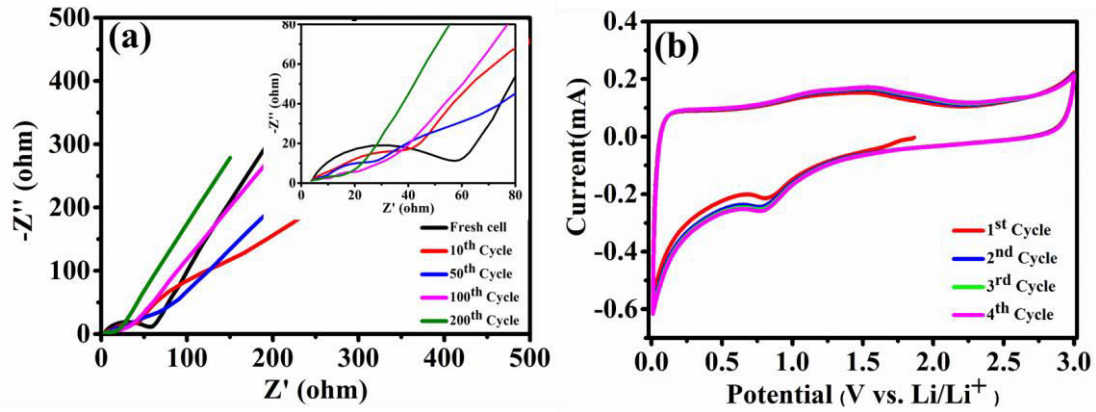

Figure 4.12: (a) Nyquist plots of AC impedance spectra NDC/NiO/$NiFe_2O_4$ electrode at different cycles of Charge-discharge, (b) Cyclic voltammetry curve of NDC/NiO/$NiFe_2O_4$ electrode at 0.25 mVs^{-1} scan rate after 1000 cycles at 1Ag^{-1} of current density.

4.4 Conclusions

A ternary nanocomposite of NDC/NiO/$NiFe_2O_4$ is synthesized as an electrode material with hetero structure morphology by using solvothermal method. In this composite, $NiFe_2O_4$ nanoparticles are decorated with NiO nanosheets and mixed with nanosheets of N doped carbon. Electrochemical study of ternary composite reveals that it has long and quite stable cycle life with excellent rate capabilities as well as high reversible discharge capacity. It delivers a reversible discharge capacity of 786 $mAhg^{-1}$ at 0.1 Ag^{-1} and 463 $mAhg^{-1}$ at a higher current density of 2 Ag^{-1}. Furthermore, it exhibits stable cycle life over 1000 cycles with 98% capacity retention and more than 99% of coulombic efficiency. Sheet like morphology of NiO avoids the aggregation of $NiFe_2O_4$ nanoparticles. Polydopamine derived N doped carbon in the composite provides more active sites to react with Li ions, increases the conductivity and act as a buffer to sustain volumetric expansion of the ternary composite during cycling.

4.5 References

[1] C. Vidal-Abarca, P. Lavela and J. L. Tirado, *J. Phys. Chem. C*, 2010, **114**, 12828-12832.

[2] H. Wang, Y. Liang, M. Gong, Y. Li, W. Chang, T. Mefford, J. Zhou, J. Wang, T. Regier, F. Wei and H. Dai, *Nat. Commun.*, 2012, **3**, 917.

[3] B. Das, M. V Reddy and B. V. R. Chowdari, *J. Alloys Compd.*, 2013, **565**, 90-96.

[4] Q. Q. Xiong, Y. Lu, X. L. Wang, C. D. Gu, Y. Q. Qiao and J. P. Tu, *J. Alloys Compd.*, 2012, **536**, 219-225.

[5] Y. Wang, S. Wu, C. Wang, Y. Wang and X. Han, *Front. Chem.*, 2019, **6**, 654.

[6] X. Zheng, Y. Zhang, H. Liu, D. Fu, J. Chen, J. Wang, C. Zhong, Y. Deng, X. Han and W. Hu, *Small*, 2018, **14**, 1803666.

[7] W. Shi, Y. Zhang, J. Key and P. K. Shen, *J. Power Sources*, 2018, **379**, 362-370.

[8] X. Yin, H. Chen, C. Zhi, W. Sun, L.-P. Lv and Y. Wang, *Small*, 2018, **14**, 1800589.

[9] M. Li, Y.-X. Yin, C. Li, F. Zhang, L.-J. Wan, S. Xu and D. G. Evans, *Chem. Commun.*, 2012, **48**, 410-412.

[10] L. Guo, Y. Ding, C. Qin, W. Li, J. Du, Z. Fu, W. Song and F. Wang, *Electrochim. Acta*, 2016, **187**, 234-242.

[11] X. Wang, X. Li, L. Zhang, Y. Yoon, P. K. Weber, H. Wang, J. Guo and H. Dai, *Science* , 2009, **324**, 768-771.

[12] Z. Wang, X. Xiong, L. Qie and Y. Huang, *Electrochim. Acta*, 2013, **106**, 320-326.

[13] L. Qie, W.-M. Chen, Z.-H. Wang, Q.-G. Shao, X. Li, L.-X. Yuan, X.-L. Hu, W.-X. Zhang and Y.-H. Huang, *Adv. Mater.*, 2012, **24**, 2047-2050.

[14] Y. Liu, X. Yan, Y. Yu and X. Yang, *J. Mater. Chem. A*, 2015, **3**, 20880-20885.

[15] J. Kong, W. A. Yee, L. Yang, Y. Wei, S. L. Phua, H. G. Ong, J. M. Ang, X. Li and X. Lu, *Chem. Commun.*, 2012, **48**, 10316-10318.

[16] X. Gao, J. Wang, D. Zhang, K. Nie, Y. Ma, J. Zhong and X. Sun, *J. Mater. Chem. A*, 2017, **5**, 5007-5012.

[17] R. Jia, J. Chen, J. Zhao, J. Zheng, C. Song, L. Li and Z. Zhu, *J. Mater. Chem.*, 2010, **20**, 10829-10834.

[18] X.-Z. Song, F.-F. Sun, S.-T. Dai, X. Lin, K.-M. Sun and X.-F. Wang, *Inorg. Chem. Front.*, 2018, **5**, 1107-1114.

[19] Z. R. Ismagilov, A. E. Shalagina, O. Y. Podyacheva, A. V Ischenko, L. S. Kibis, A. I. Boronin, Y. A. Chesalov, D. I. Kochubey, A. I. Romanenko, O. B. Anikeeva, T. I. Buryakov and E. N. Tkachev, *Carbon N. Y.*, 2009, **47**, 1922-1929.

[20] K. Nguyen, N. D. Hoa, C. M. Hung, D. T. Thanh Le, N. Van Duy and N. Van Hieu, *RSC Adv.*, 2018, **8**, 19449-19455.

[21] P. Sivakumar, R. Ramesh, A. Ramanand, S. Ponnusamy and C. Muthamizhchelvan, *J. Alloys Compd.*, 2012, **537**, 203-207.

[22] H. Guo, T. Li, W. Chen, L. Liu, J. Qiao and J. Zhang, *Sci. Rep.*, 2015, **5**, 13310.

[23] J. Chen, X. Wu, Q. Tan and Y. Chen, *New J. Chem.*, 2018, **42**, 9901-9910.

[24] F. Hao, Z. Zhang and L. Yin, *ACS Appl. Mater. Interfaces*, 2013, **5**, 8337-8344.

[25] E. K. Heidari, B. Zhang, M. H. Sohi, A. Ataie and J.-K. Kim, *J. Mater. Chem. A*, 2014, **2**, 8314-8322.

[26] J. Mujtaba, H. Sun, G. Huang, K. Molhave, Y. Liu, Y. Zhao, X. Wang, S. Xu and J. Zhu, *Sci. Rep.*, 2016, **6**, 20592.

[27] X. Leng, S. Wei, Z. Jiang, J. Lian, G. Wang and Q. Jiang, *Sci. Rep.*, 2015, **5**, 16629.

[28] L. Guo, Y. Ding, C. Qin, W. Li, J. Du, Z. Fu, W. Song and F. Wang, *Electrochim. Acta*, 2016, **187**, 234-242.

[29] T. Liu, A. Garsuch, F. Chesneau, B. L. Lucht, *J. Power Sources* **2014**, *269*, 920-926.

Chapter 5

Co_3O_4 NPs Decorated on 3-D Architecture of CNH Foam as a Promising Anode Material for Li-ion Battery

Well-designed Co_3O_4 nanoparticles anchored on functionalized carbon nano horn (CNH) foam nanocomposite was prepared via freeze drying process and demonstrated as anode material for lithium-ion battery (LIB) with improved electrochemical properties. The three-dimensional (3D) hierarchical mesoporous hybrid of functionalized carbon nano horn-Co_3O_4 (CCO) shows an improved lithium storage performance and long cycle life due to high surface area, good conductivity, 3D interconnected mesoporous structure, mechanical and chemical stability and shorten the length of Li-ion transport during lithiation-delithiation compared to bare Co_3O_4. The incorporated Co_3O_4 nanoparticles into interconnected CNH foam effectively increase the number of active sites of CCO nanocomposite and increase the reversible specific capacity and Coulombic efficiency. Different compositions of CNH foam with Co_3O_4 nanoparticles were prepared, among which the CCO 1:1 foam displays reversible capacity of 797 $mAhg^{-1}$ and excellent rate performance. It delivers high specific capacity value of around 702 $mAhg^{-1}$ at 5 Ag^{-1} of high current density. Moreover. It exhibit long cycle stability over 500 cycles with 78% capacity retention as well as >99 % Coulombic efficiency. The hierarchical 3D foam of CCO 1:1 nanocomposite with enhanced electrochemical performance can be used as a potential anode material for LIB applications.

5.1 Introduction

Along with Fe and Ni based oxide, Co_3O_4 is also considered to be an excellent anode material for energy storage due to its high specific capacity of 890 $mAhg^{-1}$ (2 times higher than graphite and even higher than most other metal oxides like SnO_2, NiO, TiO_2), low cost, abundance in nature and environment friendly.[1] Nevertheless, lower conductivity, slow diffusion kinetics, large volume change and consequently low rate capability and poor cycle life hinders its practical use. Various strategies were employed to counter these problems including hybridizing Co_3O_4 with carbon nanocomposites and structural modification of Co_3O_4 nanostructures, such as nanoparticles, nanowires, nanorods, spheres, nanosheets and nanotubes etc., to effectively improve the electrochemical rate performance of LIBs. Synthesis of hybrid nanocomposite of Co_3O_4 nanoparticles incorporated in porous conducting matrix is an effective route to improve the battery performance. [2] Despite intensive research efforts, the rate performance of the Co_3O_4 along with high cycling life is still a major challenge.

Carbon nanohorn (CNH), a cone shaped nanostructure of carbon offers good electrical conductivity, large surface area with hierarchical porous structure as well as good mechanical strength.[3] Hence CNH is effectively being used for the synthesis of variety of hybrid nanostructures. Recently CNH, has received growing research attention in various applications such as sensors, absorbent, supercapacitors, catalyst support, drug delivery system, fuel cells, solar cells, Li-ion batteries etc., since CNH have favorable mechanical and surface properties for energy storage. CNH with high surface area can provide mechanical support as well as act as a conductive matrix for nanoparticles to increase battery performance by effectively preventing the particle aggregation and volume expansion, shorten the Li ion transport path length during charge/discharge process.

In this chapter, the synthesis of CCO foam is reported via freeze drying process with homogenous anchoring of Co_3O_4 nanoparticles in 3D interconnected network of CNH matrix. The as-prepared CCO foam represents an interconnected hierarchical nanostructure, in which Co_3O_4 NPs increase the specific capacity and f-CNH provide electronically conductive network. CNH foam also acts as an elastic buffer for the Co_3O_4 nanoparticles to increase the cycling stability and rate performance of electrode material. The CCO 1:1 foam delivers the reversible capacity of 797 $mAhg^{-1}$ at 0.1 Ag^{-1} of current density. It shows excellent rate performance with 702 $mAhg^{-1}$ of specific capacity at 5 Ag^{-1} of high current density with 89% capacity retention. Moreover, it shows 82% capacity retention over 500 cycle at 1 Ag^{-1} current density with >99 % coulombic efficiency.

5.2 Experimental section

5.2.1 Functionalization of CNH

Surface functionalization is generally employed for altering the surface energy of a material to improve its wetting and adhesion properties. Functionalization of CNH was carried out using H_2O_2 to incorporate the oxygen containing functional group such as hydroxyl, carbonyl and carboxylic group.[4]

5.2.2 Synthesis of f-CNH foam

f-CNH foam was prepared by lyophilization technique. In a typical procedure, f-CNH and DI water were taken in the 5:1 w/v ratio and sonicated for 15 min. Then particular amount of resorcinol, glutaraldehyde and a very small amount of sodium tetraborate decahydrate was added to the above dispersion and sonicated for 2 h. The resulted dispersion was frozen in liquid nitrogen followed by lyophilization in a bench-top freeze dryer for 10 h at -80 ^{0}C and 0.02 mbar pressure.

5.2.3 Synthesis of Co_3O_4 NPs

To synthesize Co_3O_4 nanoparticles, 0.29 g of $Co(NO_3)_2.6H_2O$ was dissolved in 40 mL of ethanol by stirring for 30 minutes followed by addition of ammonia solution ($NH_3.H_2O$, 25%). The obtained solution was transferred into a Teflon-lined stainless steel autoclave and heated at 190 ^{O}C for 24 h. Finally, the reaction mixture was filtered and washed with DI water and ethanol followed by overnight drying.

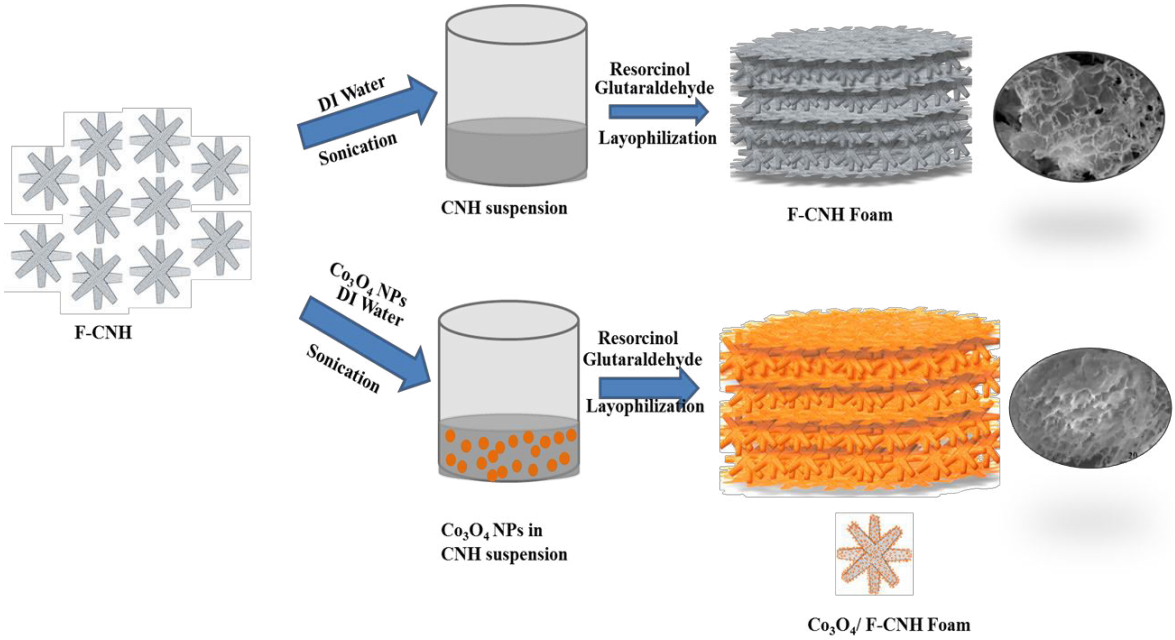

Figure 5.1: Schematic representation of the synthesis of f-CNH foam and Co_3O4 nanoparticles anchored f-CNH foam.

5.2.4 Synthesis of Co_3O_4 NPs decorated f-CNH foam

Nanocomposites of Co_3O_4 NPs decorated f-CNH foam were prepared by dispersion of Co_3O_4 NPs in f-CNH and DI water solution followed by the above mentioned procedure of f-CNH foam synthesis. We have synthesized three different nanocomposites CCO 2:1, CCO 1:1 and CCO 1:2 by varying the mass ratio of f-CNH and Co_3O_4 NPs.

5.2.5 Material Characterization

Powder X-ray Diffraction patterns were recorded on a Phillips PAN analytical diffractometer. Transmission Electron microscopy was carried out by Tecnai F20 FEG machine. Morphology and chemical composition of CCO foam composites was examined by using Quanta 200 3D, FEI scanning electron microscope (SEM). X-ray photoelectron spectroscopic (XPS) measurements were carried out on a VG Micro Tech ESCA 3000 instrument. The nitrogen adsorption desorption isotherm measurements were performed on a Quantachrome surface area analyzer; the specific surface areas and pore size distributions of the samples were obtained by Brunauer-Emmett-Teller (BET) model and Nonlocal density functional theory (NLDFT).

5.2.6 Electrochemical Characterization

The electrochemical properties of CCO foam composites are examined by two-electrode coin cell (2032) configuration. The composite anode was prepared by mixing the active material with the conductive additive (super P) and the binder (polyvinylidenedifluoride, PVDF). This mixture was coated on Cu foil, which serve as a current collector, subsequently dried at 90ºC overnight before making a cell assembly in an Ar-filled glovebox. The coin cells were assembled by using lithium metal foil as a counter electrode, a quartz microfiber paper (Whatmann) as a separator and 1 M $LiPF_6$ in ethylene carbonate (EC)-diethyl carbonate (DEC) (1: 1 by volume) as an electrolyte. Cyclic voltammetry (CV) was performed using SP-300 EC Biologic pontentiostat at a scan rate of 0.25 mV s^{-1} between 0.005 and 3.0 V. The galvanostatic discharge–charge cycling of the cells was carried out at different current densities between potentials of 0.005 and 3.0 V by using MTI battery analyser. The electrochemical impedance spectroscopy (EIS) was used to measure impedance in the frequency range from 100 kHz to 50 mHz with an AC amplitude of 10 mV.

5.3 Results and discussion

5.3.1 Powder X-ray diffraction

The crystalline nature and phase purity of the above prepared materials was confirmed by p-XRD spectra. As shown in figure 5.2, p-XRD pattern of f-CNH foam consist of two broad

peaks at the two-theta values of 24.2 and 43.6 assigned to (002) and (101) planes of graphitized carbon, respectively. All reflections in Co_3O_4, CCO 2:1, CCO 1:1 and CCO 1:2 are in good agreement with spinel structure of Co_3O_4 with a face-centered cubic lattice (JCPDS Card no. 42-1467, cell parameter a = 8.0837 A°). XRD pattern of all four samples consist of diffraction peaks at two theta values of 19.0, 31.29, 36.94, 44.86, 55.7, 59.29 and 65.27 corresponding to (111), (220), (311), (400), (422), (511) and (440) planes, respectively. Diffraction peaks of f-CNH foam disappeared in the composite XRD as the Co_3O_4 NPs cover the f-CNH foam surface. Absence of any other impurity peaks indicates the high phase purity of all prepared materials.

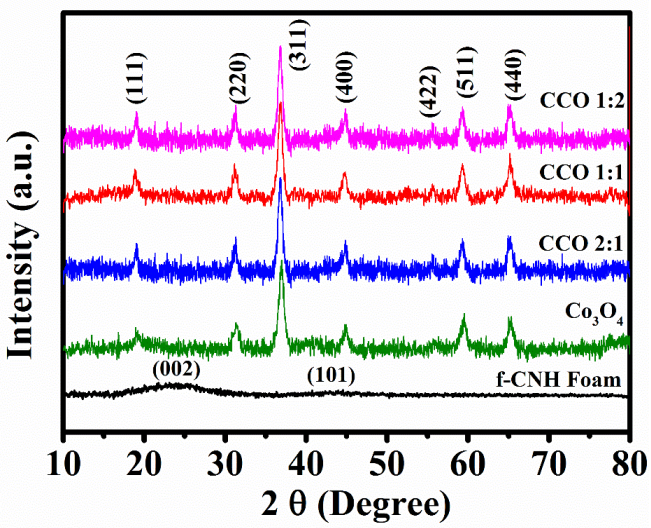

Figure 5.2: X-ray diffraction of f-CNH, f-CNH foam, CO NPs, CCO 2:1, CCO 1:1 and CCO 1:2 composites.

5.3.2 Raman spectroscopy

The phases of the f-CNH, f-CNH foam, CO NPs, CCO 2:1, CCO 1:1 and CCO 1:2 composites were further confirmed by Raman spectroscopy as shown in figure 5.3. The peaks distinguished at around 192, 480, 525, 615 and 682 cm^{-1} correspond to the F_{2g}^1, E_g, F_{2g}^2, F_{2g}^3 and A_{1g} vibrational modes of crystalline Co_3O_4.[5, 6] Additionally, the broad peaks appearing at 1360 cm^{-1} and 1595 cm^{-1} correspond to D and G bands of CNH, respectively. The D band is attributed to the mode of the k-point phonons of A_{1g} symmetry while the G band corresponds to the E_{2g} phonon of C sp^2 atoms. We can also observe that the D band is stronger than the G band, indicating a largely disordered structure of the obtained f-CNH. [7]

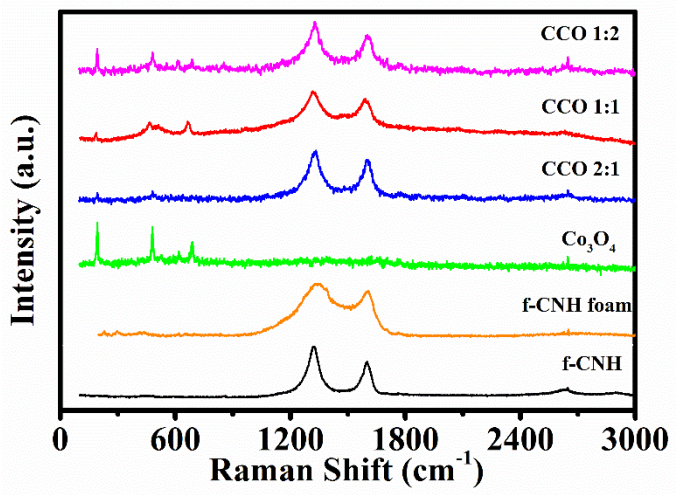

Figure 5.3: Raman spectrum of f-CNH, f-CNH foam, CO NPs, CCO 2:1, CCO 1:1 and CCO 1:2 composites.

5.3.3 X-Ray photoelectron spectroscopy

Chemical composition and oxidation state of cobalt in CCO 1:1 composite were investigated by XPS analysis. Figure 5.4a displays the XPS survey spectra of all three composites (CCO 2:1, CCO 1:1 and CCO 1:2) which displays the presence of Co 2p, C 1s, O 1s and Na 1s peaks. In figure 5.4b and c, deconvoluted spectra of core level peaks are provided to understand the surface composition of the constituting elements. Deconvoluted spectra of Co shows the doublet 2p spectral profile of spinel Co_3O_4 separated by 15.2 eV of binding energy corresponding to $2p_{1/2}$ to $2p_{3/2}$ and separation occurs due to the spin-orbit coupling (figure 5.4b). Both the peaks of Co $2p_{1/2}$ and Co $2p_{3/2}$ contains tetrahedral Co^{2+} and octahedral Co^{3+} ions.[8, 9] The deconvoluted Co 2p peaks at 779.7 eV and 794.9 eV are assigned to Co^{3+} $2p_{3/2}$ and Co^{3+} $2p_{1/2}$, respectively. The deconvoluted peak at 780.9 eV and 796.1 eV corresponds to the other spin-orbit components, Co^{2+} $2p_{3/2}$ and Co^{2+} $2p_{1/2}$, respectively. Moreover, four peaks with lesser intensity are also detected in the high binding energy region of $2p_{3/2}$ and $2p_{l/2}$ transitions corresponding to the respective shake-up satellite peaks of Co_3O_4 indicating the presence of Co^{2+} and Co^{3+} on the surface of the material. Chemical shift of main spin-orbit components may give rise the peaks at 782.2 eV and 797.4 eV which results from the interaction of cationic Co species to surface hydroxyl species. Deconvoluted XPS spectrum of C 1s is shown in figure 5.4c. Four deconvoluted peaks appeared in C 1s spectrum at 284.7, 285.2, 286.5 and 288.2 eV corresponding to the sp^2 hybridized carbon, sp^3 hybridized carbon, C-O and C=O bonds respectively. [10-11]

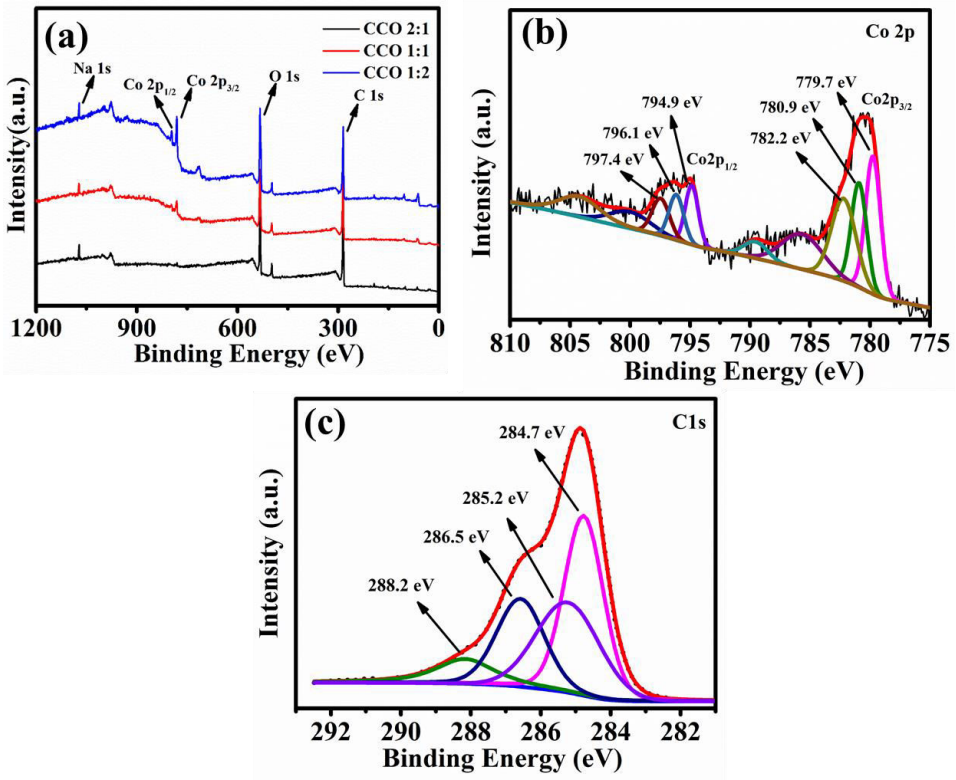

Figure 5.4: (a) XPS survey spectrum of CCO 2:1, CCO 1:1 and CCO 1:2 composite (b) and (c) Deconvoluted spectra for Co and C in CCO 1:1 respectively.

5.3.4 Thermogravimetric analysis

In order to quantify the individual component in the composites, TGA of all four samples was done in air flow with 10 °C min^{-1} rate up to 900 °C as shown in figure 5.5. There are three significant drops in corresponding weight, one is below 100 °C, second is around 300 °C and third is at around 550 °C in composite electrodes. [22] First weight loss is assigned to the dehydration of physisorbed water, whereas second weight loss corresponds to evolution of CO_2 and CO molecules and decomposition of oxygenated functional groups, on the surface of f-CNH foam. At about 550 °C, the weight loss occurred due to the combustion of the carbon skeleton of f-CNH foam matrix. From TGA profile of all 3 composites, it can be seen that the complete removal of carbon content in CCO 2:1 occurred at lower temperature, whereas in case of CCO 1:2 carbon content removed at higher temperature. This phenomenon may be attributed to the catalytic role of Co_3O_4 NPs in the oxidation of carbon materials.[12] After 700 °C, the content of Co_3O_4 in CCO 2:1, CCO 1:1 and CCO 1:2 nanocomposites is about 35%, 45% and 55% respectively.

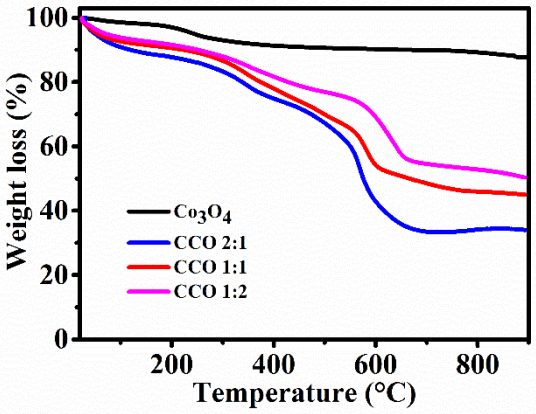

Figure 5.5: Thermogravimetric analysis of Co_3O_4, CCO 2:1, CCO 1:1 and CCO 1:2 composites.

5.3.5 Scanning electron microscopy

Structural morphology of as prepared samples were carried out by FESEM. Figure 5.6a-f shows FESEM images of the Co_3O_4 NPs, f-CNH foam, CCO 1:1, CCO 2:1 and CCO 1:2, respectively. From figure 5.6a we can see that cobalt oxide nanoparticles formed are in the range of 10-15 nm size. Figure 5.6b represents the interconnected network of 3D f-CNH foam. Fig 5.6c-f show Co_3O_4 nanoparticles adsorbed on the formed f-CNH foam. Figure 5.6d shows that the size of interconnected channels of CCO 1:1 are less compared to CCO 2:1 and CCO 1:2, which increases the surface area of the material and provides more active sites to react with Li ions during lithiation and delithiation. In figure 5.6e, it can be seen that the very thick layer of Co_3O_4 NPs deposited on the carbon surface in CCO 1:2 compared to CCO 1:1 and CCO 2:1.

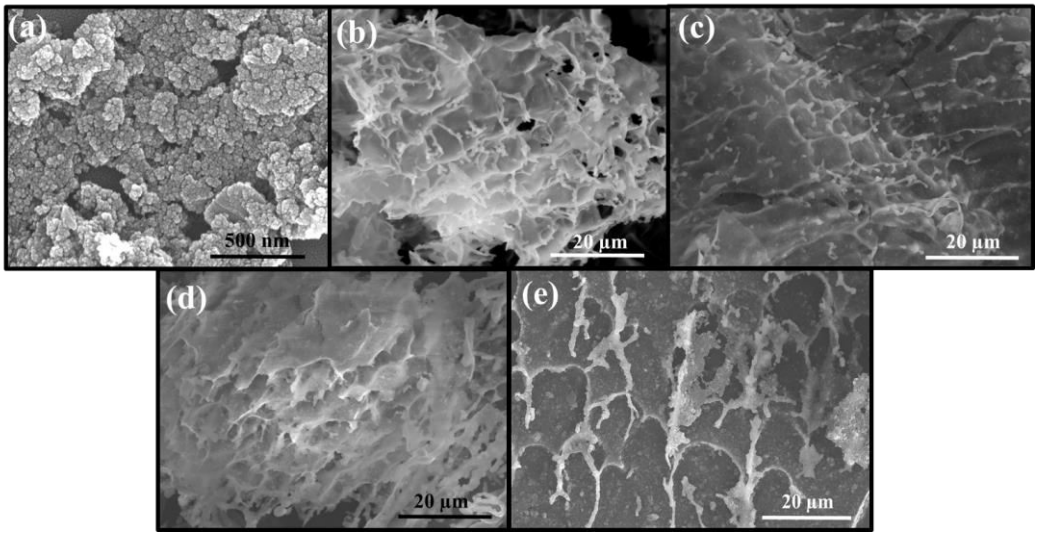

Figure 5.6: FESEM images of (a) Co_3O_4 nanoparticles, (b) f-CNH Foam (c) CCO 2:1, (d) CCO 1:1 and (e) CCO 1:2.

Figure 5.7 (a-e) depicts the SEM elemental mapping, where it can be seen that the distribution of C, Co and O elements are homogenously spread throughout the sample.

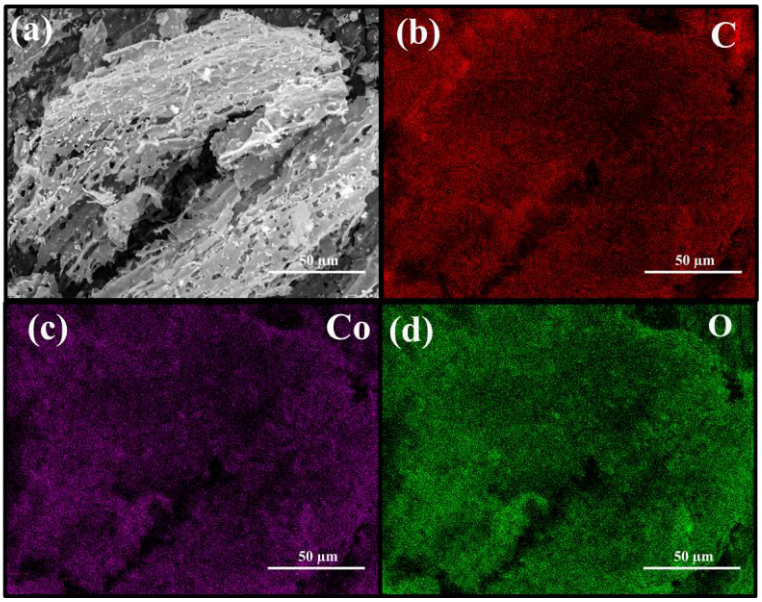

Figure 5.7: Elemental mapping of the 1:1 composite of f-CNH and Co_3O_4 nanoparticles.

5.3.6 Transmission electron microscopy

TEM characterization was carried out for all samples to provide an insight into the inner architecture and the crystallographic nature. Figure 5.8a-c represents the TEM images of f-CNH foam, CCO 2:1, CCO 1:2, respectively and figure 5.8d and 5.8e show the low and high resolution TEM image of CCO 1:1. Among all three composites, in CCO 1:1, Co_3O_4 nanoparticles are distributed homogeneously on the surface of f-CNH sheets whereas in case of CCO 1:2 Co_3O_4 nanoparticles get agglomerated.

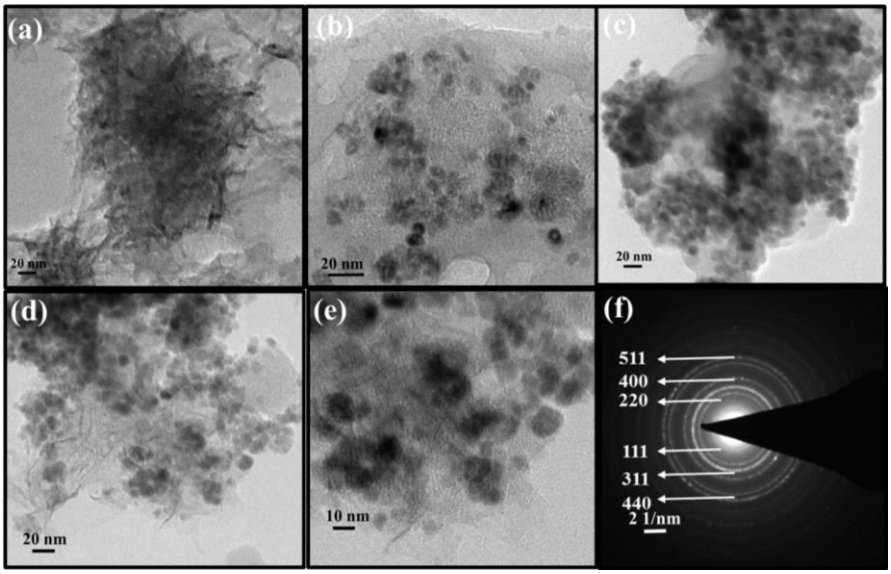

Figure 5.8: Transmission electron microscopy images of (a) f-CNH foam, (b) CCO2:1 composite, (c) CCO1:2. (d) and (e) are TEM images of the CCO1:1. (f) The SAED pattern of the CCO1:1.

Figure 5.8f demonstrates the SAED pattern of CCO 1:1 composite which gives information about polycrystalline nature of the material and diffraction rings corresponds to

(111), (220), (311), (400), (511), and (440) planes of Co_3O_4, which is in well resemblance with p-XRD pattern of the material. [13]

5.3.7 Surface area measurement

The specific surface area of f-CNH foam, Co_3O_4, CCO 1:1 and CCO 1:2 nanocomposites was calculated by using the multi-point BET technique from nitrogen adsorption/desorption isotherm, shown in figure 1c. The isotherms of f-CNH foam, CCO 2:1, CCO 1:1 and CCO 1:2 nanocomposites materials exhibit a BET type IV isotherm with H1 hysteresis which is due to the presence of a mesoporous features in the samples (figure 5.9a). The BET surface area approximated as 935 m^2g^{-1}, 361 m^2g^{-1}, 267 m^2g^{-1} and 100 m^2g^{-1} for f-CNH foam, CCO 2:1, CCO 1:1 and CCO 1:2, respectively. The increasing trend in surface area from CCO 1:2 to CCO 2:1 is due to the more contribution of f-CNH foam in the composite. Pore size distribution (PSD) shown in figure 1d was plotted using Non Local Density Functional Theory (NLDFT) slit-pore model for pores ranging from 1.4-30 nm. PSD results are well in accordance with Nitrogen adsorption isotherm as f-CNH foam exhibit highest pore volume due to a higher presence of micro and meso pores in the range of 1.5 to 15 nm resulting in a high specific surface area with average pore radius of 3.72 nm whereas CCO 2:1, CCO 1:1 and CCO 1:2 has average pore radius of 1.88 nm, 2.06 nm and 3.9 nm as indicated in the figure 5.9b.

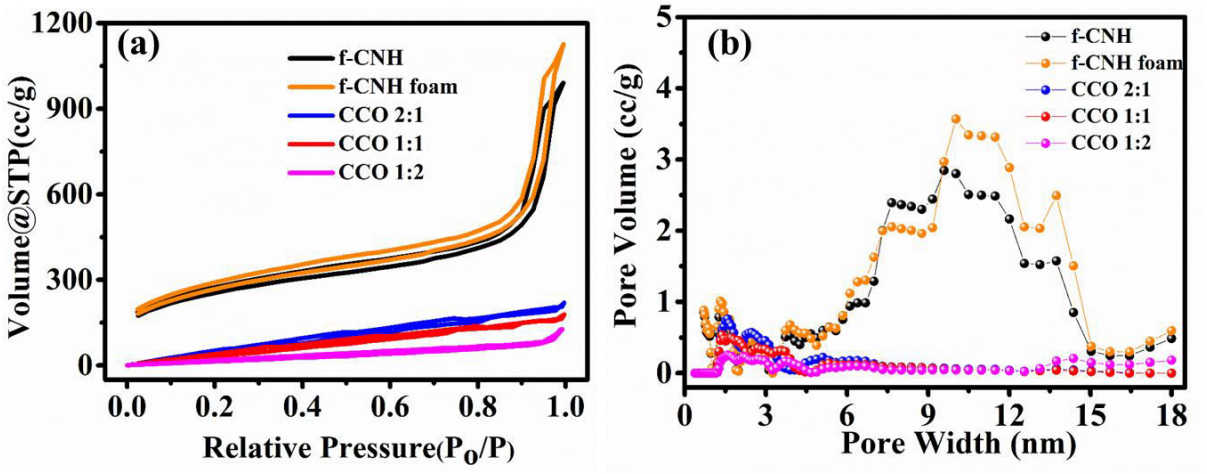

Figure 5.9: (a) N_2 adsorption/desorption isotherms of f-CNH foam, Co_3O_4, CCO 1:1 and CCO 1:2 (b) Pore size distribution curve of f-CNH foam, Co_3O_4, CCO 1:1 and CCO 1:2.

5.3.8 Cyclic voltammetry

Structure and morphology of the electrode material affect the electrochemical performance of the battery. Electrochemical performance of all electrodes was investigated by cyclic voltammetry, galvanostatic charge-discharge and impedance spectroscopy. CV measurements were carried out in the voltage range of 0.01-3.0 V for four cycles at a scan rate

of 0.25 mV s^{-1}. In the first discharge cycle of Co_3O_4 electrodes (Figure 5.10a), sharp cathodic peak appears around 0.78 V due to the electrochemical reduction of Co_3O_4 to metallic cobalt accompanying the formation of Li_2O and the solid electrolyte interphase (SEI) film.[14, 15] From second cycle onwards, cathodic peak splits into two distinguishable peaks appeared at 1.0 V and 1.24 V with lesser intensity which is due to multistep reaction during lithiation and presence of some irreversible transformation which gives structure modification in the first cycle.[14, 15] In the anodic process, broad peaks located at around 1.33 V and 2.09 V can be ascribed to the reversible oxidation reaction from cobalt to Co_3O_4. The corresponding multi-step conversion reaction can be described by equation (1) and (2).

$$Co_3O_4 + 2Li^+ + 2e^- \leftrightarrow Li_2O + 3CoO \ldots (1)$$

$$3CoO + 6Li^+ + 6e^- \leftrightarrow 3Li_2O + 3Co \ldots.. (2)$$

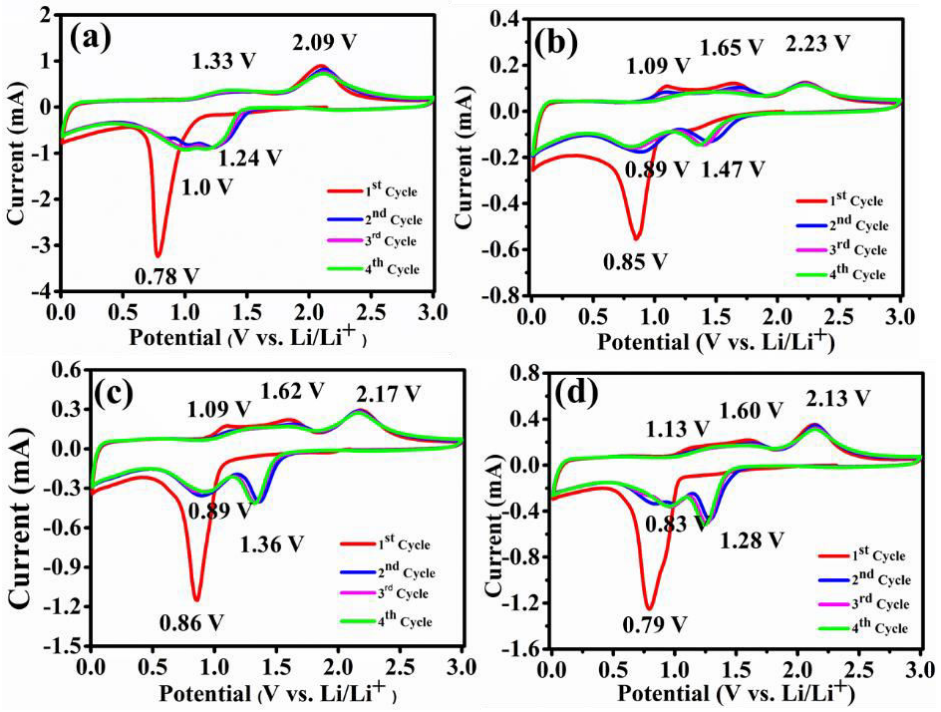

Figure 5.10: Cyclic voltammograms of (a) Co_3O_4 (b) CCO 2:1 (c) CCO 1:1 and (d) CCO 1:2 electrodes in the voltage range of 0.01−3.0 V at 0.25 mVs^{-1}.

Fig 5.10b-d shows the CV curves of CCO 2:1, CCO 1:1 and CCO 1:2, respectively. We can see that oxidative peak positions shifted towards high voltage as the concentration of carbon is increasing. Furthermore, high concentration of Co_3O_4 in the composite increase the intensity of cathodic peak which reveals a fast kinetics process for the phase transformation of Co_3O_4 and SEI film formation on the electrode surface.[2]

5.3.9 Charge-discharge measurements

GCD measurements were carried out to calculate the specific capacity of the composites and their cycling stability. The GCD profiles of Co_3O_4 NPs, CCO2:1, CCO1:1, CCO1:2 are shown in figure 5.11 a-d, respectively. GCD measurements are done at 100 mA g^{-1} of current density in between 0.01 and 3.0 V. A prolonged voltage plateau appeared at around 1.1 V for all the four electrodes due to the lithiation of nanocomposites and the conversion of Co_3O_4 to an intermediate phase of CoO (or $Li_xCo_3O_4$) and then to metallic Co, which indicates typical characteristics of potential trends for the Co_3O_4 electrode materials.[16] The slope occurred in the region of 1.5 to 2.5 V in the charge curves represents reversible oxidation of metallic Co to Co_3O_4. Co_3O_4 delivers second discharge capacity of 1142 $mAhg^{-1}$, whereas CCO 2:1, CCO 1:1 and CCO 1:2 shows 508, 797 and 665 $mAhg^{-1}$. Among all three hybrid composites CCO 1:1 delivers highest reversible capacity because the optimum amount of Co_3O_4 and carbon content in the composite provide high surface area as well as more reactive sites to react with Li which increase the Li storage capacity.

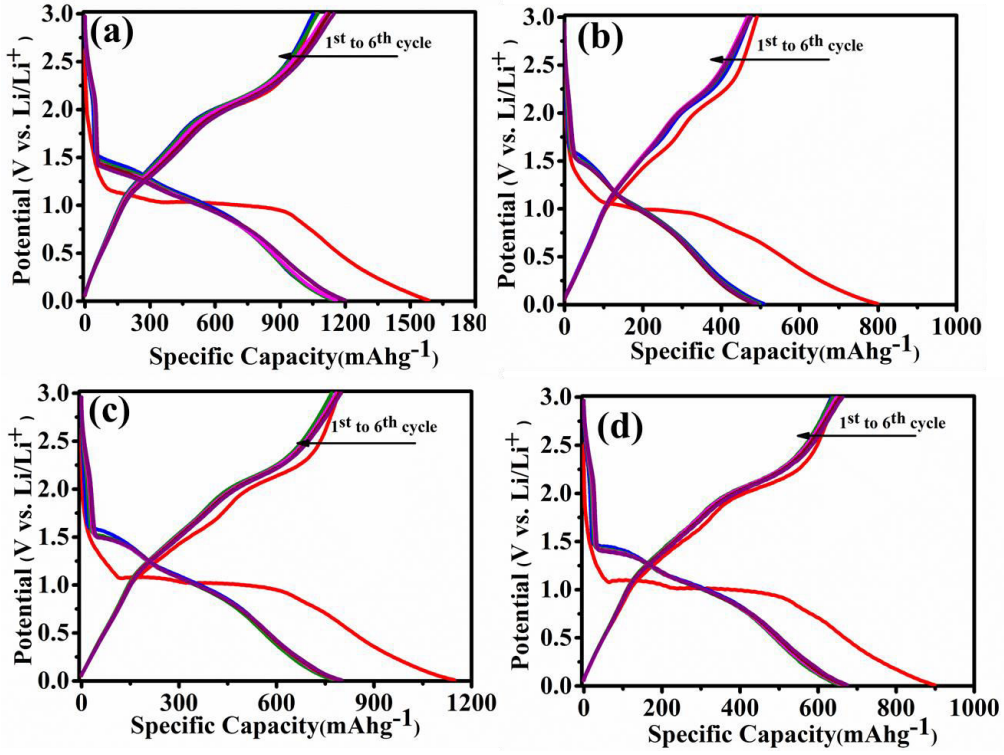

Figure 5.11: Charge/discharge profiles of (a) Co_3O_4 (b) CCO 2:1 (c) CCO 1:1 and (d) CCO 1:2 electrodes for 6 cycles at 100 mAg^{-1} current density.

5.3.10 Rate performance

The rate performance is one of the most important parameter of the materials for the LIBs applications. The rate capability of CCO 2:1, CCO 1:1 and CCO 1:2 were investigated at

different current densities ranging from 0.1, 0.25, 0.5, 1, 2 and 5 Ag^{-1} as shown in figure 5.12. CCO 1:1 electrode delivers specific capacity of 797, 834, 838, 811, 780 and 702 at 0.1, 0.25, 0.5, 1, 2 and 5 Ag^{-1} of current density, respectively. When the current density was reverted to 0.1 Ag^{-1}, it exhibits 963 $mAhg^{-1}$ of specific discharge capacity which is more than initial reversible capacity. In case of CCO 2:1 electrode, initial specific capacity value is less due to more contribution of carbon in the composite during lithiation and delithiation process, whereas in case of CCO 1:2, capacity is less due to large pore volume and less surface area which decrease the active sites reacting with Li ions. Large quantity of Co_3O_4 can get agglomerated and form a thick layer on the carbon network which reduce the diffusion of Li ions during continuous charge-discharge processes.

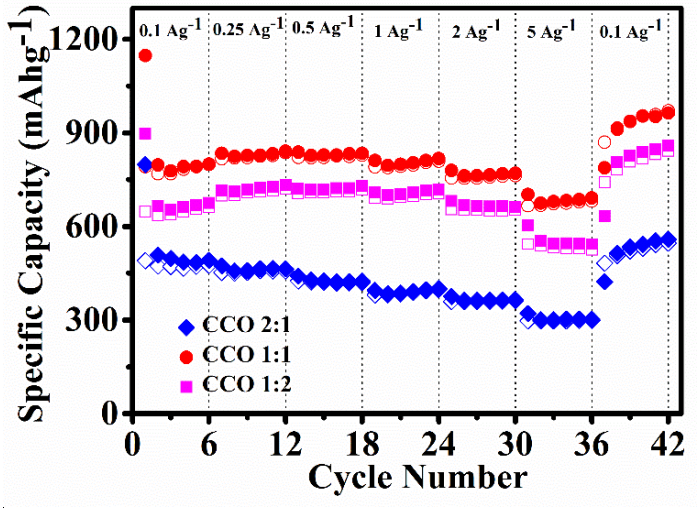

Figure 5.12: Rate Performance of (a) CCO 2:1 (b) CCO 1:1 and (c) CCO 1:2 electrodes from 0.1 Ag^{-1} to 5 Ag^{-1} of current density.

5.3.11 Electrochemical impedance spectroscopy

EIS measurement was used to investigate the charge transfer resistance of Co_3O_4 NPs, CCO 2:1, CCO 1:1, and CCO 1:2 nanocomposites in the frequency range of 100 kHz to 0.05 Hz at 10 mV at room temperature. As shown in figure 5.13, the Nyquist plots of all electrodes consist of a semicircle in high frequency region which corresponds to the charge transfer resistance (R_{ct}) at the electrode/electrolyte interface and a straight line in low frequency region related to diffusion of lithium ion in the bulk materials called Warburg impedance (W). [17, 18] Charge transfer resistance of all electrode materials was calculated by circuit fitting model. Nanocomposites of CNH foam and Co_3O_4 in 1:1 ratio has very less charge transfer resistance (49 Ω) than bare Co_3O_4 (173.8 Ω), CCO 2:1 (75 Ω) and CCO 1:2 (98 Ω) implying that the 3D foam of Co_3O_4-CNH composites exhibit more accessible sites on the surface of active materials and shorten Li-ion diffusion path length which increase the kinetics of charge transfer.[2]

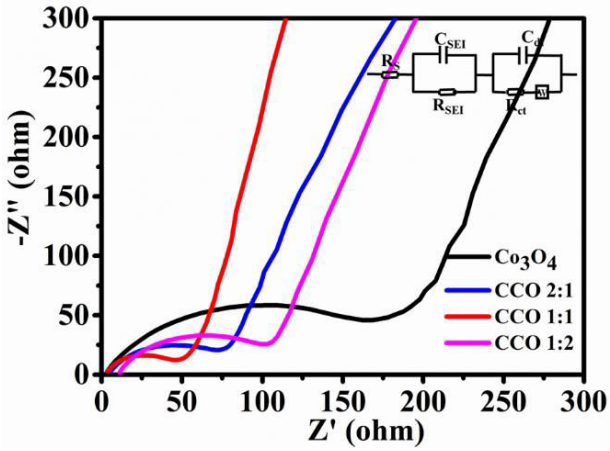

Figure 5.13: Nyquist Plot of (a) Co_3O_4 (b) CCO 2:1 (c) CCO 1:1 and (d) CCO 1:2 electrodes at 10 mV.

5.3.12 Cycling stability

Figure 5.14 demonstrates the cycle life study of all three nanocomposites CCO 2:1, CCO 1:1, and CCO 1:2 for 500 cycles at a current density of 1 Ag^{-1}. For initial 250 cycles of CCO 1:1 capacity increases gradually to 1055 $mAhg^{-1}$, because of gradual activation process which enhances the kinetics of Li ion diffusion and polymeric gel-like film formation with better electrolyte infiltration during cycling.[19] Further, over 500 cycles the capacity value decreases to 820 $mAhg^{-1}$ with 78% capacity retention and has more than 99% Coulombic efficiency. Additionally, high surface area of electrode can provide more accessible reactive sites which leads to increased lithium-ion storage capacity.[2] CCO 2:1 nanocomposite delivers less specific capacity value of 583 $mAhg^{-1}$ at 500^{th} cycles because of excessive amount of carbon in the composite. Whereas CCO 1:2 delivers 696 $mAhg^{-1}$ of specific capacity value at 500^{th} cycle due to less surface area and more li ion diffusion resistance caused by thick deposition of Co_3O_4 NPs on carbon surface.

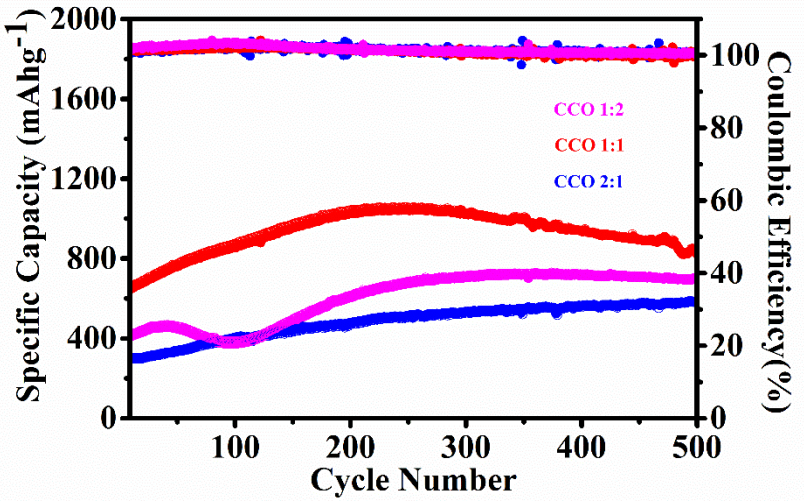

Figure 5.14: Cycling stability of CCO 2:1, CCO 1:1 and CCO 1:2 electrodes at 1 Ag^{-1} of current density for 500 cycles.

5.3.13 Post cycling study

EIS measurements were done to measure the resistance of electrode during continuous charge discharge process for CCO 1:1 electrode. Figure 5.15a shows the Nyquist plot of CCO 1:1 at different steps of cycling (fresh cell and after 10^{th}, 30^{th}, 60^{th}, 100^{th} and 250^{th} cycles of charge-discharge) at 1 Ag^{-1} of current density. It can be seen that the charge transfer resistance and Warburg diffusion resistant of electrode decreases on increasing cycle number, and after 250^{th} cycle both charge transfer and diffusion resistance are very less and displays two prominent semicircles. First semicircle in higher frequency region appears due to SEI layer resistance and another semicircle at mid frequency region appear due to charge transfer resistance. After 250 cycles, formation of SEI layer with optimum thickness on the electrode surface and penetration of electrolyte increases the electronic/ionic transport during cycling and reduce both the charge transfer as well as Warburg diffusion resistance of the cell which aids in increasing the specific capacity of the electrode.[20, 21]. Thus, cycle life study of the CCO 1:1 electrode corroborate by impedance measurement at different levels of cycling. Further, TEM analysis was done to investigate the morphological changes of electrode after 500 cycles of Charge-Discharge at 1 Ag^{-1} of current density. Figure 5.15b and 5.15c represents the low and high resolution TEM images of CCO 1:1 electrode after cycling where it can be seen that the morphology of the CCO 1:1 nanocomposites is still retained fairly even after continuous 500 cycles of charge-discharge.

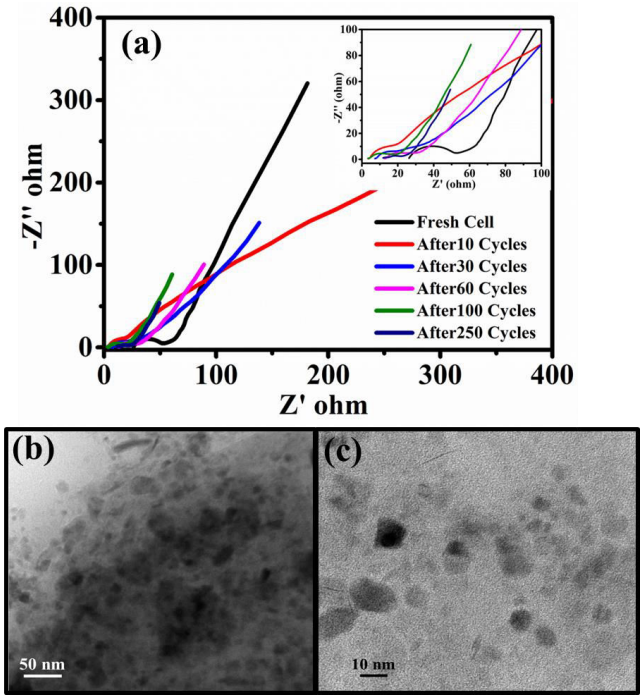

Figure 5.15: (a) Nyquist plots of AC impedance spectra CCO 1:1 electrode at different cycles of Charge-discharge, (b-c) TEM image of CCO 1:1 at 1Ag^{-1}after 500 cycles.

5. 4 Conclusion

We reported a facile freeze drying process to develop a well-designed Co_3O_4 NPs anchored on f-CNH foam architecture as composite anode material for LIBs. The Co_3O_4-CCO nanocomposite exhibit the best lithium storage capacity and good cycling stability when carbon content is around 45 weight %, retaining a discharge capacity of 820 $mAhg^{-1}$ up to 500 cycles with more than 99% of Coulombic efficiency. At 5 Ag^{-1} of high current density it delivers 702 $mAhg^{-1}$ of high specific capacity value. The improved battery performance and cycle life of the 3D CCO 1:1 hierarchical nanocomposite are due to the intimate integration which increase the reversible specific capacity by reducing the number of active sites of f-CNH matrices. In Co_3O_4 NPs and f-CNH foam nanocomposite, f-CNH act as an electronically conductive network and elastic buffer for the Co_3O_4 NPs to prevent the volumetric expansion and contraction during the lithiation and delithiation process. More surface area and three-dimensional (3D) interconnected mesopore structure of f-CNH foam provides essential channels for charge transport. Hence, 3D CCO 1:1 hierarchical nanocomposite with excellent electrochemical performance could find potential applications as anode materials for LIBs.

5.5 References

[1] J. He, Y. Liu, Y. Meng, X. Sun, S. Biswas, M. Shen, Z. Luo, R. Miao, L. Zhang and W. E. Mustain, *RSC Adv.*, 2016, **6**, 24320-24330.

[2] F. Hao, Z. Zhang and L. Yin, *ACS Appl. Mater. Interfaces*, 2013, **5**, 8337-8344.

[3] N. Karousis, I. Suarez-Martinez, C. P. Ewels and N. Tagmatarchis, *Chem. Rev.*, 2016, **116**, 4850-4883.

[4] A. B. Deshmukh and M. V Shelke, *Rsc Adv.*, 2013, **3**, 21390-21393.

[5] L. Yu, P. Zhang, H. Dai, L. Chen, H. Ma, M. Lin and D. Shen, *RSC Adv.*, 2017, **7**, 39611-39616.

[6] P. Jing, P. Wang, M. Liu, W. Gao, Y. Cui, Z. Wang and Y. Pu, *J. Alloys Compd.*, 2019, **774**, 236-243.

[7] L. Pan, H. Zhao, W. Shen, X. Dong and J. Xu, *J. Mater. Chem. A*, 2013, **1**, 7159-7166.

[8] X. Tian, X. Sun, Z. Jiang, Z.-J. Jiang, X. Hao, D. Shao and T. Maiyalagan, *ACS Appl. Energy Mater.*, 2017, **1**, 143-153.

[9] C. K. Ranaweera, C. Zhang, S. Bhoyate, P. K. Kahol, M. Ghimire, S. R. Mishra, F. Perez, B. K. Gupta and R. K. Gupta, *Mater. Chem. Front.*, 2017, **1**, 1580-1584.

[10] D. S. Su, J. J. Delgado, X. Liu, D. Wang, R. Schlögl, L. Wang, Z. Zhang, Z. Shan and F. Xiao, *Chem. Asian J.*, 2009, **4**, 1108-1113.

[11] S. D. Gardner, C. S. K. Singamsetty, G. L. Booth, G.-R. He and C. U. Pittman Jr, *Carbon N. Y.*, 1995, **33**, 587-595.

[12] J. Zhao, Z. Liu, Y. Qin and W. Hu, *CrystEngComm*, 2014, **16**, 2001-2008.

[13] C. Cheng, G. Zhou, J. Du, H. Zhang, D. Guo, Q. Li, W. Wei and L. Chen, *New J. Chem.*, 2014, **38**, 2250-2253.

[14] L. Shen and C. Wang, *Electrochim. Acta*, 2014, **133**, 16-22.

[15] G. Huang, F. Zhang, X. Du, Y. Qin, D. Yin and L. Wang, *ACS Nano*, 2015, **9**, 1592-1599.

[16] Z. Li, X.-Y. Yu and U. Paik, *J. Power Sources*, 2016, **310**, 41-46.

[17] G. Zhou, D.-W. Wang, L. Li, N. Li, F. Li and H.-M. Cheng, *Nanoscale*, 2013, **5**, 1576-1582.

[18] M. V Reddy, T. Yu, C.-H. Sow, Z. X. Shen, C. T. Lim, G. V Subba Rao and B. V. R. Chowdari, *Adv. Funct. Mater.*, 2007, **17**, 2792-2799.

[19] J. Mujtaba, H. Sun, G. Huang, K. Mølhave, Y. Liu, Y. Zhao, X. Wang, S. Xu and J. Zhu, *Sci. Rep.*, 2016, **6**, 20592.

[20] Y. Bai, X. Wang, X. Zhang, H. Shu, X. Yang, B. Hu, Q. Wei, H. Wu and Y. Song, *Electrochim. Acta*, 2013, **109**, 355-364.

[21] T. Liu, A. Garsuch, F. Chesneau and B. L. Lucht, *J. Power Sources*, 2014, **269**, 920-926.

Chapter 6

Study of Nanocomposite Anode Material Comprising Co_3O_4 Nanoparticles Decorated on Nitrogen and Sulphur co-doped Carbon Spheres for High Performance Li-Ion Battery

Conversion type anode materials are intensely being studied for Li-ion battery (LIB) for their potentially higher capacities over current graphite based anode. This work describes development of high capacity and stable anode from a nanocomposite of N and S co-doped carbon spheres (NSCS) with Co_3O_4 (NSCS-Co_3O_4). Hydrothermal reaction of saccharose with L-cysteine has been carried out followed by its carbonization. CS used as support for conversion type materials provides efficient electron/ion transfer channels enhancing the overall electrochemical performance of the electrodes. Additionally hetero atoms doped in carbon matrix alter the electronic properties, often increasing the reactivity of the carbon surface and reported to be effective for anchoring metal oxide nanoparticles. Consequently, the NSCS-Co_3O_4 nanocomposites developed in this work exhibit enhanced and stable reversible specific capacity over the cycling. Stable cycling behavior is observed at 1 Ag^{-1} with 1285 $mAhg^{-1}$ of specific capacity retained after 350 cycles along with more than 99% of coulombic efficiency. This material shows an excellent rate capability with specific capacity retained to 745 $mAhg^{-1}$ even at high current density of 5 Ag^{-1}.

6.1 Introduction

As discussed in previous chapters, Co_3O_4 can be produced in large quantity due to low cost and has been demonstrated as a potential high energy material for LIB with a theoretical capacity of around 890 $mAhg^{-1}$. [1] However, the commercial application of Co_3O_4 has not been viable yet due to its low electrical conductivity, high volume expansion during charging and discharging cycles, capacity fading at high current density, and poor cyclic stability.[2, 3] Some new synthesis approaches are demonstrated for producing nanostructures of Co_3O_4 with different morphologies having various pore distribution and specific surface area leading to high capacity and improved stability for LIB. [4-11] High surface area and small dimension of these nanostructures helps to improve the interaction of electrode-electrolyte surface and reduces the Li-ion diffusion length into the solid surface. However, the high volume expansion of Co_3O_4 results into crystal deformation and agglomeration of anode material restricting the capacity gain. [12] It is reported that making composite of metal oxide nanostructures with conducting carbon networks compensates for the volume expansion and the lacking conductivity which also enhances the electrochemical performance. This strategy helps in remarkably reducing the volume expansion of Co_3O_4 and also the carbon matrix improves the conduction of electrons to the current collector. [13] Different carbon forms such as nanoonions, nanotubes, nanofibers, graphene sheets and 3d porous carbon networks are widely used to make composite with Co_3O_4 and demonstrated the anodic capacity enhancement.[13-20] Among these carbon structures spherical carbon has maximum packing density, low surface to volume ratio and high structural resistance. However, there is large scope for further improvements in the performance by introducing defects in carbon matrices, e.g. doping of heteroatoms such as N, B, and S etc.[21-24] These dopant atoms on the surface of carbon materials improve reactivity with enhanced lithiation capacity. Additionally, the large atomic size of sulfur can increase the interlayer spacing of the graphitized carbon, creates micropores into the carbon matrix and improves the charge storage capacity of the carbon material. Moreover, lone pair electrons of N and S atoms contribute to extending the conjugated electron clouds of carbon matrix resulting in increased conductivity which enhances the rate capacity and cycle life of the electrode material.

Taking in consideration of the potential effects of co-doped carbon matrix for stable performance of high energy conversion type anode material like metal oxides, we have synthesized a composite of Nitrogen and Sulphur co-doped Carbon Spheres and Co_3O_4 as an anode material for LIB with enhanced reversible capacity and potential for large-scale production. N and S co-doping in carbon spheres are found to efficiently inhibit the

agglomeration of Co_3O_4 NPs, facilitate robust interactions between the electrode and Li ions, which can improve the kinetics of lithium diffusion and reduce the charge transfer resistance. NSCS-Co_3O_4 nanocomposite exhibits excellent rate performance with Specific capacity of 745 $mAhg^{-1}$ at high current density of 5 Ag^{-1}. It retains remarkable and stable discharge capacity of 1285 $mAhg^{-1}$ at 1 Ag^{-1} after 350 cycles with more than 99% coulombic efficiency.

6.2 Experimental section

6.2.1 Synthesis of NS co-doped carbon spheres

For the synthesis of NS co-doped carbon spheres, saccharose and L-cysteine in 5:1 ratio were used as precursors. In a typical experiment, 10 g of saccharose was first dissolved in 120 ml of de-ionized water followed by the addition of 2 g of L-cysteine under stirring. The resultant solution was then treated hydrothermally at 180 °C for 24 h. After cooling down to room temperature, the obtained product was washed by filtration several times with de-ionized water and ethanol followed by overnight drying at 80 °C. After drying the above prepared material was annealed at 800 ^{O}C in an inert atmosphere for 1 h. For the synthesis of non-doped CS, only saccharose was treated hydrothermally.

6.2.2 Synthesis of Co_3O_4 NPs composite with NS co-doped carbon spheres

To synthesize NSCS-Co_3O_4 nanocomposite, 50 mg of NSCS were dispersed in 20 ml of ethanol by ultra-sonication process and a separate solution of 0.29 g of $Co(NO_3)_2.6H_2O$ in 20 mL of ethanol was prepared by stirring. Both solutions were mixed under stirring for 30 minutes followed by addition of ammonia solution ($NH_3.H_2O$, 25%). The obtained solution was then transferred into a Teflon-lined stainless steel autoclave and heated at 190 ^{O}C for 24 h. Finally, the reaction mixture was washed by filtration with DI water and ethanol followed by overnight drying at 80 °C. For comparison, pure Co_3O_4 was synthesized without the addition of NSCS and CS-Co_3O_4 with non-doped CS.

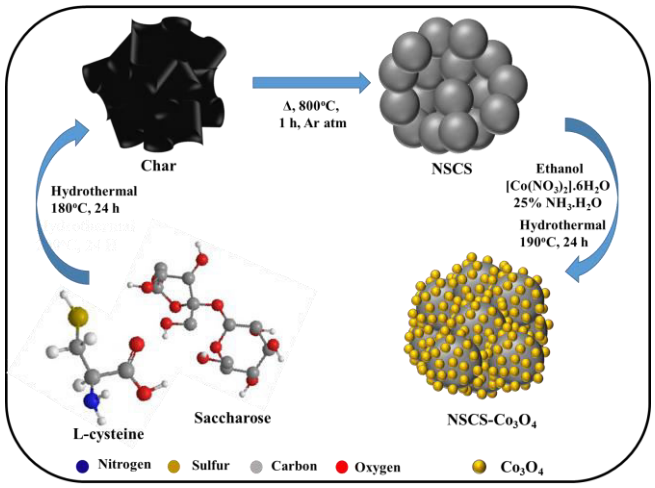

Figure 6.1: Schematic representation of the synthesis of NSCS-Co3O4 nanocomposite.

6.2.3 Material Characterization

Powder X-ray Diffraction (p-XRD) patterns were recorded in a Phillips PAN analytical diffractometer with CuKα radiation (λ = 1.5406 Å). Transmission electron microscopy (TEM) was carried out by Tecnai F30 FEG machine operated at an accelerating voltage of 300 kV. Morphology and chemical composition of the ternary hybrid composite were examined by using Quanta 200 3D, FEI scanning electron microscope (SEM). X-ray photoelectron spectroscopic (XPS) measurements were carried out on a VG Micro Tech ESCA 3000 instrument. Thermogravimetric analysis (TGA) was performed with the SDT model Q600 of TA instrument with a heating rate at 10 °C/min in air atmosphere.

6.2.4 Electrochemical Characterization

The electrochemical properties of the above-prepared electrode materials were examined in a two-electrode coin cell (CR2032) configuration. The Co_3O_4 nanostructures, non-doped CS and NSCS-Co_3O_4 were tested as anode material by preparing their slurry with conducting carbon additive (super P) and a binder (polyvinylidene difluoride, PVDF). Further, the slurry was coated on Cu foil, which serves as the current collector and subsequently dried at 90ºC for overnight before assembling the cell in an Ar-filled glove box. The coin cells were assembled with lithium metal foil as the counter electrode, a quartz microfiber paper (Whatman) as separator and 1 M $LiPF_6$ in ethylene carbonate (EC)-diethyl carbonate (DEC) (1: 1 by volume) as the electrolyte. Cyclic voltammetry (CV) was performed using SP-300 EC Biologic potentiostat at a scan rate of 0.25 mVs^{-1} in the potential window of 0.01 V - 3.0 V. The galvanostatic discharge-charge cycling of the cells was carried out at different current densities between the potential windows of 0.01 V - 3.0 by using MTI battery analyser. The electrochemical impedance spectroscopy (EIS) was used to measure the impedance in the frequency range from 100 kHz to 50 mHz with AC amplitude of 10 mV.

6.3 Results and discussion

6.3.1 Powder X-Ray Diffraction

The crystallographic structure and phase purity of the as-prepared materials were investigated by p-XRD spectra. The p-XRD of the synthesized materials is given in figure 6.2. p-XRD spectra of CS and NSCS samples are showing the presence of two broad peaks appearing at 24.2° and 43.6° of 2θ corresponding to the (002) and (101) planes of graphitized carbon, respectively. p-XRD spectra of Co_3O_4, CS-Co_3O_4 and NSCS-Co_3O_4 consist of peaks at 19.0°, 31.29°, 36.94°, 44.86°, 59.29° and 65.27° of 2θ corresponding to (111), (220), (311), (400), (511) and (440) planes respectively indicating Co_3O_4 spinel structure with a face-centred cubic lattice (JCPDS Card no. 42-1467). Peaks of the CS and NSCS are not detected in the

composite samples as the carbon spheres are completely covered by Co_3O_4 NPs. No residual/impurity peaks could be seen in the p-XRD spectra indicating the good quality of the samples.

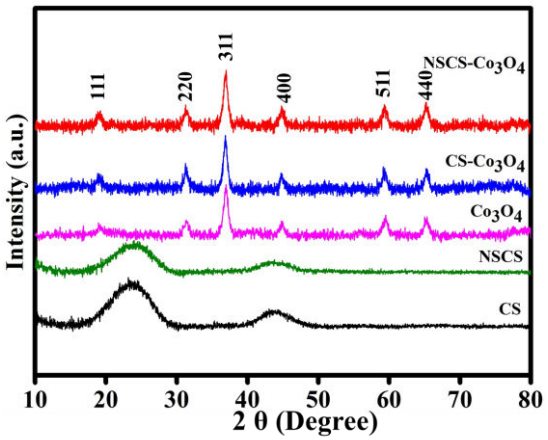

Figure 6.2: p-XRD pattern of CS, NSCS, Co3O4, CS-Co_3O_4 and NSCSs- Co_3O_4.

6.3.2 Thermogravimetric analysis

TGA was performed for all five samples in air atmosphere at a rate of 10 °C min^{-1} up to 900 °C to quantify the weight percentage of individual components in the composites. In figure 6.3, the weight loss below 150 °C can be attributed to the release of adsorbed moisture and gases from the surface of the samples.[17] CS and NSCS show complete weight loss after heating at 600 °C. In case of CS-Co_3O_4 and NSCS-Co_3O_4 nanocomposites significant weight loss occurred from 400 °C to 500 °C and then shows stable TGA profile indicating the removal of carbon from the composites and the residual corresponds to the weight percentage of Co_3O_4. Hence, Co_3O_4 and carbon content in the composites is approximately 60 % and 40 %, respectively.

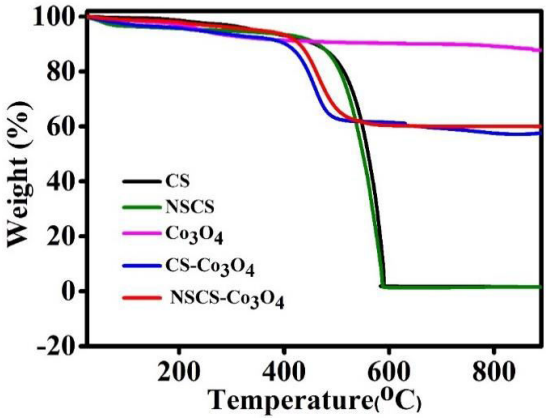

Figure 6.3: TGA analysis of Co_3O_4, CS-Co_3O_4 and NSCS-Co_3O_4.

6.3.3 X-ray photoelectron spectroscopy

XPS analysis was carried out to find out the oxidation states of cobalt and elemental composition in the NSCS-Co_3O_4 composite. Figure 6.4a shows the XPS survey spectra of the

composite which displays the presence of Co 2p, C 1s, N 1s and S 2p peaks. In figure 6.4b-6.4e, core level peaks are further deconvoluted to understand the surface composition of the constituting elements. As shown in figure 6.4b, a combination of tetrahedral Co^{2+} and octahedral Co^{3+} contributes to the doublet 2p spectral profile of Co_3O_4 separated in high and low energy component due to spin-orbit coupling corresponding to $2p_{1/2}$ to $2p_{3/2}$ with a separation of 15.2 eV.[25, 26] The deconvolution of Co 2p peak at 779.3 eV and 780.6 eV are assigned to Co^{3+} $2p_{3/2}$ and Co^{2+} $2p_{3/2}$, respectively. The other spin-orbit components, Co^{3+} $2p_{1/2}$ and Co^{2+} $2p_{1/2}$, have been detected at 794.5 and 795.8 eV, respectively. The peaks at 782.1 eV and 797.3 eV may occur due to chemical shift of the main spin-orbit components resulting from chemical interaction of Co cations with surface hydroxyl groups. In addition to these peaks, four small peaks are also observed corresponding to the shake-up satellite peaks of Co_3O_4 in the high binding energy side of $2p_{3/2}$ and $2p_{1/2}$ transitions indicate the co-existence of Co (II) and Co (III) on the surface of the material. Figure 6.4c shows four deconvolution peaks in C 1s spectra at 284.6, 285.6, 286.5 and 288. 5 eV which corresponds to the sp^2 hybridized carbon, sp^3 hybridized carbon, C-O/C-N and C=O bonds, respectively.[27-29] The high resolution S 2p spectra (figure 6.4d) shows two peaks at 163.9 eV and 165.2 eV which may correspond to the presence of C-S-C and C=S, respectively and weak peaks at around 168 eV can be related to the oxidized sulfur.[30, 31] The high-resolution N 1s spectrum (figure 6.4e) with four deconvoluted peaks at 398.5 eV, 399.7 eV, 400.7 eV and 401.6 eV can be attributed to the presence of pyridinic N, pyrrolic N, quaternary-graphitic N and oxidized species, respectively.[32]

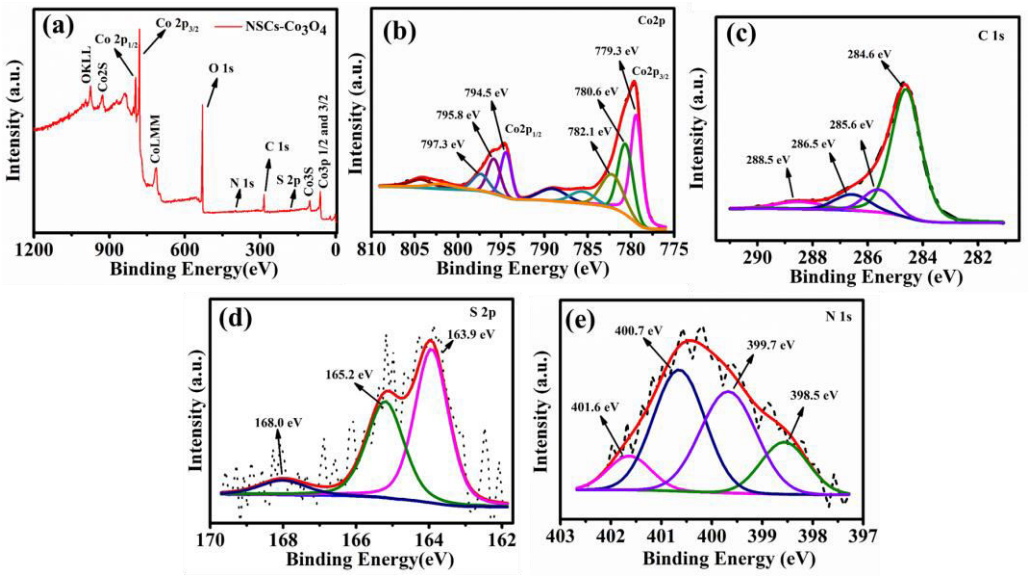

Figure 6.4: (a) XPS survey scan of NSCS-Co_3O_4. Deconvoluted spectra of (b) Co2p (c) C1s (d) S 2p and (e) N 1s.

6.3.4 Scanning electron microscopy

The surface and structural morphology of the as-prepared materials were observed by SEM and the images are shown in figure 6.5. Figure 6.5a represents the micron sized particles of CS. Figure 6.5b shows agglomerated Co_3O_4 nanoparticles which are randomly distributed in clusters. Figure 6.5c depicts Co_3O_4 NPs decorated on the surface of CS. Here, Co_3O_4 NPs are distributed unevenly on the surface of CS leading to clustering. Whereas in NSCS-Co_3O_4 (figure 6.5d), Co_3O_4 NPs are well distributed and homogeneously decorated on the NSCS surface forming an extended nanosheets like structure which uniformly covers the surface of NSCS. It is also observable from images that N and S doping is playing a vital role for the uniform nucleation and growth of Co_3O_4 nanoparticles by providing well dispersed nucleation sites in NSCS.

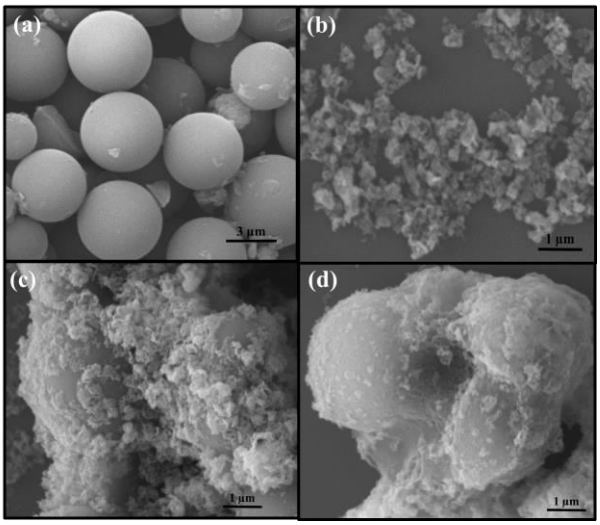

Figure 6.5: (a) ESEM images of (a) CS, (b) Co_3O_4, (c) CS-Co_3O_4 and (d) NSCS-Co_3O_4

Morphological control on the uniform growth of Co_3O_4 NPs through N, S doping can be highlighted with the help of atomic distribution of different elements over the surface of NSCS-Co_3O_4. SEM elemental maps are shown in figures 6.6a-6.6f and they indicate the presence of all five elements (Co, C, N, S and O) which are homogeneously distributed throughout the sample.

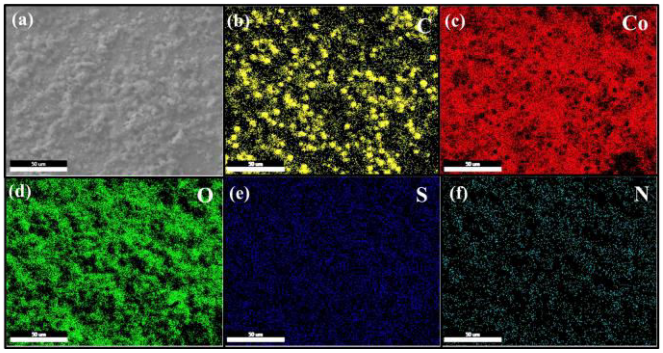

Figure 6.6: (a) ESEM elemental mapping images of (b) C, (c) Co, (d) O, (e) S and (d) N.

6.3.5 Transmission electron microscopy

TEM characterization was performed on all samples to provide an insight into the inner architecture and the crystallographic structure of as prepared materials. Figure 6.7a represents the TEM image of well dispersed carbon spheres with diameter ranging between 2 to 5 micrometres. Figure 6.7b shows interconnected network of Co_3O_4 nanoparticles with 10-20 nm size. Higher magnification image in figure 6.7c clearly verifies the cubic structure of Co_3O_4 NPs. The inset images, also indicate inter-planar spacing of 0.46 nm and 0.28 nm, corresponding to (111) and (220) planes of the face centred cubic phase of Co_3O_4, respectively.[33] Figure 6.7d attributes that N and S co-doped carbon spheres are closely and densely surrounded by Co_3O_4 NPs which are extended into sheet like structures due to uniform coverage over the NSCS surface.

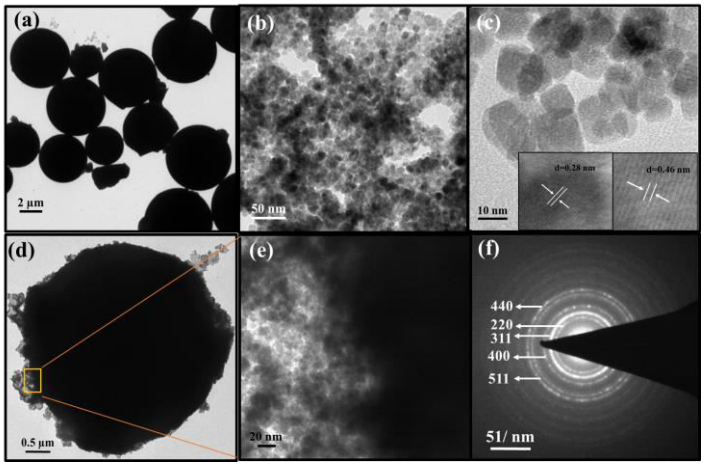

Figure 6.7: TEM images of (a) CSs, (b) low and (c) high resolution images of Co_3O_4, (d) low resolution image of NSCS- Co_3O_4, d) high resolution image of NSCS- Co_3O_4, (f) SAED pattern of NSCS- Co_3O_4.

The high magnification image (figure 6.7e) of NSCS-Co_3O_4 also reveals the surface boundary of NSCS and Co_3O_4 NPs aggregated like sheets, which indicates the homogeneous distribution of Co_3O_4 NPs on the surface of NSCS. Figure 6.7f illustrates a typical SAED pattern of the NSCS-Co_3O_4 nanocomposites. The diffraction rings correspond to (220), (311), (400), (511), and (440) planes of polycrystalline Co_3O_4.[34]

6.3.6 Cyclic voltammetry

Lithium storage properties of Co_3O_4, CS-Co_3O_4 and NSCS-Co_3O_4 composites were examined in a coin cell configuration versus Li/Li^+ under identical conditions with cyclic voltammetry and results are shown in figure 6.8 (a-c). The CV measurements for Co_3O_4, CS-Co_3O_4 and NSCS-Co_3O_4 composite electrodes were done at a scan rate of 0.25 mVs^{-1} in the potential window of 0.01 V to 3.0 V. A distinct and irreversible reduction peak appeared at 0.77 V in the first cathodic scan of Co_3O_4 CV curve (Figure 6.8 a) which is due to the reduction of Co_3O_4 to metallic Co and formation of amorphous Li_2O by conversion reaction.

Simultaneous decomposition of electrolyte takes place to form SEI layer on the electrodes surface.[19, 35] From second cycle onwards, cathodic peak splits into two distinguishable peaks appeared nearly at 1.01 V and 1.23 V with lesser intensity which is due to multistep reaction during lithiation and presence of some irreversible transformation which gives structure modification in the first cycle. [19, 23, 35] Moreover, two broad peaks are observed during anodic scan at potentials 1.35 V and 2.1 V which can be attributed to the oxidation of metallic Co. The electrochemical reaction mechanism of Co_3O_4 involves the formation and decomposition of Li_2O, accompanied by the reduction of Co^{3+} to Co^{2+} and Co^{2+} to Co and the oxidation of Co to Co^{2+} and $Co2^{+}$ to Co^{3+} through an intermediate of CoO. This multiple electron process can be represented by equations (1) and (2). [36]

$$Co_3O_4 + 2Li^+ + 2e^- \leftrightarrow Li_2O + 3CoO \ldots (1)$$

$$3CoO + 6Li^+ + 6e^- \leftrightarrow 3Li_2O + 3Co \ldots (2)$$

In case of the CS-Co_3O_4 electrode, as shown in figure 6.8b, during first cathodic scan the reduction peak was observed at 0.71 V and subsequent cathodic peaks (2nd cycle onwards) were observed at 0.87 V and 1.29 V vs. Li/Li^+, whereas the anodic peaks were obtained at approximately 1.37 V and 2.14 V. Figure 6.8c represents the CV curve of NSCS-Co_3O_4 composite where, the first cathodic peak appeared at 0.85V and subsequent cathodic peaks appeared at 0.96 and 1.34 V, whereas, anodic peaks were observed at 1.3 V and 2.1 V. In NSCS-Co_3O_4 composite the subsequent cycles represents the proper overlapping of anodic and cathodic peaks, an indication of the good electrochemical reversibility of the electrode material.

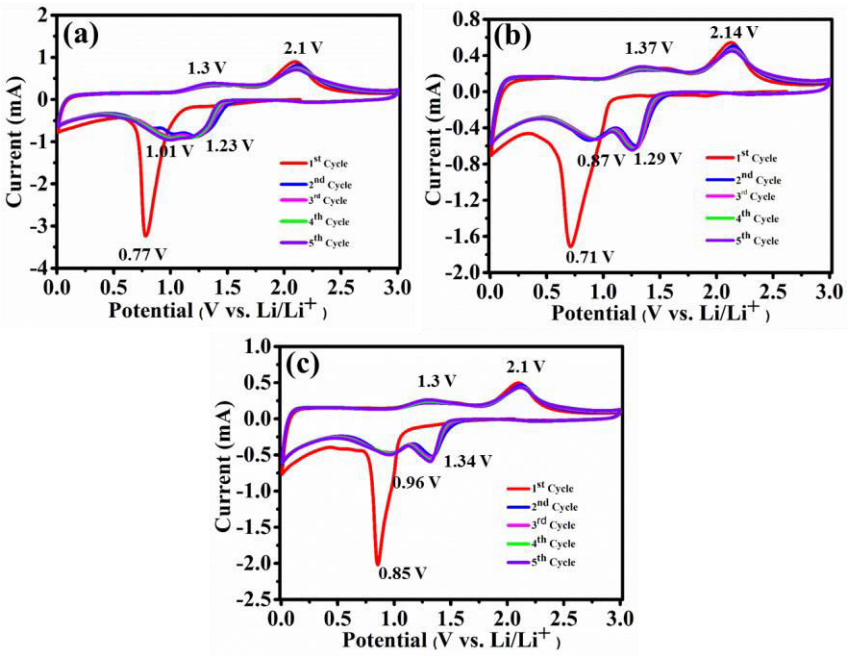

Figure 6.8: Cyclic voltammetry curves of (a) Co_3O_4 nanoparticles (b) CS-Co_3O_4 (c) NSCS-Co_3O_4 composite electrodes over 6 cycles at scan rate of 0.25 mVs^{-1} and potential range of 0.01-3V vs. Li/Li^+.

6.3.7 Charge-discharge measurements

The GCD curves are shown in figure 6.9 (a-c) for Co_3O_4, CS-Co_3O_4 and NSCS-Co_3O_4, respectively within a voltage window of 0.01-3.00 V vs. Li/Li^+. GCD curves were recorded at a current density of 100 mAg^{-1} and the obtained results are in well accordance with the CV results. In the charge-discharge profiles of Co_3O_4, CS-Co_3O_4 and NSCS-Co_3O_4, an extended voltage plateau is observed at around 1.1 V resulting from the lithiation of Co_3O_4 and the formation of Co and Li_2O. In the charge curves, the slope region from 1.2 to 2.5 V corresponds to the reversible oxidation of Co_3O_4.

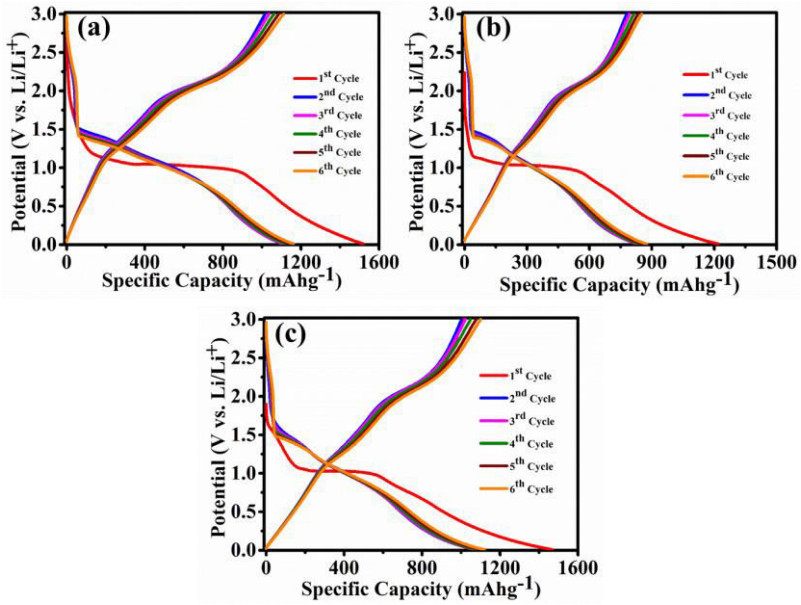

Figure 6.9: Galvanostatic charge-discharge profiles of (a) Co_3O_4 nanoparticles (b) CS-Co_3O_4 (c) NSCS-Co_3O_4 composite electrode at current density of 100 mAg^{-1}.

Discharge capacity values calculated from second cycle are around 1106 $mAhg^{-1}$, 836 $mAhg^{-1}$ and 1075 $mAhg^{-1}$ for Co_3O_4, CS-Co_3O_4 and NSCS-Co_3O_4, respectively. Lower specific capacity value of CS-Co_3O_4 compare to bare Co_3O_4 is probably due to the addition of CS but in case of NSCS-Co_3O_4, reversible capacity increases due to N and S co-doping in CS which may provide large quantity of edge defects with enhanced electronic conductivity and improved lithium-ion accessibility [31]. Another reason could be homogeneous distribution of Co_3O_4 nanoparticles on the surface of NSCS which may allow better charge transfer.

3.2.8 Electrochemical impedance spectroscopy

Impedance measurements of Co_3O_4, CS-Co_3O_4 and NSCS-Co_3O_4 electrode were carried out in frequency range of 100 kHz to 0.05 Hz at 10 mV at room temperature. As shown in figure 6.10, Nyquist plots of all three electrodes consist of a depressed semicircle at high frequency region and an inclined line at low frequency region. The high-frequency semicircle is attributed to the SEI film formation, contact resistance, and charge transfer resistance on

electrode/electrolyte interface, whereas the inclined line in low frequency region corresponds to the lithium-diffusion process within electrodes. [37] The charge transfer resistance is calculated by fitting circuit model. It is observed to be lower for NSCS-Co_3O_4 (65.72 Ω) as compared to bare Co_3O_4 (152.5 Ω) and CS-Co_3O_4 (106.1 Ω) implying more conducting nature and faster Li^+ diffusion rate of NSCS-Co_3O_4 nanocomposite. Reduced charge transfer resistance of NSCS-Co_3O_4 electrode is possibly due to the carbon matrix which reduces the mechanical strain and avoid volume expansion during charge-discharge process. Additionally, N and S co-doping enhances the electronic conductivity, providing continuous and rapid electron transport, which may accelerate the Li-ion storage capacity of electrode material.

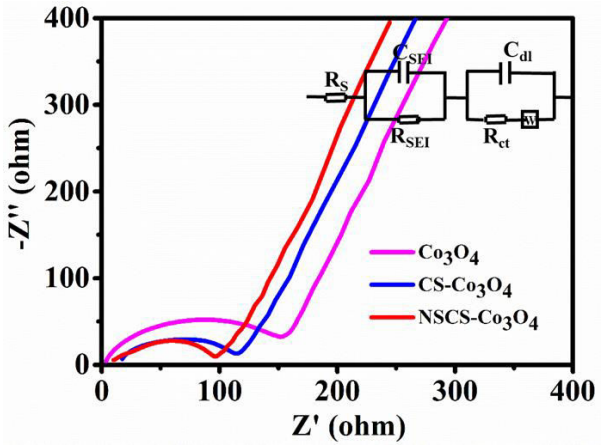

Figure 6.10: Impedance spectra of Co_3O_4, CS-Co_3O_4 and NSCS-Co_3O_4 at 10 mV.

6.3.9 Cycling stability

Figure 6.11 shows the cyclability of NSCS-Co_3O_4 composite at a current density of 1 Ag^{-1} for 350 cycles. It can be observed that the as prepared NSCS-Co_3O_4 electrode exhibits long cycle life over 350 cycles with higher specific capacity value and very good coulombic efficiency. Over the cycling more reactive sites of NSCS-Co_3O_4 are activated and contribute in lithium ion storage which is reflecting in gradually increasing specific capacity up to 919 $mAhg^{-1}$ for initial 25 cycles. Additionally, hetero atoms doped carbon spheres provide more reactive sites leading to the increased lithium-ion storage capacity while cycling.[37-39] Afterwards, for 70 cycles the capacity value observed to be decreasing to 720 $mAhg^{-1}$, which may be due to deterioration of the electrode material on continuous charge-discharge process resulting into increased charge transfer resistance which is an inherent characteristic of the TMO electrodes [40, 24]. Further, increase in capacity value is observed up to 250 cycles (1331 $mAhg^{-1}$) and then remain fairly stable for over 350 cycles with 96.5% capacity retention (1285 $mAhg^{-1}$) as well as >99 % coulombic efficiency. This trend in discharge capacity is observed probably due to the enhanced kinetics of Li-ion diffusion by the gradual activation process and the formation of the polymeric gel-like film with better electrolyte infiltration during cycling.[41]

In addition, heteroatom doped carbon spheres reduces the volume expansion during cycling and provides structural stability to Co_3O_4 NPs. NSCS increases the electronic and ionic conductivity of the composite electrode leading to fast Li^+ insertion kinetics in Co_3O_4.[23]

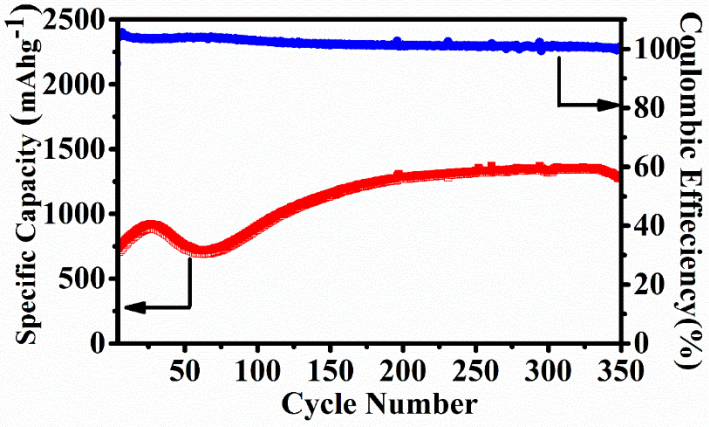

Figure 6.11: Cycling stability of NSCS-Co_3O_4 at 1 Ag^{-1}

6.3.10 Rate performance

Figure 6.12 illustrates the comparative rate performance of the Co_3O_4, CS-Co_3O_4 and NSCS-Co_3O_4 electrodes after continuous charge discharge of 251 cycles at 1 Ag^{-1} and then varying current densities between 0.1 Ag^{-1} to 5 Ag^{-1}. As seen in figure 6.12, among all, NSCS-Co_3O_4 electrode exhibit an excellent rate performance with reversible discharge capacities of 1807, 1730, 1616, 1419, and 1151 $mAhg^{-1}$ at 0.1, 0.25, 0.5, 1 and 2 Ag^{-1}, respectively. Even at a high current density of 5 Ag^{-1}, the NSCS-Co_3O_4 electrode delivers a high specific capacity of 745 $mAhg^{-1}$. On the other hand, bare Co_3O_4 exhibits 1060 $mAhg^{-1}$ at 0.1 Ag^{-1} and 384 $mAhg^{-1}$ at 5 Ag^{-1} while as tested CS-Co_3O_4 composite electrode delivers specific capacity of 1237 $mAhg^{-1}$ at 0.1 Ag^{-1} and 437 $mAhg^{-1}$ at 5 Ag^{-1}. After varying the current densities again all the electrodes are subjected to charge-discharge test at 0.1 Ag^{-1}, wherein, NSCS-Co_3O_4 showed 1889 $mAhg^{-1}$ of specific capacity, whereas, Co_3O_4 and CS-Co_3O_4 delivered 1007 and 1356 $mAhg^{-1}$ of specific capacity. The logic behind enhanced rate performance of the NSCS-Co_3O_4 nanocomposites could be the improved electron transfer due to nanostructured cobalt oxide as well as an increased electronic conductivity provided by the conducting carbon network, in addition, fast kinetics, and reduced volume expansion at higher current density are helping probably for NSCS-Co_3O_4. [23] To understand it in deep we have calculated Li -ion diffusion coefficient for all the electrodes.

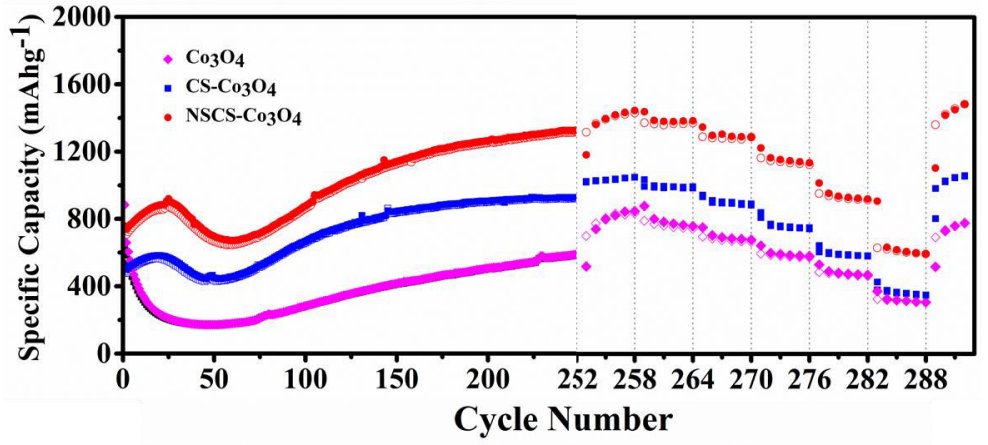

Figure 6.12: Rate performance of Co_3O_4, CS-Co_3O_4 and NSCS-Co_3O_4.

6.3.11 Li-ion diffusion coefficient calculation

The Li ion diffusion coefficient (D^{Li+}) is calculated by using following equation (3).[42]

$$D^{Li+} = \frac{1}{2}\{V_m/AF\sigma_w * \partial E/\partial x\}^2 \ldots\ldots\ldots\ldots\ldots (3)$$

Where, V_m is the molar volume, A is the area of the electrode surface (1.13 cm^2), F is the Faraday constant (96500 coulomb mol^{-1}), σ_w is the Warburg coefficient and $\partial E/\partial x$ is the slope of potential vs. Li concentration plot as shown in figure 6.13a. σ is obtained from the extrapolation of the straight line in the lower frequency region from the semicircle to real axis.[43]

$$Z_{re} = R_e + R_{ct} + \sigma\,\omega^{0.5} \ldots\ldots\ldots\ldots\ldots\ldots (4)$$

Where, σ is the slope for the plot of Z_{re} vs. the reciprocal root square of the lower angular frequencies ($\omega^{-0.5}$) as shown in figure 6.13b. The obtained values for **σ** are 141.422, 39.8 and 27.422 for Co_3O_4, CS-Co_3O_4 and NSCS-Co_3O_4, respectively.

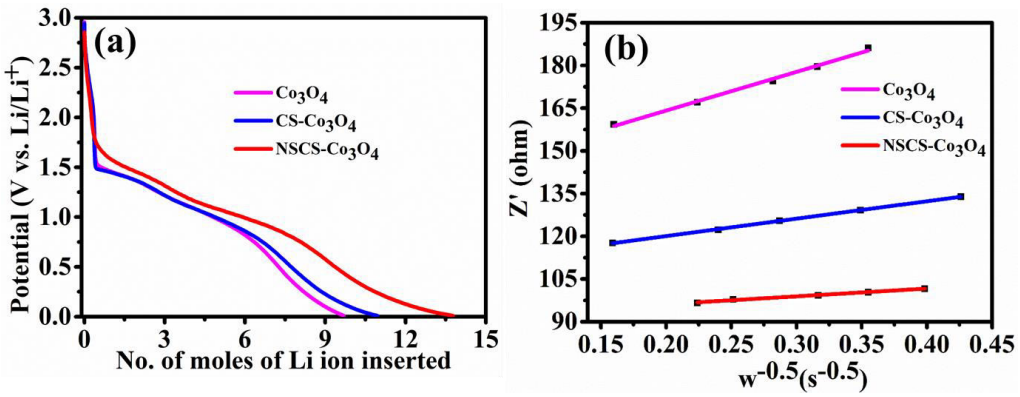

Figure 6.13: (a) Relationship between voltage and x mole of Li insertion in second discharge curve of Co_3O_4, CS-Co_3O_4 and NSCS-Co_3O_4, (b) Relationship between real resistance and frequency of Co_3O_4, CS-Co_3O_4 and NSCS-Co_3O_4.

As shown in table 6.1, the Li-ion diffusion coefficient of electrodes, Co_3O_4, CS-Co_3O_4 and NSCS-Co_3O_4, are 1.23 x 10^{-13} cm^2s^{-1}, 0.56 x 10^{-12} and 1.73 x 10^{-12} cm^2s^{-1}, respectively. Among them NSCS-Co_3O_4 composite is having higher Li-ion diffusion coefficient compare to other

electrode materials which agrees with the other electrochemical performances. Hetero atoms doped carbon spheres could increase the kinetics of Li-ions into the electrode surface by improving the conductivity of the electrode material, which help to improve the electrochemical performance of the battery.

Electrode	**σ_w(Ω $s^{-1/2}$)**	**X (mol cm^{-3})**	**D_{Li} (cm^2 s^{-1})**
Co_3O_4	135.96	0.1852	0.123 x 10^{-12}
CS-Co_3O_4	61.24	0.1768	0.56 x 10^{-12}
NSCS-Co_3O_4	27.42	0.1394	1.73 x 10^{-12}

Table 6.1: Values of σ_w, X, and D_{Li} for Co_3O_4, CS-Co_3O_4 and NSCS-Co_3O_4 as determined from EIS data.

6.3.12 Post cycling study

Figure 6.14a shows the Nyquist plots for NSCS-Co_3O_4 electrode in a fresh cell and after 10^{th}, 30^{th}, 60^{th}, 250^{th} cycles of charge-discharge at $1Ag^{-1}$ of current density. It can be seen in impedance spectrum that the charge transfer resistance of the cell decreases after 10^{th} cycle, whereas charge transfer resistance and Warburg impedance both increased after 30^{th} and 60^{th} cycles. This could be probably due to structural changes occurring in the electrode material for few cycles after the activation process.

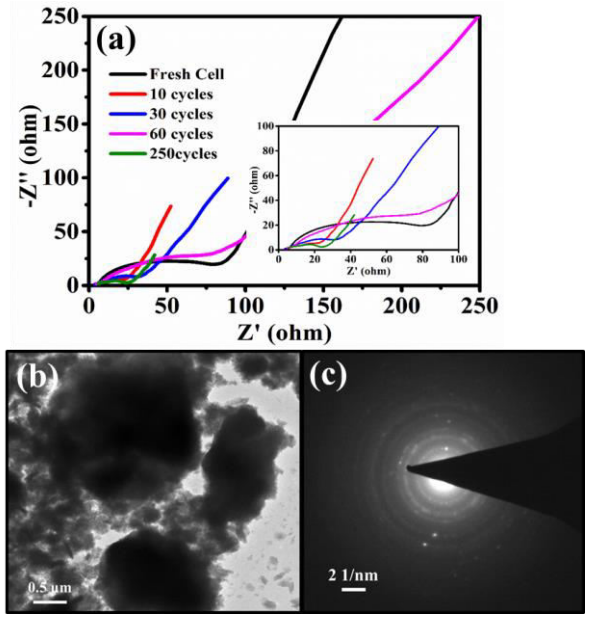

Figure 6.14: (a) Impedance spectra of NSCS-Co_3O_4 nanocomposite at different cycle number during cycling at 1 Ag^{-1} (b) TEM images and (c) SAED pattern of NSCS-Co_3O_4 nanocomposite electrode after 350 cycles at 1 Ag^{-1}.

The impedance spectrum taken after 250 cycles shows two prominent semicircles, one at the higher frequency range corresponding to the SEI layer resistance and the one at mid

frequency corresponding to charge transfer resistance. It is observed that after 250 cycles, both the Warburg as well as charge transfer resistance of the cell decreased on account of SEI layer formation with optimum thickness on the electrode surface and enhanced electronic/ionic transport due to electrolyte penetration leading to the increased specific capacity of the electrode. [42, 44] Thus, impedance measurement of the cell at different levels of cycling validate the cycle life study.

Furthermore, figure 6.14b represents the TEM images of the NSCS-Co_3O_4 electrode cycled at 1 Ag^{-1} over 350 cycles. It can be seen that the morphology of the NSCS-Co_3O_4 nanocomposite is still retained after the large number of charge-discharge cycles. An SAED pattern of the same electrode after the 350 cycles is presented in figure 6.14c; from the observations it appears that the electrode material has partially retained its polycrystalline nature after 350 charge-discharge cycles.

In summary, the excellent electrochemical performance of NSCS-Co_3O_4 can be attributed to synergetic effect of Co_3O_4 and N and S co-doped carbon spheres. Nano particles of Co_3O_4 effectively reduce the path length for lithium ion migration during charge/discharge process. Heteroatom doping offers suitable pathways for electron transfer and provide a good conductive matrix for Co_3O_4 nanoparticles. NSCS also acts as a buffer substrate to accommodate the volume changes of Co_3O_4 in the process of lithium ion insertion/extraction. Nitrogen and sulphur doping introduces defects, thus leading to the formation of disordered carbon structure, which tends to be electron accepting and provides anchor sites for the Co_3O_4 nanoparticles.

6.4 Conclusions

NSCS-Co_3O_4 nanocomposite is synthesized as an anode material with a significant potential for application in lithium ion batteries as high energy density material. Doped N and S atoms enhances the electronic conductivity and also provides binding sites for facile deposition of a large number of Co_3O_4 nanoparticles. It also provides the channels for charge and ionic transport, which effectively alleviates the aggregation of Co_3O_4 in the Li^+ insertion/extraction. As a consequence, NSCS-Co_3O_4 shows excellent rate performance and long cycle life. Among all three electrodes, NSCS-Co_3O_4 exhibit less charge transfer resistance with more Li-ion diffusion coefficient value of 1.73 x 10^{-12} cm^2s^{-1}.

6.5 References

[1] Y. Wang, B. Wang, F. Xiao, Z. Huang, Y. Wang, C. Richardson, Z. Chen, L. Jiao and H. Yuan, *J. Power Sources*, 2015, **298**, 203-208.

[2] M. R. Palacín, *Chem. Soc. Rev.*, 2009, **38**, 2565-2575.

[3] D. Gu, W. Li, F. Wang, H. Bongard, B. Spliethoff, W. Schmidt, C. Weidenthaler, Y. Xia, D. Zhao and F. Schüth, *Angew. Chemie*, 2015, **127**, 7166-7170.

[4] Y. Huang, C. Chen, C. An, C. Xu, Y. Xu, Y. Wang, L. Jiao and H. Yuan, *Electrochim. Acta*, 2014, **145**, 34-39.

[5] L. Zhan, S. Wang, L.-X. Ding, Z. Li and H. Wang, *Electrochim. Acta*, 2014, **135**, 35-41.

[6] J. Guo, L. Chen, X. Zhang and H. Chen, *J. Solid State Chem.*, 2014, **213**, 193-197.

[7] L. Tian, H. Zou, J. Fu, X. Yang, Y. Wang, H. Guo, X. Fu, C. Liang, M. Wu, P. K. Shen and Q. Gao, *Adv. Funct. Mater.*, 2010, **20**, 617-623.

[8] K. Qiu, Y. Lu, J. Cheng, H. Yan, X. Hou, D. Zhang, M. Lu, X. Liu and Y. Luo, *Electrochim. Acta*, 2015, **157**, 62-68.

[9] D. Liu, X. Wang, X. Wang, W. Tian, Y. Bando and D. Golberg, *Sci. Rep.*, 2013, **3**, 2543.

[10] X. Liu, Q. Long, C. Jiang, B. Zhan, C. Li, S. Liu, Q. Zhao, W. Huang and X. Dong, *Nanoscale*, 2013, **5**, 6525-6529.

[11] Y. Zhang, Y. Wu, Y. Chu, L. Li, Q. Yu, Y. Zhu, G. Liu, Q. Hou, R. Zeng and L. Zhao, *Electrochim. Acta*, 2016, **188**, 909-916.

[12] G. Huang, S. Xu, S. Lu, L. Li and H. Sun, *ACS Appl. Mater. Interfaces*, 2014, **6**, 7236-7243.

[13] S. Abouali, M. Akbari Garakani, B. Zhang, H. Luo, Z.-L. Xu, J.-Q. Huang, J. Huang and J.-K. Kim, *J. Mater. Chem. A*, 2014, **2**, 16939-16944.

[14] J. Xu, J. Wu, L. Luo, X. Chen, H. Qin, V. Dravid, S. Mi and C. Jia, *J. Power Sources*, 2015, **274**, 816-822.

[15] Y. Liu, Z. Cheng, H. Sun, H. Arandiyan, J. Li and M. Ahmad, *J. Power Sources*, 2015, **273**, 878-884.

[16] X. Zhou, J. Shi, Y. Liu, Q. Su, J. Zhang and G. Du, *Electrochim. Acta*, 2014, **143**, 175-179.

[17] Y. Lou, J. Liang, Y. Peng and J. Chen, *Phys. Chem. Chem. Phys.*, 2015, **17**, 8885-8893.

[18] G. Huang, F. Zhang, X. Du, Y. Qin, D. Yin and L. Wang, *ACS Nano*, 2015, **9**, 1592-1599.

[19] L. Shen and C. Wang, *Electrochim. Acta*, 2014, **133**, 16-22.

[20] X. Liu, S. W. Or, C. Jin, Y. Lv, W. Li, C. Feng, F. Xiao and Y. Sun, *Electrochim. Acta*, 2013, **100**, 140-146.

[21] L. Wang, Y. Zheng, X. Wang, S. Chen, F. Xu, L. Zuo, J. Wu, L. Sun, Z. Li, H. Hou and Y. Song, *ACS Appl. Mater. Interfaces*, 2014, **6**, 7117-7125.

[22] Y. Sun, F. Huang, S. Li, Y. Shen and A. Xie, *Nano Res.*, 2017, **10**, 3457-3467.

[23] L. Guo, Y. Ding, C. Qin, W. Li, J. Du, Z. Fu, W. Song and F. Wang, *Electrochim. Acta*, 2016, **187**, 234-242.

[24] D. Li, D. Shi, Z. Chen, H. Liu, D. Jia and Z. Guo, *RSC Adv.*, 2013, **3**, 5003-5008.

[25] X. Tian, X. Sun, Z. Jiang, Z.-J. Jiang, X. Hao, D. Shao and T. Maiyalagan, *ACS Appl. Energy Mater.*, 2018, **1**, 143-153.

[26] C. K. Ranaweera, C. Zhang, S. Bhoyate, P. K. Kahol, M. Ghimire, S. R. Mishra, F. Perez, B. K. Gupta and R. K. Gupta, *Mater. Chem. Front.*, 2017, **1**, 1580-1584.

[27] Z. Yang, K. Qian, J. Lv, W. Yan, J. Liu, J. Ai, Y. Zhang, T. Guo, X. Zhou, S. Xu and Z. Guo, *Sci. Rep.*, 2016, **6**, 27957.

[28] L. Zhang, Z. Su, F. Jiang, L. Yang, J. Qian, Y. Zhou, W. Li and M. Hong, *Nanoscale*, 2014, **6**, 6590-6602.

[29] D. Bhattacharjya, H.-Y. Park, M.-S. Kim, H.-S. Choi, S. N. Inamdar and J.-S. Yu, *Langmuir*, 2014, **30**, 318-324.

[30] W. Deng, Y. Zhang, L. Yang, Y. Tan, M. Ma and Q. Xie, *RSC Adv.*, 2015, **5**, 13046-13051.

[31] W. Si, J. Zhou, S. Zhang, S. Li, W. Xing and S. Zhuo, *Electrochim. Acta*, 2013, **107**, 397-405.

[32] X. Li, Y. Fang, L. Wen, F. Li, G. Yin, W. Chen, X. An, J. Jin and J. Ma, *Dalt. Trans.*, 2016, **45**, 5575-5582.

[33] J. Liu, H. Xia, L. Lu and D. Xue, *J. Mater. Chem.*, 2010, **20**, 1506-1510.

[34] C. Cheng, G. Zhou, J. Du, H. Zhang, D. Guo, Q. Li, W. Wei and L. Chen, *New J. Chem.*, 2014, **38**, 2250-2253.

[35] G. Huang, F. Zhang, X. Du, Y. Qin, D. Yin and L. Wang, *ACS Nano*, 2015, **9**, 1592-1599.

[36] X. Chi, L. Chang, D. Xie, J. Zhang and G. Du, *Mater. Lett.*, 2013, **106**, 178-181.

[37] X. Leng, S. Wei, Z. Jiang, J. Lian, G. Wang and Q. Jiang, *Sci. Rep.*, 2015, **5**, 16629.

[38] H.-H. Li, L. Zhou, L.-L. Zhang, C.-Y. Fan, H.-H. Fan, X.-L. Wu, H.-Z. Sun and J.-P. Zhang, *ACS Energy Lett.*, 2017, **2**, 52-59.

[39] Z. Fang, W. Xu, T. Huang, M. Li, W. Wang, Y. Liu, C. Mao, F. Meng, M. Wang, M. Cheng, A. Yu and X. Guo, *Mater. Res. Bull.*, 2013, **48**, 4419-4423.

[40] Z. Zhang, L. Li, Q. Xu and B. Cao, *RSC Adv.*, 2015, **5**, 61631-61638.

[41] J. Mujtaba, H. Sun, G. Huang, K. Mølhave, Y. Liu, Y. Zhao, X. Wang, S. Xu and J. Zhu, *Sci. Rep.*, 2016, **6**, 20592.

[42] Y. Bai, X. Wang, X. Zhang, H. Shu, X. Yang, B. Hu, Q. Wei, H. Wu and Y. Song, *Electrochim. Acta*, 2013, **109**, 355-364.

[43] A. Y. Shenouda and H. K. Liu, *J. Power Sources*, 2008, **185**, 1386-1391.

[44] T. Liu, A. Garsuch, F. Chesneau and B. L. Lucht, *J. Power Sources*, 2014, **269**, 920-926.

Chapter 7

Conclusion and Future Prospect

7.1 Summary of research work

This thesis discussed new anode materials with excellent capacity and cycle life for lithium ion battery. Synthesis of transition metal oxides (Fe_2O_3, Co_3O_4 and NiO) and their nanocomposites with different carbon material as anode materials was done for their high theoretical capacity. Development of various types of conversion type anode materials is particularly the state-of the art of this work. The charge storage mechanism and the shortcomings associated with those materials in terms of charge storage have been explained. Different approaches are discussed to improve the performance of these materials along with modification in order to address the shortcomings. Feasible synthesis strategies have been employed and electrochemical testing of materials is demonstrated in coin cell assembly. Key role of individual component of composites has been discussed separately in their electrochemical performance as LIB.

The chapter wise conclusion is discussed in details below.

Chapter 1 presents the introduction of energy storage devices and LIBs (working principle and different components) are discussed in detail.

Chapter 2 elaborated different synthesis techniques of different nanocomposites of metal oxides and carbon materials and their material and electrochemical characterization techniques.

Chapter 3 provided an account on the synthesis of the novel ternary hybrid electrode material of NFOC with different morphological structures. TEM study indicates the $Ni(OH)_2$ nanosheets are decorated with Fe_2O_3 nanoparticles and further these sheets are wrapped on CNOs. Here CNOs network used to sustain structural integrity of the electrode material, to enhance the electronic transport and decrease the Li-ion diffusion path. As Prepared NFOC electrode material exhibits 1112 $mAhg^{-1}$ of 1^{st} discharge capacity at 50 mAg^{-1} of current density. Also retains 60.5% of specific capacity at 1000 $mAhg^{-1}$ of higher current. It shows 96% capacity retention after 1000 charge-discharge cycles with more than 99% of coulombic efficiency.

Chapter 4 presents the research on synthesis of ternary nanocomposite of NDC/NiO/NFO novel electrode material with hetero structure morphology where, mixed morphology of

$NiFe_2O_4$ nanoparticles with nanosheets of NiO and N doped carbon. Polydopamine derived N doped carbon in the composite play an important role to improve the cycle lifespan and rate capacity of the electrode material by provides more active sites to react with li ions and increases the conductivity. N doped carbon matrix also act as a buffer to sustain volumetric expansion of the ternary composite during cycling. High theoretical capacity and sheet like morphology NiO used to avoid the aggregation of $NiFe_2O_4$ nanoparticles and to improve the conductivity of the active material. It delivers a reversible discharge capacity of 786 $mAhg^{-1}$ at 0.1 Ag^{-1} and 463 $mAhg^{-1}$ at a higher current density of 2 Ag^{-1}. Furthermore, it exhibit stable cycle life over 1000 cycles with 98% capacity retention and more than 99% of coulombic efficiency.

Chapter 5 deals with the synthesis of a well-designed Co_3O_4 NPs anchored on f-CNH foam architecture composite by a facile freeze drying process as anode materials for LIBs. Here f-CNH used as an electronically conductive network and elastic buffer to prevent the volumetric expansion and contraction of Co_3O_4 NPs during the lithiation and delithiation process. Intimate integration of Co_3O_4 and f-CNH foam in nanocomposite improved battery performance and cycle life where more surface area and three-dimensional interconnected mesoporous structure of f-CNH foam provides essential channels for charge transport. It retains a discharge capacity of 820 $mAhg^{-1}$ over 500 cycles with more than 99% of Coulombic efficiency. At 5 Ag^{-1} of high current density it delivers 702 $mAhg^{-1}$ of high specific capacity value.

Chapter 6 deals with the synthesis of NSCS-Co_3O_4 nanocomposite as an anode material with a significant potential for application in lithium ion batteries as high energy density material. Hetero atoms (N and S) doped carbon spheres enhance the electronic conductivity and also provide more binding sites for facile deposition of a large number of Co_3O_4 nanoparticles. It also provides the channels for charge and ionic transport, which effectively alleviates the aggregation of Co_3O_4 in the Li^+ insertion/extraction. As a consequence, NSCS-Co_3O_4 shows excellent rate performance and long cycle life. As synthesized NSCS-Co_3O_4 exhibit less charge transfer resistance with more Li ion diffusion coefficient value of 1.73 x 10^{-12} cm^2s^{-1}.

7.2 Future prospects

Limited availability of Li in the earth's crust increase the price of high energy li ion battery. Low cost and more abundant nature of sodium metal makes sodium ion battery (SIBs) an outstanding alternative candidate to replace existing LIBs in large scale stationary energy storage systems. Compared to lithium, sodium has lower standard half reaction potential (2.7

V vs. Na/Na^+ and 3.045 V vs. Li/Li^+ for Li) which gives benefit of lesser electrolyte degradation with increasing the safety of SIBs. However, large size of Na ion (r ~ 0.102 nm) decreases the reaction kinetics of Na ion transportation, resulting in fading of capacity value, poor rate capability and short cycle life. Therefore, developing high capacity electrode materials for commercial application of SIBs is still an urgent need.

Although hard carbon materials deliver good cyclic stability, there is still lot to do on capacity front to make the sodium ion battery realizable for modern applications like grid power and electric vehicles. Several anode materials have been explored for SIBs and classified into different category like carbonaceous materials (insertion-deinsertion), alloy materials, conversion materials (Fe, Cu, Ni, or Co-based oxides), conversion and alloying materials (Sn, Sb-based oxides). Among all anode material, conversion based metal oxides (MOs) are most promising candidate, because of their suitable redox potential, good safety and high energy densities. However, low coulombic efficiency and an unsatisfactory rate performance has been observed in the case of TMOs due to intrinsically low electric conductivity and slow rate of Na-ion transportation during sodiation-desodiation. Moreover, structural disorientation occurred via large volume change and structure pulverization of the metal oxides affects the cycling performance.

To address these issues TMOs can be tailored in nanostructures and nanocomposites with carbonaceous materials to improve the electrochemical performance compared to bulk material. Nanostructured TMOs and their composite with carbonaceous materials can provide short Na^+ diffusion path length, large electrode-electrolyte interface and good mechanical stability during sodiation-desodiation process. Carbon matrix in composite with TMOs can provide electrical conductivity and overcome rate capability problem of TMOs. Hetero atom doping in carbon matrix can increase the interlayer spacing, create defective site on the surface and provide more active sites to store more Na ions and can improve the battery performance by increasing cycle life and rate capability.

Additionally, the conversion in combination with alloying based materials like Sb_2S_3, Sb_2Se_3, SnS_2, SnS, $SnSe_2$, and Bi_2Se_3 can also store more Na ions with higher capacity owing to the two sodium storage mechanisms being operational simultaneously. These materials with carbon coatings shall furnish high specific capacities with enhanced cycle and rate performance.

List of publications

1. **Pravin Kumari Dwivedi,** Vedi Kuyil Azhagan Muniraj, Dr. Rami Reddy Deverapalli, Dr. Manjusha V Shelke, $Ni(OH)_2$-Fe_2O_3/CNOs ternary nanocomposite designed as an anode with complementary properties for high-performance Li-ion battery, **ChemistrySelect., 3,8, 2286 - 2292 (2018).**

2. Vedi Kuyil Azhagan Muniraj, **Pravin Kumari Dwivedi**, Parikshit Shivaji Tamhanea, Sabine Szuneritsc, Rabah Boukherroub and Manjusha Vilas Shelke, "High energy flexible supercapacitor - Synergistic effects of Polyhydroquinone and $RuO_2 \cdot xH_2O$ with micro-sized, few layered, self-supportive exfoliated-graphite sheets" **ACS applied material and interface, 11, 20, 18349-18360 (2019).**

3. Anil A. Kashale, **Pravin K. Dwivedi,** Bhaskar R. Sathe, Manjusha V. Shelke, Jia-Yaw Chang, and Anil V. Ghule. "Biomass-Mediated Synthesis of Cu-Doped TiO_2 Nanoparticles for Improved-Performance Lithium-Ion Batteries", **ACS Omega, 3, 10, 13676-13684 (2018).**

4. Anil A. Kashale, Akash S. Rasal, Gokul P. Kamble, Vijay H. Ingole, **Pravin K. Dwivedi,** Swapnil J. Rajoba, Lata D. Jadhav, Jia-Yaw Chang and Anil V. Ghule "Biosynthesized Co-Doped TiO_2 Nanoparticles based Anode for Lithium-Ion Battery Application and Investigating the Influence of Dopant Concentrations on its Performance" **Journal of Composite B, DOI:10.1016/j.compositesb.2018.12.001.**

5. Anupam Biswas, Mayuresh A Kulkarni, Rangarajan Bakthavatsalam, Sourik K Mondal, **Pravin K Dwivedi**, Manjusha V Shelke, Radhamonyamma N Devi, Arun G Banpurkar And Janardan Kundu, Facile Synthesis and Self-Cleaning Application of Bimetallic (CuSn, CuNi) Dendrites, **ChemistrySelect., 2, 5552 - 5563 (2017).**

6. **Pravin Kumari Dwivedi,** Rupali S. Mehare, Vikash Chaturvedi, Dr. Manjusha V Shelke, "Co_3O_4 NPs decorated N, S co-doped Carbon Spheres Nanocomposite as an Anode Material for High Performance Li-Ion Battery" in communication.

7. **Pravin Kumari Dwivedi,** Golu Parte, M. Thripuranthka, Dr. Manjusha V Shelke, "Co_3O_4 NPs Decorated on 3-D CNH Foam as a Promising Anode Material for Li ion Battery" manuscript under preparation**.**

8. Ashvini B. Deshmukh, **Pravin K. Dwivedi,** Archana C. Nalawade, Mohammed S. Qureshi, Manjusha V.Shelke, "Li-ion battery anode from Fe_3O_4 nanoparticles embedded in Nitrogen doped porous carbon with improved rate capabilities" **in communication**.
9. Rupali S. Mehare, **Pravin Kumari Dwivedi,** and Dr. Manjusha V Shelke, "Nitrogen and Sulfur doped Hierarchical Porous Carbon as High Performance Anode Material for Li-ion and Sodium Ion Batteries", in communication.
10. Asiya F. Shaikh, Mohaseen S. Tamboli, **Pravin Kumari Dwivedi**, C. S. Praveen, Indrapal Karbhal, Suresh W. Gosavi, Manjusha V. Shelke, and Bharat B. Kale, "Architecture of $NaFe(MoO_4)_2$ as a Novel Anode Material for High Performance Lithium and Sodium Ion Batteries" in communication.

Book Chapters

1. "Nanostructured Materials for Li-Ion Battery Applications." Pushpendra Kumar, **Pravin K. Dwivedi,** Poonam Yadav and Manjusha V. Shelke, Emerging Nanostructured Materials for Energy and Environmental Science, pp 105-172, Environmental Chemistry for a Sustainable World.
2. "Metal and Non-Metal doped Metal Oxides and Metal Sulphides for Photocatalysis." Poonam Yadav, **Pravin K. Dwivedi**, Surendar Tonda, Rabah Boukherroub and Manjusha V. Shelke, Green Photocatalysts, pp 89-132, Environmental Chemistry for a Sustainable World.

Erratum